



**Politecnico  
di Torino**

**Politecnico di Torino**

Corso di Laurea Magistrale in Ingegneria Meccanica

A.a. 2020/2021

Sessione di Laurea Dicembre 2021

# **Design and characterization of drug delivery devices with embedded sensors**

Relatori:

Prof. Giorgio De Pasquale

Prof. Alessandro Grattoni

Candidato:

David William Charig



*“I have no special talents. I am only passionately curious.”*

*Albert Einstein*

## Abstract

Implantable drug delivery devices are an emerging technology and a promising alternative for controlled drug release applications. Their development has progressed considerably in recent years and affects the work of many research centers all over the world. Nowadays, efforts are converging in the realization of continuously tunable drug delivery systems able to operate independently of constant external activation. In many of these systems, drug release is controlled via concentration-based diffusion through nanofluidic membranes that regulate the delivery of drug compounds from an implantable reservoir. Such systems are suitable for many different applications in the biomedical field, especially in the management of chronic diseases where continuous ad hoc monitoring and rapid adjustment of drug doses are needed. Furthermore, they allow localized delivery with the possibility of lower drug concentrations. In the following chapters, we discuss the design and development of implantable devices for drug delivery with embedded strain sensors to measure the osmotic pressure on which the drug flow release depends. This project revolves about the nanofluidic membrane developed by Dr. Alessandro Grattoni at the Houston Methodist Research Institute. The initial phase of activity focuses on the analysis of different types of sensors to select the best instrument to measure reservoir pressures of our systems. After a careful evaluation, the choice fell on the use of strain gauges of which a brief theoretical review is proposed. The following step concerns the FEM structural analysis of different design solutions to characterize the main properties of our implantable devices and realize samples to perform tests. The thesis proceeds with the presentation and set up of the data acquisition system used for in vitro tests and the explanation of the assembled test bench to pressurize the prototypes. We tested several capsule samples, some provided by Dr. Grattoni Laboratory and others developed by us. In the end, the core experimental activity of the thesis is presented with the description of the in vitro tests and the analysis of the acquired data. In particular, we focused on the correlation between pressure and strain to validate the measurement method and check its accuracy, by comparing with the results obtained with theoretical computations.

# List of Contents

Chapter 1 Introduction and design .....	1
1.1 Introduction.....	1
1.2 Finite element analysis of cylindrical capsules .....	2
1.2.1 Static structural analysis results .....	5
1.3 Design of the test capsule sample (disc-shaped capsule).....	9
1.3.1 Capsule geometry.....	10
1.3.2 FEM static structural analysis and results .....	11
1.4 Overcoming the problem of external stresses .....	13
1.4.1 Protective external shell .....	13
FEM structural analysis.....	14
Chapter 2 Introduction to Strain Gauges.....	19
2.1 Overview of Electrical Strain Gauges.....	19
2.1.1 Backing Material .....	20
2.1.2 Adhesives .....	20
2.2 Gauge Factor .....	20
2.2.1 Measuring grid material .....	21
2.2.2 Temperature Effect.....	21
2.3 Wheatstone Bridge Circuit.....	22
2.3.1 Strain Measurement using the Wheatstone Bridge .....	24
2.3.2 Bridge Sensitivity.....	24
2.3.3 Bridge Factor .....	25
2.3.4 Quarter Bridge Configuration .....	25
2.3.5 Half-Bridge Configuration .....	26
2.3.6 Full Bridge Configuration .....	27
2.4 Strain Gauge Accuracy.....	28
2.5 Strain Gauge Linearity, Hysteresis and Zero Drift.....	28
2.6 Strain Gauge Rosette.....	29
2.6.1 Three Element 45° Rectangular Rosette .....	30
2.6.2 Three Element 60° Delta Rosette.....	31
Chapter 3 Measuring amplifier and calibration.....	32
3.1 Measuring amplifier.....	32
3.2 Calibration of the measuring system.....	33
3.2.1 Strain computed with solid mechanics theory.....	33
3.2.2 Experimental setup.....	34
3.2.3 Quarter bridge circuit with 4-wires .....	36

3.2.4	Half bridge configuration .....	40
3.2.5	Full bridge configuration.....	43
Chapter 4	Test Bench.....	47
4.1	Structure and characteristics of the test bench .....	47
Chapter 5	Samples and sealing tests .....	51
5.1	Samples .....	51
5.1.1	Disc-shaped capsules produced with additive manufacturing.....	51
5.1.2	Samples from the Houston Methodist Research Institute .....	55
Chapter 6	Experimental tests with sensorized samples and analysis of the results.....	58
6.1	Installation of strain gauges on samples.....	58
6.2	Test procedure .....	60
6.2.1	Sample 1: titanium alloy threaded capsule.....	61
6.2.2	Sample 2: additive manufactured titanium alloy capsule.....	65
6.2.3	Sample 3: additive manufactured polyamide 12 capsule .....	68
6.3	Analysis of testing results .....	72
6.3.1	Theoretical equation which relates strain and pressure.....	72
6.3.2	Theoretical calculation of strain for sample 1 .....	73
6.3.3	Theoretical calculation of strain for sample 2 .....	75
6.3.4	Theoretical calculation of strain for sample 3 .....	76
6.3.5	Comparison between theoretical and experimental results .....	78
Chapter 7	Conclusion.....	79
Bybliography	.....	81

# Chapter 1

## Introduction and design

### 1.1 Introduction

For my master's degree thesis, I've chosen a topic connected to the health care sector, a field very dear to me since before joining the Politecnico di Torino to pursue a career in mechanical engineering, I earned a bachelor's degree in medical radiology, imaging and radiotherapy techniques. Hence my desire to perform a dissertation related to biomedical engineering.

This thesis aims to analyze the early-stage design of an implantable drug delivery device. The developing of a prototype revolves around the nanofluidic membrane developed by Dr. Alessandro Grattoni and Dr. Nicola Di Trani at Houston Methodist Research Institute for controlled drug release applications. A promising alternative drug delivery approach is the use of implantable devices to release drug compounds. The most common and convenient method of drug delivery is still the oral route. Nevertheless, it presents several inconveniences and challenges as well, along with other common routes in particular transdermal or intravenous injection. Many drugs are unacceptable for delivery via oral route. The reasons could be a drug deterioration in the acid conditions of the stomach or alkaline ambient in the intestine, first-pass metabolism or compliance problems. Implantable drug release systems can provide targeted and localized delivery and fulfil a therapeutic outcome with lower drug concentrations. Consequently, they can minimize side effects of therapy, offering the possibility for increased patient compliance [1].

To reach the proposed goal, an initial documentation phase was carried out. By reading several research papers about nanofluidic-enabled implants written by Dr. Grattoni and Dr. Di Trani, it was possible to determine the main features of the device. In the first instance, it can be comparable to a small reservoir connected by the nanofluidic membrane to the outside environment. Very small dimensions are a fundamental requirement to facilitate implantation and to avoid patient's discomfort. The implant must have external communication capabilities to be able to send data. Among these, the information of the drug flow rate is vitally important. Hence the need to find the right sensor to accurately measure it. After checking the sensors available in the market, it was decided to determine the flow rate indirectly by measuring the pressure inside the drug reservoir. The possibility of using MEMS (Micro Electro-Mechanical Systems) as pressure sensors was quickly abandoned. Indeed, despite being very precise, MEMS pressure sensors have a relatively high cost. Eventually, we concluded that we could get the pressure measurement through the use of a strain gauge. The working principle is the same as for strain gauge based pressure transducers: a strain gauge can detect the deformation of an elastic material caused by pressure, resulting in a change of its resistance that is converted into a useable electrical signal. The measure of strain can be correlated to the measure of pressure with which the flow rate can be calculated. The plan is to build a workbench whereby we can pressurize some prototypes of sensorized capsules and collect the measurements of the deformations and corresponding pressures.

## 1.2 Finite element analysis of cylindrical capsules

In the first place a FEM structural analysis was conducted to characterize some concepts of the device. We used ANSYS Workbench software to this purpose. Inspired by prototypes used in the Nanofluidics for Drug and Cell Delivery Laboratory of Dr. Grattoni, we made some cylindrical designs through CAD software. We initially created two very similar CAD geometries to each other. The first model has a bullet-like shape i.e. a cylindrical shell closed at one end by an approximately hemispherical shell which features a hole at the tip that will house the nanofluidic membrane (Figure 1.1).

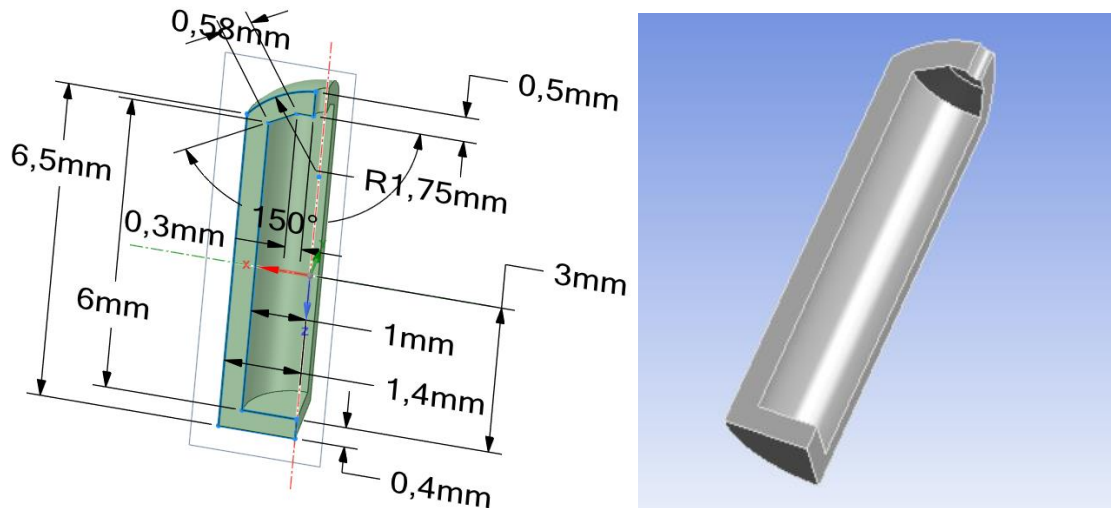


**Figure 1.1** Dimensions of the bullet-like drug reservoir.

The second one has a classic capsule form i.e. a cylindrical hull closed at both extremities by hemispherical shells (Figure 1.2). In either form, the drug reservoir is very small in size to meet our requirements, with a total height of approximately 8 mm, an external diameter of about 3 mm and a thickness of 0,5 mm. Refer to the figures for the detailed dimensions of the models. The geometries of both capsules were created using ANSYS DesignModeler.

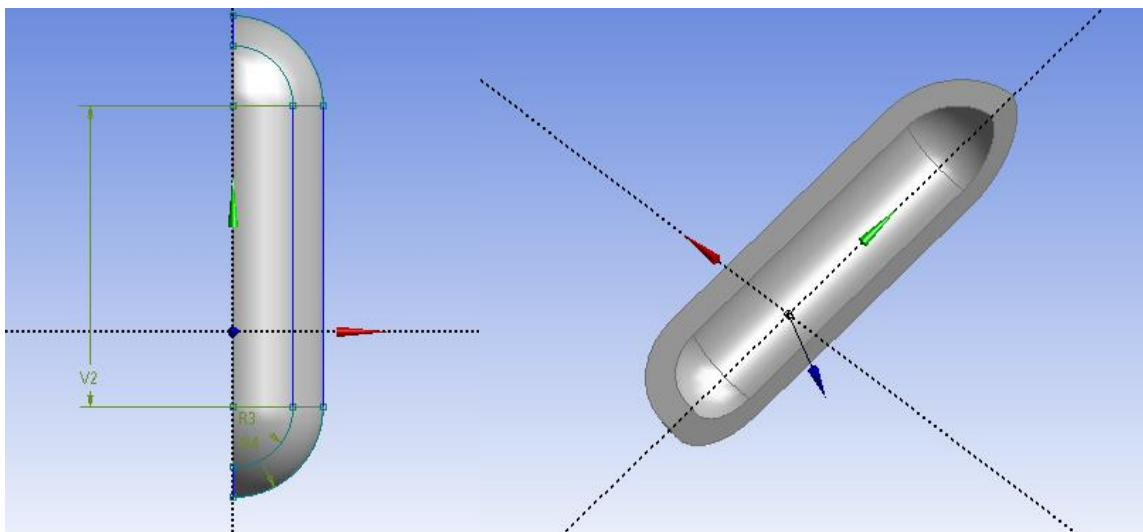
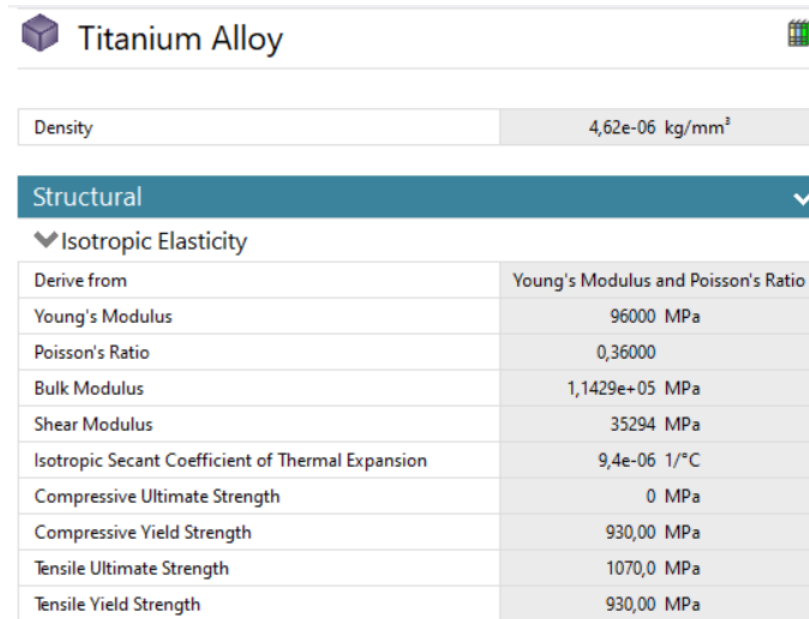


**Figure 1.2** Dimensions of the capsule form reservoir:  $V2 = 5$  mm,  $R3 = 1$  mm,  $R4 = 1,5$  mm.

Titanium alloy Ti6Al4V was chosen as the reference material since titanium is considered the most biocompatible metal due to its resistance to corrosion from bodily fluids, bio-inertness and high fatigue limit. Aimed at running the simulations, the following material properties, listed by Table 1.1, were applied.



Derive from	Young's Modulus and Poisson's Ratio
Young's Modulus	96000 MPa
Poisson's Ratio	0,36000
Bulk Modulus	1,1429e+05 MPa
Shear Modulus	35294 MPa
Isotropic Secant Coefficient of Thermal Expansion	9,4e-06 1/°C
Compressive Ultimate Strength	0 MPa
Compressive Yield Strength	930,00 MPa
Tensile Ultimate Strength	1070,0 MPa
Tensile Yield Strength	930,00 MPa

**Table 1.1** Properties of the titanium alloy Ti6Al4V.

3D structural solid model analysis of both reservoirs was performed, and the overall shape of the components was approximated by thousands of nodes connected during meshing process. For the bullet-shaped geometry we also carried out a 2D axisymmetric model that represents a slice of the actual 3D model and if revolved around the axis of the reference cartesian coordinate system, would become the original 3D structure. 2D axisymmetric finite-element modeling can be used when the object under consideration is a geometric shape in the circumferential direction of the cylindrical coordinate system and the load conditions are symmetric. Essentially, the aim was to check the convergence of 2D and 3D analysis methods and verify the results. We generated the meshes of the 3D reservoirs with ‘Sweep Method’ meshing feature, in which the section face along the axis of the cylindrical volume is meshed and then “swept” through the body creating a volume mesh, using high quality quadrilateral elements. For the 2D model we generated a ‘Face Sizing’ mesh.

Hence, we loaded the reservoirs with a constant internal pressure of 20 MPa to determine where the areas of maximum deformation, strain and stress were. Indeed, our device will mount a strain gauge on it and one of the goals of the structural analysis is to understand where it is convenient to fix the sensor, depending on the geometry and the shape of the reservoir. In fact, to ensure maximum sensitivity, the strain gage should be installed in the available area with the greatest deformation and strain. Moreover, this structural evaluation will allow us to estimate a safety factor of the designed capsules and rate the material properties. Considering the symmetry of the parts and the applied load, to perform the static structural simulation and acquire very truthful results, we set the constraints of the 3D models by blocking the displacement of a single node along the axis of the cylinder.

To avoid invalidation of the results, we picked a node in a region of little deformations: for the bullet-like reservoir we selected a node about halfway up the outer cylinder in the 3D model (Figure 1.3 A). Whereas, for the 2D axisymmetric model we blocked the displacement of a vertex along the axis of the cylinder (Figure 1.3 B).

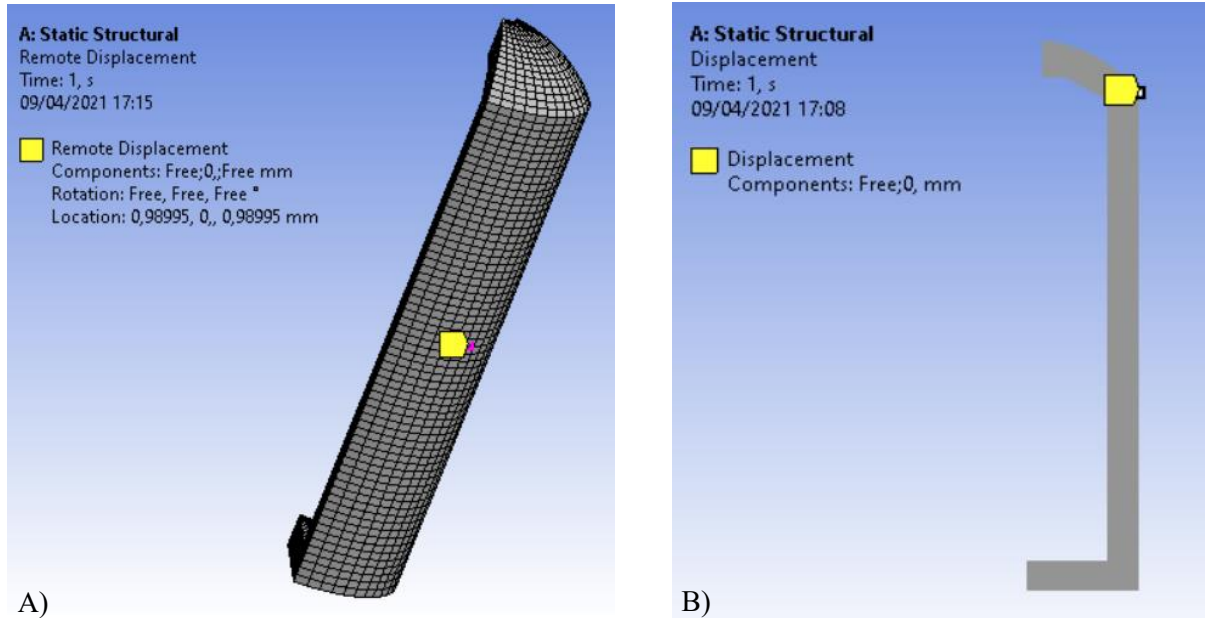


*Figure 1.3* A) 3D bullet-like model constraints. B) 2D bullet-like axisymmetric model constraints.

For the other 3D model, we adopted null displacement along the axis for the node located on top of the capsule (Figure 1.4).

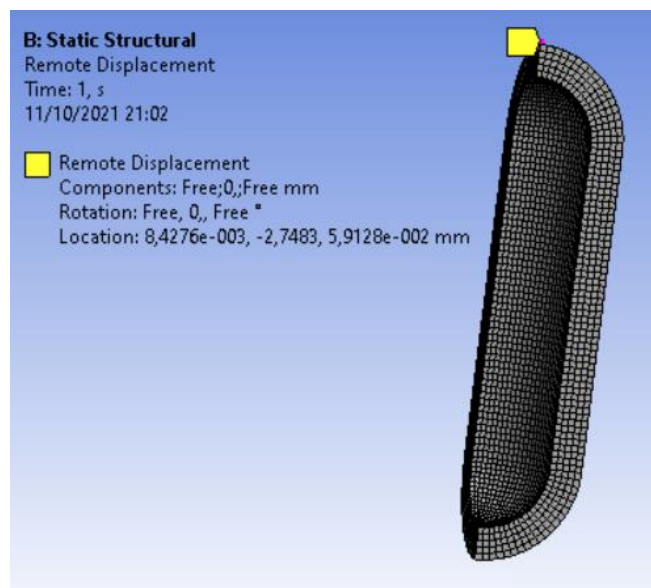


*Figure 1.4* 3D capsule-like model constraints.

## 1.2.1 Static structural analysis results

The results of the FEM analysis are presented in the following section. Depending on the shape of the model, the results differ as regards the position and the value of the maximum strains and stresses.

The results of the 3D bullet-modeled geometry are presented below. In the following visualizations, results that display in red represent high stress or high deformation and results that display in blue represent low stress or low deformation.

### EQUIVALENT ELASTIC STRAIN (VON MISES) – BULLET-SHAPED MODEL

Von Mises approach is chosen to approximate the overall elastic strain value of the reservoir. Figure 1.4 shows that the internal pressure of  $20\text{ MPa}$  brings to a maximum strain of  $1,4975 \cdot 10^{-3}\text{ mm/mm}$  at the inner edge of the bottom (flat side) of the cylindrical reservoir. There's also a region of maximum strain at the upper edge of the internal cylinder, shown by the red color. Another area in which the strains are very consistent is that in correspondence with the center of the outer circle that forms the bottom (flat side) of the capsule. The zones of minor deformation are colored blue and are located on the outside edges of the cylinder (Figure 1.5).

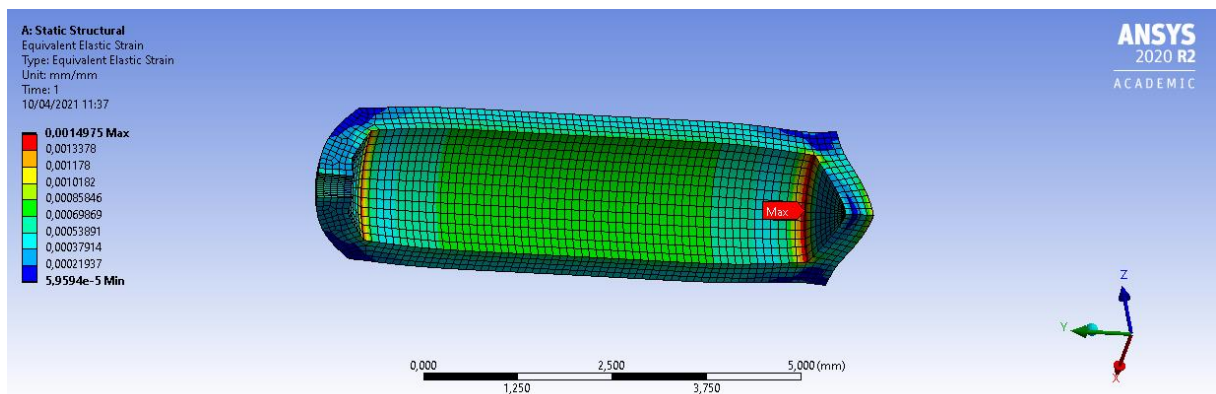


**Figure 1.4** Equivalent Elastic Strain of the 3D bullet-shaped model, maximum strain value.

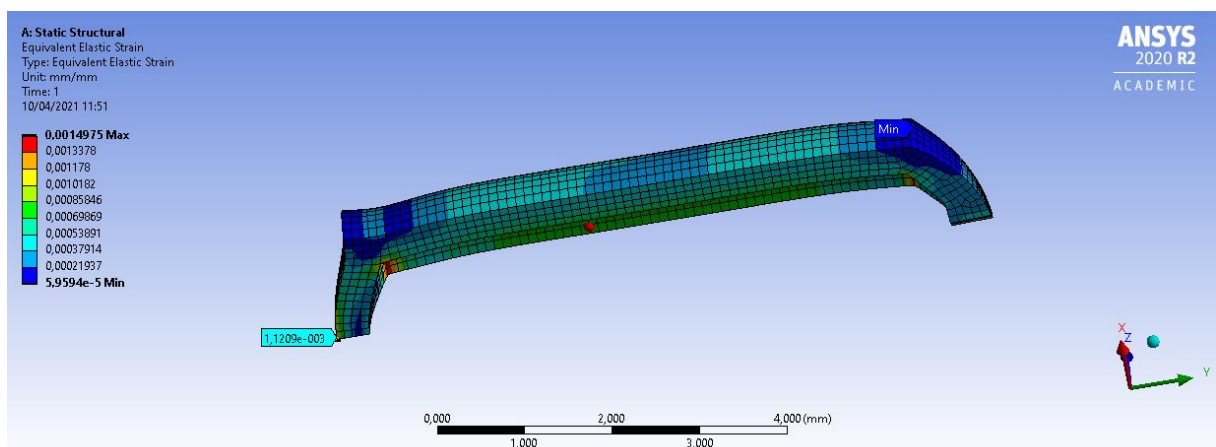


**Figure 1.5** Equivalent Elastic Strain of the 3D bullet-shaped model, external bottom and minimum value.

EQUIVALENT STRESS (VON MISES) – BULLET-SHAPED MODEL

We used the maximum distortion criterion (Von Mises) to approximate the overall stress value of the capsule. The situation reflects the one analyzed for the equivalent elastic strain. Located at the inner edge of the bottom (flat side) of the cylindrical reservoir, Figure 1.6 depicts a maximum stress value of 135,4 MPa and a similar stress is also present in the top inner edge of the cylinder. Major stresses are present in correspondence with the center of the outer circle which forms the lower part of the capsule. The areas of minor stress are colored blue and are located on the outside edges of the cylinder (Figure 1.7).

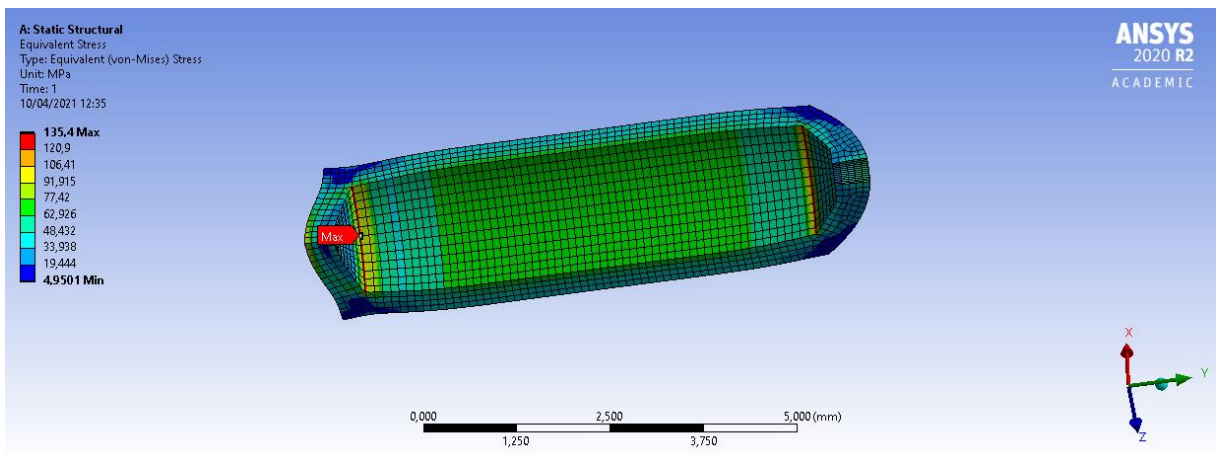


Figure 1.6 Equivalent Stress of the 3D bullet-shaped model, maximum stress value.

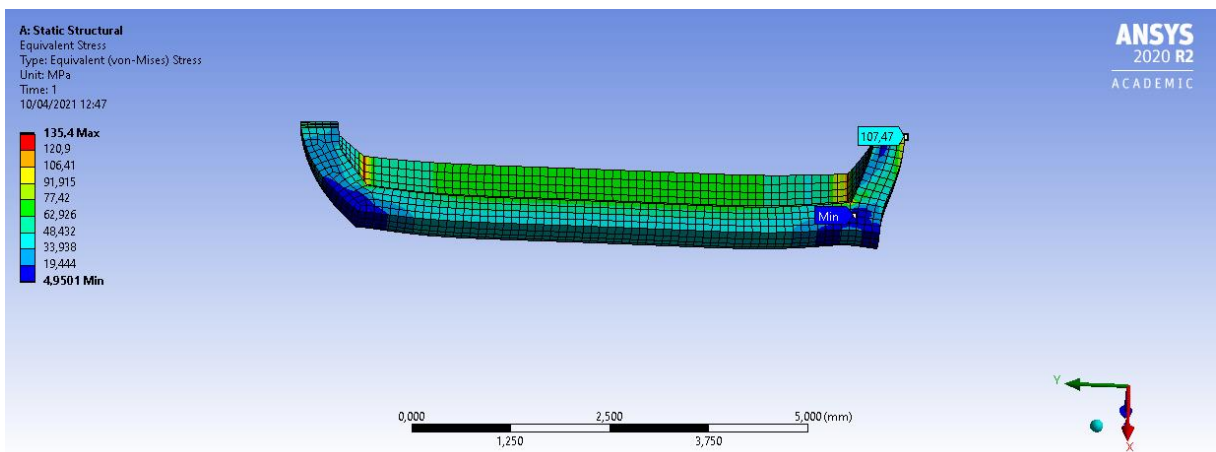


Figure 1.7 Equivalent Stress of the 3D bullet-shaped model, external bottom and minimum value.

Based on the outcomes of the FEM structural analysis performed on the bullet-shaped capsule, we can make some observations about the material and the possible locations where the strain gauge can be installed. Titanium alloy Ti6Al4V represents a suitable candidate to be used as the construction material of the device because of its high mechanical strength. This characteristic may be very important for an instrument that needs to work inside the human body. Implantable systems based on controlled drug delivery via concentration driven diffusion through nanofluidic membrane, should normally operate with osmotic pressures ranging from few bars up to about 10 bars. Nevertheless, in this analysis, we imposed an internal pressure 20 times higher than the maximum normally achievable to verify the integrity of the system in an extremely critical condition. From the results, it is clear that the selected material behaves well even at exceptionally high pressures. It should be noted that the visualization of the FEM model under pressure, illustrated in the previous figures, shows very accentuated deformations, but this is due to the high deformation scale factor used by the software. Deformation scale factor involves scaling the maximum displacement amplitude to display a distorted mesh image and it can be either chosen a large scaling coefficient to zoom on the deformed geometry or a small coefficient to achieve a realistic visualization. Maximum values of strain and stress occur where there is a sudden variation in the internal geometry of the reservoir, i.e. at the inner edges in the bottom and the top of the cylinder. In order to contrast this problem, a small fillet radius can be added.

Regarding the right location of the reservoir where the strain gauge can be fixed, the bottom of the capsule may be a good alternative because of its large tendency to deformation that could provide high sensing sensitivity. However, one drawback is the limited space available at this position. A larger available area is offered by the cylindrical surface of the capsule, although here we have lower deformations and thus a reduced sensing sensitivity for the strain gauge.

The results of the structural analysis for the capsule-shaped model are now reported.

### EQUIVALENT ELASTIC STRAIN (VON MISES) – CAPSULE-SHAPED MODEL

The maximum distortion strain energy criterion (Von Mises) is used to compute the analysis. The figure below displays the capsule with an internal pressure of  $20 \text{ MPa}$  and a maximum strain of  $0,6527 \cdot 10^{-3} \text{ mm/mm}$  located on the inside surface of the cylinder. The rest of the internal surface, in correspondence with the two hemispheres, shows considerable deformations which are marked with the colors orange and yellow.

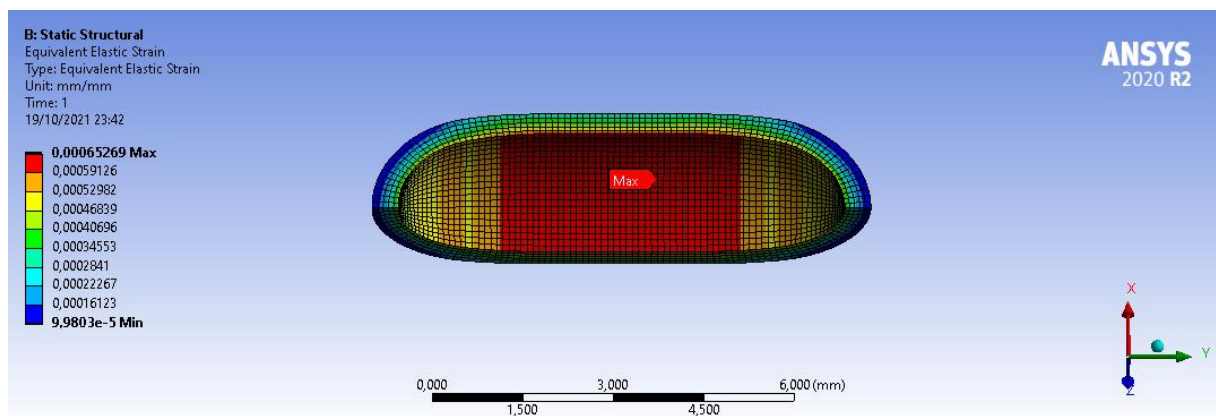
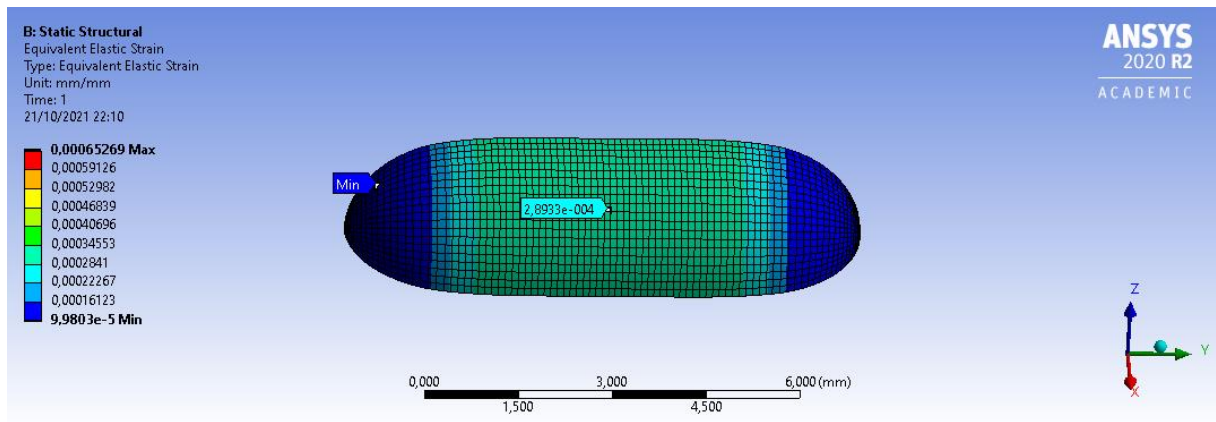


Figure 1.8 Equivalent Elastic Strain of the 3D capsule-shaped model, maximum strain value.

The outer surface of the capsule exhibits minimal deformation at the upper and lower hemispheres. A computed strain of  $0,2893 \cdot 10^{-3} \text{ mm/mm}$  on the external area of the cylinder is highlighted with a tag (Figure 1.9).



**Figure 1.8** Equivalent Elastic Strain of the 3D capsule-shaped model, minimum strains.

#### EQUIVALENT STRESS (VON MISES) – CAPSULE-SHAPED MODEL

Von Mises criterion was used to compute the total stress of the reservoir. The situation mirrors that analyzed for the corresponding elastic strain. The maximum stress value is located on the cylindrical internal surface and is equal to  $62,66 \text{ MPa}$ , as shown with red color in Figure 1.9. At the ends of the reservoir, high values of stress are present on the internal area of the two hemispheres. Figure 1.10 shows the minimal stress values of in the external area of the lower hemisphere and upper hemisphere. On the external cylindrical surface, there is a stress of about  $27 \text{ MPa}$ .

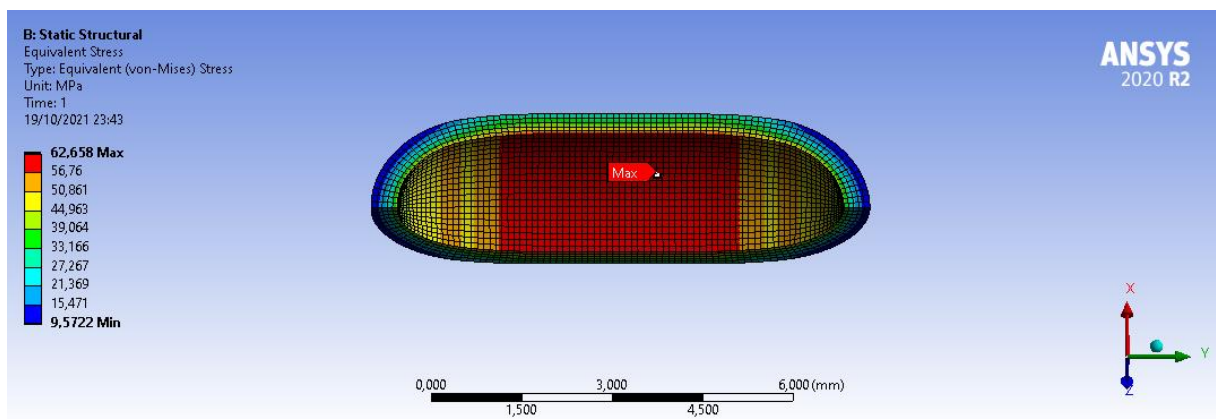


**Figure 1.9** Equivalent Stress of the 3D capsule-shaped model, maximum stress values.

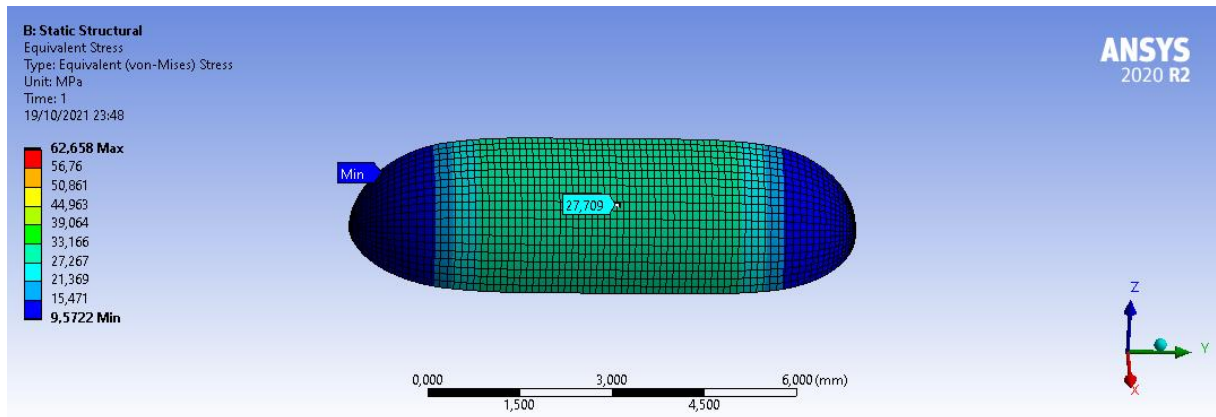


**Figure 1.10** Equivalent Stress of the 3D capsule-shaped model, minimum stress values.

According to the results of the FEM structural analysis of the capsule-like reservoir, several observations can be made as for the other model. Once again, the properties of the material fully meet our requirements by ensuring high mechanical resistance to internal pressures. In the present case, the geometry used allows for more homogeneously distributed deformations and lower maximum stress and strain values. One more time we wonder about the right spot where the strain gauge can be glued. The external cylindrical surface assures an excellent surface for this purpose and a consistent deformation that can allow good strain detections. Moreover, the simplicity of the geometry can lead to a better production process of the device.

### 1.3 Design of the test capsule sample (disc-shaped capsule)

In the previous paragraphs we analyzed two possible design solutions for our device, both with a cylindrical shape. From this first analysis, some advantages and disadvantages associated with the selected geometries emerged. A possible improvement is certainly reducing the size of the capsule. Following consultation with the Houston Methodist Research Institute, we decided to design and analyze a disc-shaped reservoir. First of all, this design allows for smaller dimensions but guarantees two large surfaces on which to install strain gauges, i.e. the upper and lower face of the disc. Furthermore, the simplicity of the geometry facilitates the realization of the samples. Some samples with this form had previously been used in Dr. Grattoni's lab for *in vivo* testing with the nanofluidic membrane. A number of them will then be tested in our laboratory.

### 1.3.1 Capsule geometry

The first step is the definition of the geometry of the capsule realizing a 3D CAD model using Solidworks. The main dimensions were agreed on cooperation with the Houston Methodist Research Institute.

Geometry specifications are the following:

- external radius: 12,5 mm
- internal radius: 11 mm
- height: 6 mm
- fillet radius: 1 mm
- lateral wall thickness: 1,5 mm
- upper/lower wall thickness: 0,5 mm

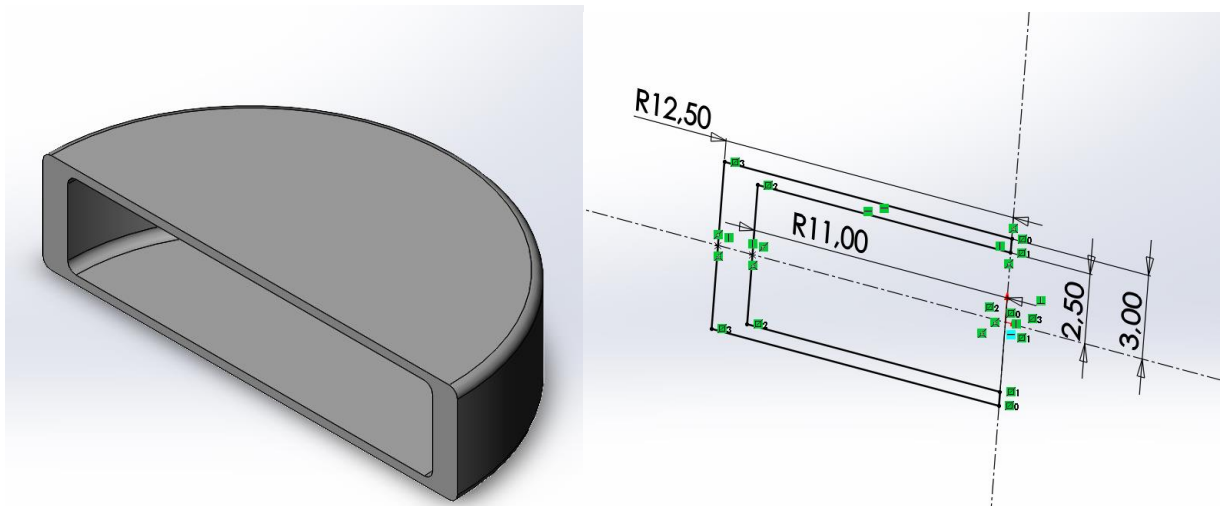


*Figure 1.11* 3D CAD model of the disc-shape reservoir.

### 1.3.2 FEM static structural analysis and results

As for the cylindrical capsules, a FEM static structural analysis of the model was performed using ANSYS Workbench software. Even in this case, we realized the mesh of the model with the «Sweep Method» mesh function described previously. As far as the results are concerned, we focused on:

- equivalent stress (Von Mises) in [MPa]
- equivalent elastic strain (Von Mises) in [mm/mm]

Also in this analysis, we used an internal pressure of 20 MPa and titanium alloy Ti6Al4V was chosen as the reference material.

Results from the FEM structural analysis for the disc-shaped capsule are presented below.

#### EQUIVALENT ELASTIC STRAIN (VON MISES) – DISC-SHAPED MODEL

Von Mises approach is chosen to compute the overall elastic strain value of the reservoir. In Figure 1.12, the internal pressure of 20 MPa brings to a maximum strain of  $3,3335 \cdot 10^{-2} \text{ mm/mm}$  at the inner edge of the lower and upper side of the disc-like reservoir. A large strain of  $1,863 \cdot 10^{-2} \text{ mm/mm}$  is present around the center of the top and bottom surface. The regions of minimum strain are located at the center of the upper and lower internal circular surfaces.

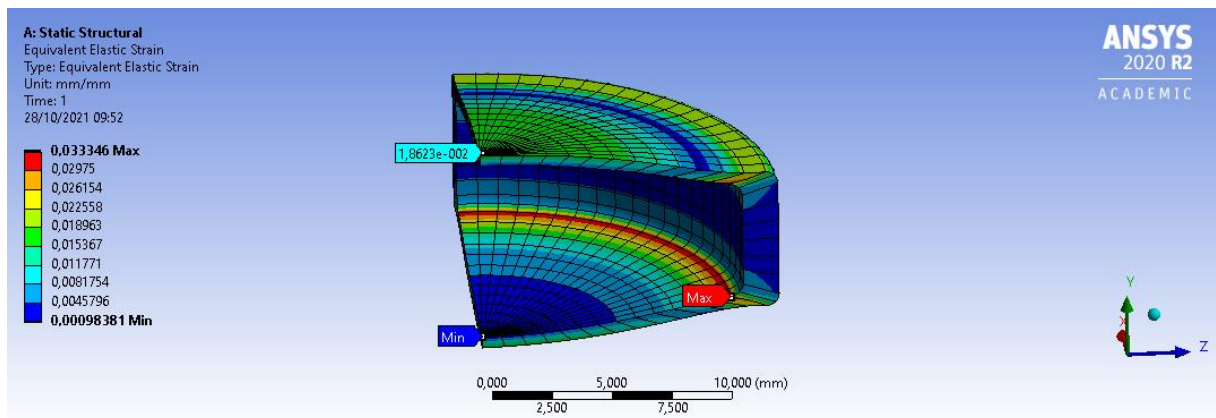


**Figure 1.12** Equivalent Elastic Strain of the 3D disc-shaped model.

## EQUIVALENT STRESS (VON MISES) – DISC-SHAPED MODEL

The maximum distortion criterion (Von Mises) was used to approximate the overall stress value of the capsule. The situation reflects that analyzed for the corresponding elastic strain. Situated at the inner edge of the top and bottom of the disc-like capsule, Figure 1.13 shows a maximum stress value of  $3198,6 \text{ MPa}$ . High stresses ( $\cong 1700 \text{ MPa}$ ) are present in correspondence with the center of the outer circles which form the top and the bottom of the reservoir. A minimum stress value of  $94,4 \text{ MPa}$  is positioned at the center of the upper and lower internal circular surfaces.

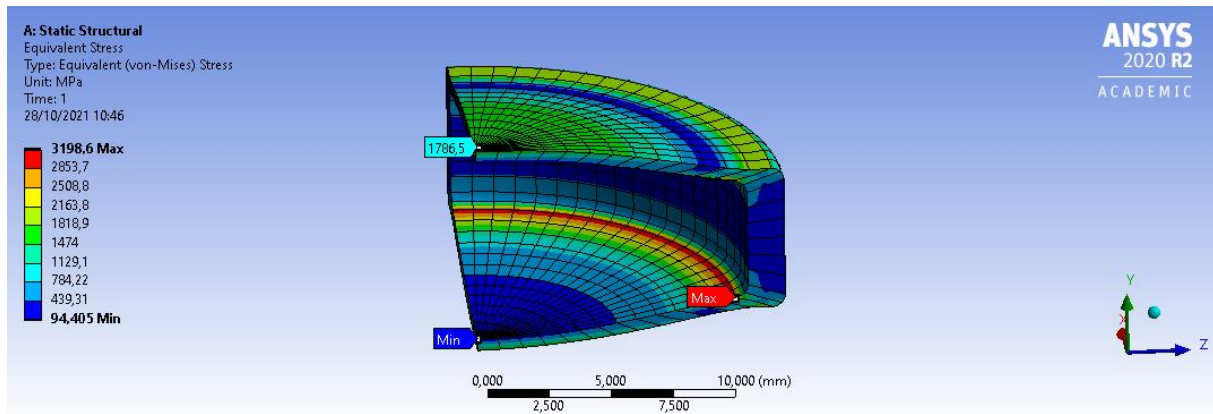


*Figure 1.13* Equivalent Stress of the 3D disc-shaped model.

Once again, some observations can be made about the material used and the geometry of the model. Even though, for this model, we have an increase in stress and strain values compared to the previous configurations, the use of a titanium alloy appears a valid option. As already explained, our implantable system should normally operate with osmotic pressures ranging from few bars up to about 10 bars, but the internal pressure of the model was set at a much higher level to accentuate possible critical issues. As mentioned above, the disc-like structure has two large surfaces in correspondence of the outer areas that forms the bottom and the top of the reservoir. In the central region of these surfaces, due to the effect of the internal pressure, there are considerable strains that can provide great sensitivity to the sensor. In addition, these areas are flat and therefore promote sensor bonding. This reservoir has a simple geometry, thus it could be easily produced using a variety of manufacturing techniques.

For all the reasons discussed above, we decided to adopt this design to make the samples to conduct our experiments.

## 1.4 Overcoming the problem of external stresses

Sensorizing an implantable device with strain gauges, to measure the internal pressure that controls drug release, presents some difficulties. An intrinsic problem with this measurement system is the fact that it is necessary to discriminate the pressure induced by the nanofluidic membrane and that produced by an external stress. Depending on the anatomical position in which the device will be implanted, it could be possible to calibrate the strain gauge, within certain limits, so that it can measure correctly. However, the system may be subject to external forces that would compromise its measurements. Inside the human body, the environment rarely maintains itself under constant pressure. Moreover, this problem is accentuated if the device is positioned subcutaneously or intramuscularly. In addition, it should be recalled that the strain gauge is a delicate sensor that must not suffer from strong external forces.

### 1.4.1 Protective external shell

A first intuitive approach to the problem is to equip our device with a protective external shell. This cover must protect the capsule from external stresses and at the same time guarantee free expansion or contraction of the sensorized surface, where the strain gauge is bonded, due to the variation of osmotic pressure. Figure 1.14 shows the 3D CAD model of the assembly, consisting of a disk-shaped capsule and its protective shell, made with Solidworks. The reservoir is connected to the shell by means of a circular joint arranged along the external circumference. In this assembly, the strain gauge can be placed on the top or bottom circular surface. The capsule is now confined within the shell with sufficient space to be able to expand.

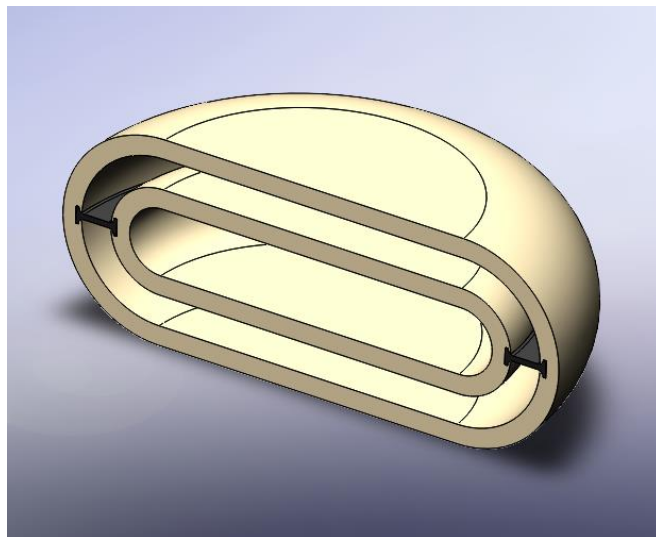


**Figure 1.14** 3D CAD assembly of capsule and its protective shell.

A different capsule model was used to conduct this analysis than the one that will be used to produce the samples. In the present case, both the capsule and the shell have rounded side walls. In Figure 1.15, the dimensions of the sketch are illustrated. In particular, the upper and lower circular surfaces have a radius equal to  $2,80\text{ mm}$ . The external radius of the capsule side wall is  $0,95\text{ mm}$  whereas the external radius of the cover is  $1,85\text{ mm}$ . A distance of  $0,55\text{ mm}$  is maintained between the outer surface of the capsule and the inner surface of the shell. The circular joint has a total height of  $0,05\text{ mm}$ .

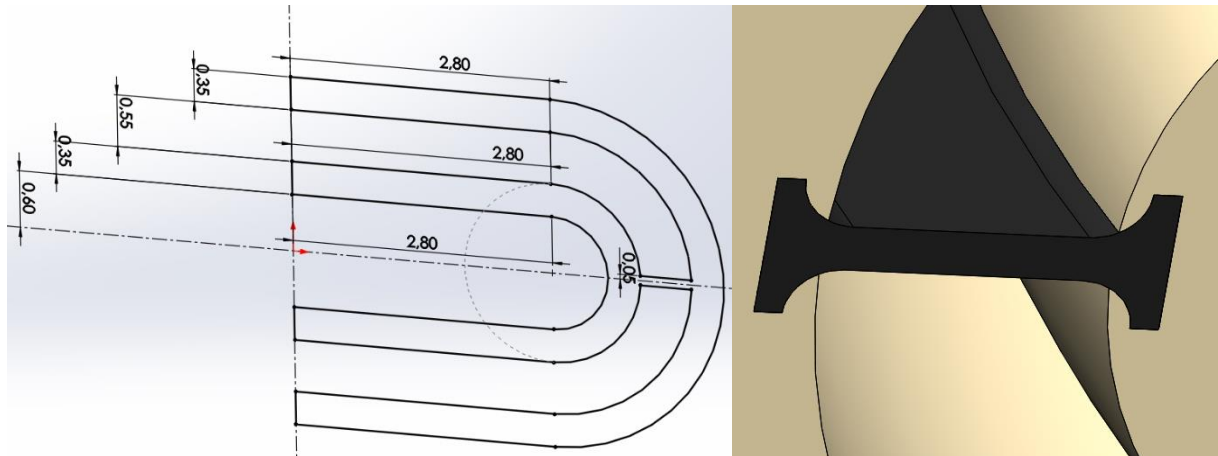


*Figure 1.15* Sketch dimensions of the assembly and detail view of the circular joint.

## FEM structural analysis

To evaluate this protection system from external stresses, a FEM analysis was performed. We envisioned a situation where the device was implanted inside the human body and subjected to a sudden force, perpendicular to the external circular surface of the shell.

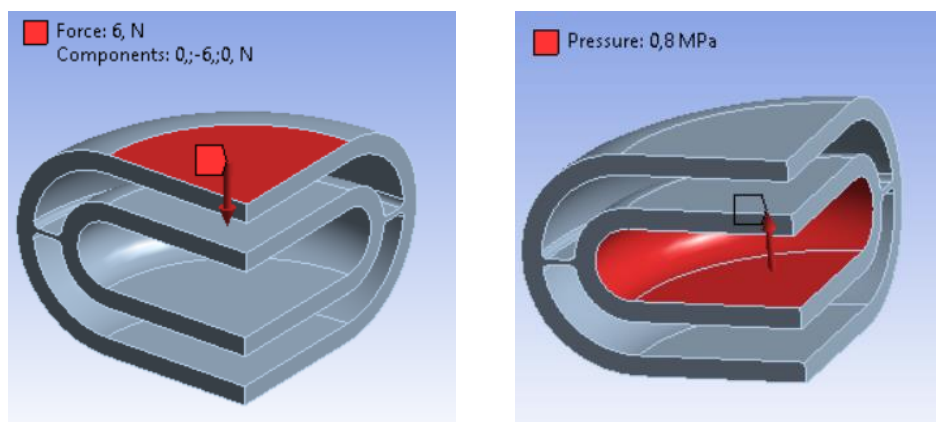


*Figure 1.16* External force on the shell and working osmotic pressure of the capsule.

Therefore, we loaded the capsule with an internal pressure of  $0,8 \text{ MPa}$ , i.e. during a typical operating condition. Selected pressure value is reached with a 1 second ramp in the first load step. Then we imposed a following load step in which the force acting on the shell reaches a maximum value of  $6 \text{ N}$  after 1 second (Figure 1.17). The force vector is distributed across the flat face marked in red in Figure 1.16.

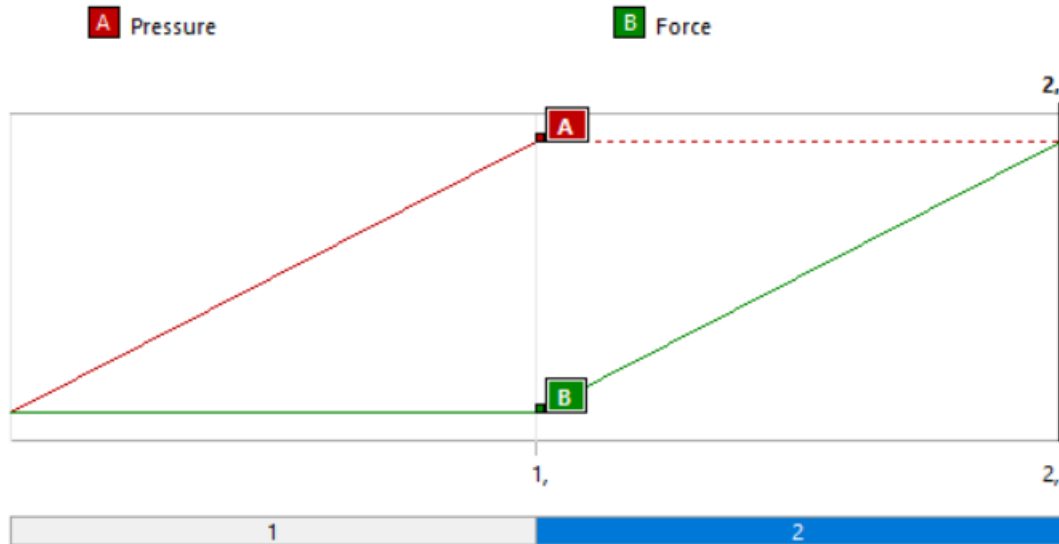


**Figure 1.17** Load steps of the FEM model.

In order to make the analysis as realistic as possible, the circular external surface of the shell, opposite to that which undergoes external force, is constrained with an elastic support of  $2 \text{ N/mm}^2$  that allows the face to move and deform according to a spring behavior.

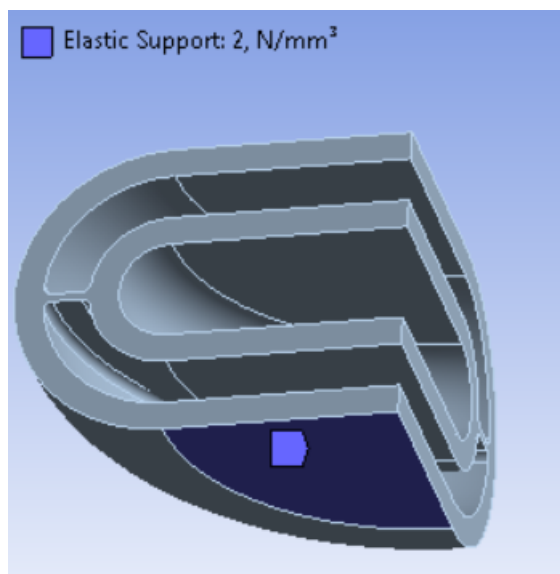


**Figure 1.18** Load steps of the FEM model.

First, we analyze what happens when the external load to the device is not yet applied but the internal pressure is set to the maximum (0,8 MPa). Once more, we focused on the equivalent elastic strain (Von Mises) in [mm/mm] and the equivalent stress (Von Mises) in [MPa].

However, this time we selected a different material for the device, i.e. polyester resin which is a synthetic resin mainly used in the construction of molded reinforced fibers and composite products. Figure 1.19 illustrates the principal proprieties of the material.

Resin Polyester	
Density	1,2e-06 kg/mm <sup>3</sup>
<b>Structural</b>	
▼ Isotropic Elasticity	
Derive from	Young's Modulus and Poisson's Ratio
Young's Modulus	3000,0 MPa
Poisson's Ratio	0,31600
Bulk Modulus	2717,4 MPa
Shear Modulus	1139,8 MPa
<b>Other</b>	
▼ Ply Type	
source	ACP
Type	Isotropic

Figure 1.19 Resin Polyester properties.

### EQUIVALENT ELASTIC STRAIN (VON MISES) – SHELL NOT LOADED

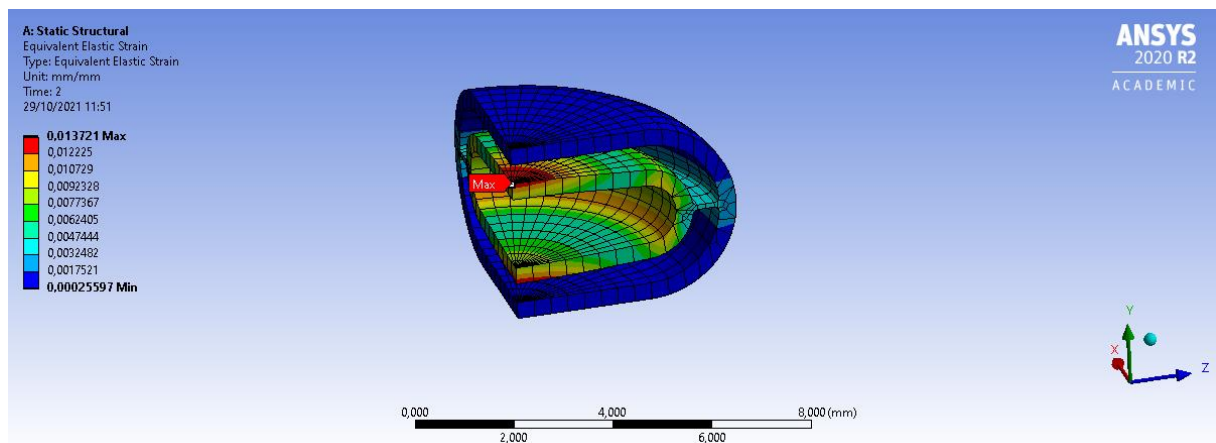
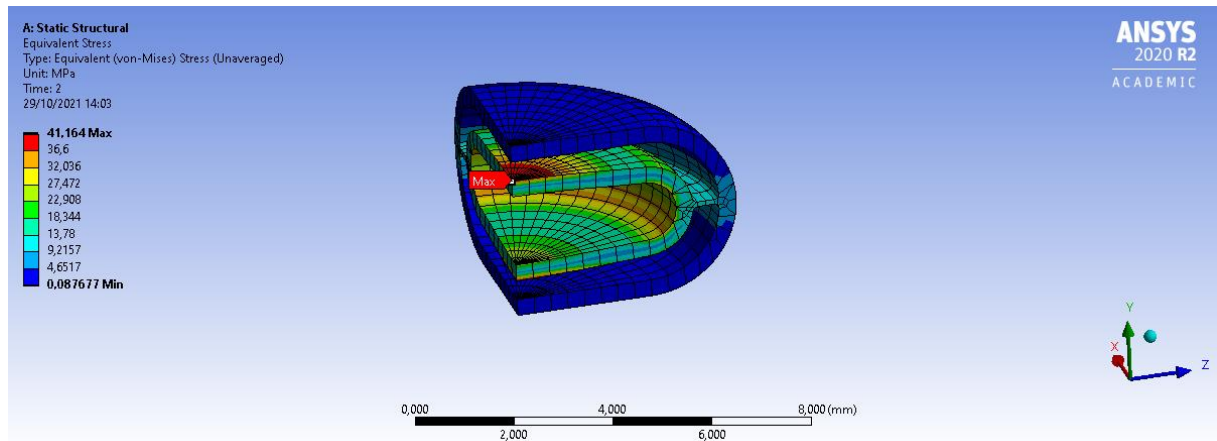


Figure 1.20 Equivalent Elastic Strain of the 3D CAD assembly without external force on the shell.

Figure 1.20 shows the overall elastic strain values of the model, computed according to Von Mises method. The external force is not present, and the capsule is loaded with an internal pressure. It can be noticed that the maximum equivalent elastic strain, equal to  $1,3721 \cdot 10^{-2} \text{ mm/mm}$ , occurs in the central points of the upper and lower circular surfaces of the reservoir. The outer shell shows almost no deformation and low strain values are present in the circular joint around the capsule periphery.

### EQUIVALENT STRESS (VON MISES) – SHELL NOT LOADED



**Figure 1.21** Equivalent Stress of the 3D CAD assembly without external force on the shell.

Figure 1.21 illustrates the overall stress values of the capsule, computed using Von Mises criterion. The situation is consistent with the equivalent elastic strain analysis. The maximum equivalent stress occurs in the central points of the upper and lower circular surfaces of the reservoir and is equal to  $41,164 \text{ Mpa}$ .

### EQUIVALENT ELASTIC STRAIN (VON MISES) – SHELL LOADED

We therefore analyze the situation in which the capsule is loaded internally by the osmotic pressure and the shell is subjected to a perpendicular force to its flat surface. The force vector is oriented perpendicularly to the circular surface of the case and is distributed across the flat face. Figure 1.22 provides the overall elastic strain values of the model. As it can be seen from the figure below, the external force caused an evident elastic deformation of the upper and lower circular surfaces of the shell. However, the behavior of the reservoir, under internal pressure, is not much affected. The equivalent elastic strain in correspondence of the central points of the upper and lower circular surfaces of the capsule is equal to  $1,3017 \cdot 10^{-2} \text{ mm/mm}$ . This value is very similar to the one computed in the simulation without the external force. The maximum equivalent elastic strain, equal to  $2,1945 \cdot 10^{-2} \text{ mm/mm}$ , takes place in the central area of the internal surface of the shell loaded by the force.

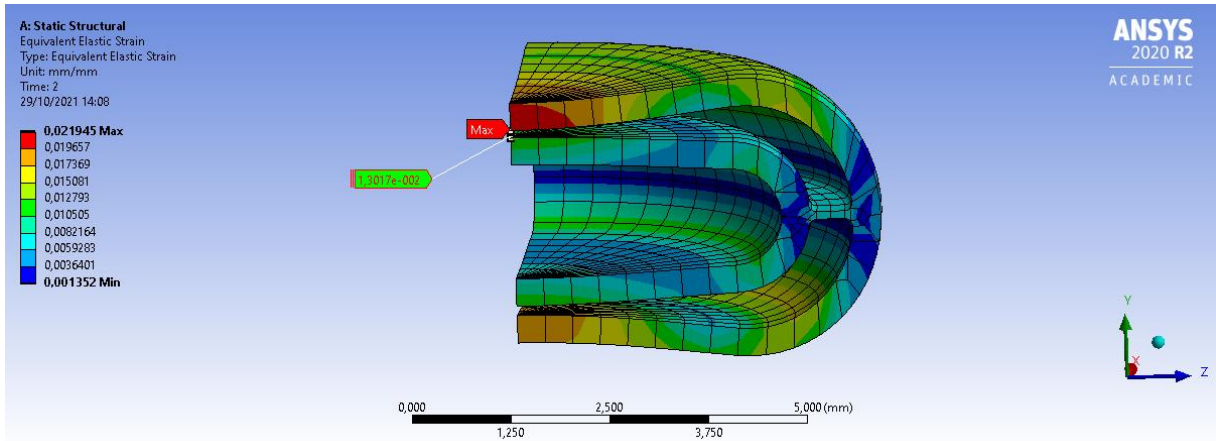


**Figure 1.22** Equivalent Elastic Strain of the 3D CAD assembly with external force on the shell.

### EQUIVALENT STRESS (VON MISES) – SHELL LOADED

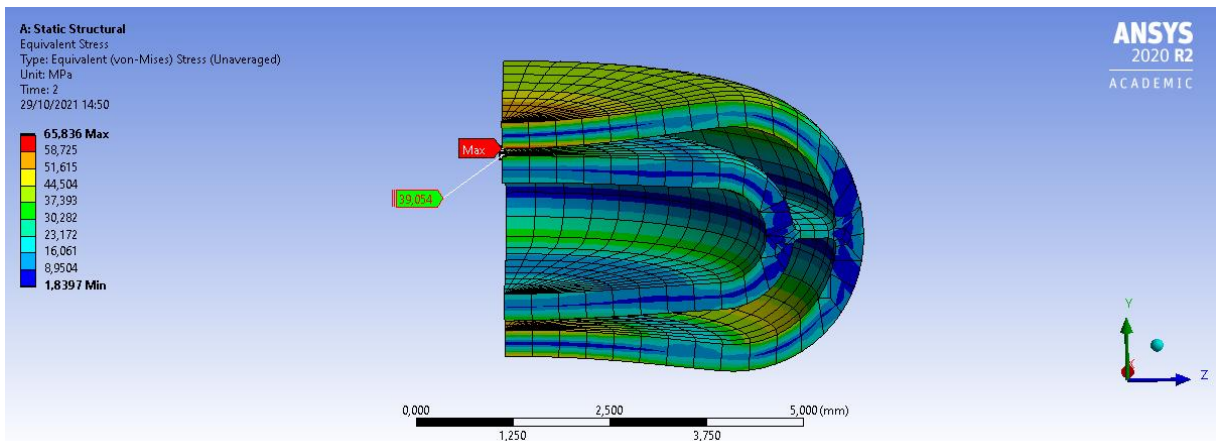


**Figure 1.23** Equivalent Stress of the 3D CAD assembly with external force on the shell.

Figure 1.23 above illustrates the simulation results as regards the overall stress values of the capsule, computed using Von Mises criterion. The equivalent stress in correspondence of the central points of the upper and lower circular surfaces of the reservoir is equal to  $39,054 \text{ MPa}$ . This value is very close to the one calculated in the simulation without the external force. The maximum equivalent stress, equal to  $65,836 \text{ MPa}$ , occurs in the central area of the internal surface of the shell loaded by the force.

This initial approach to ensure that no external stresses interfere with the measurement of internal pressure, seems to promise good results but there is still a lot to study in order to design a shell that allows the correct functioning of the device.

## Chapter 2

# Introduction to Strain Gauges

### 2.1 Overview of Electrical Strain Gauges

A strain gauge (also spelled strain gage) is a mechanical sensor used to measure the deformations of a body. Electrical strain gauges are transducers that convert strain measurements into electrical signals. There are different electrical strain gauges, but the resistance electrical strain gauge is the most largely used. It consists of an insulating elastic backing in which a metallic foil pattern is fixed. The gauge is then secured to the object by means of a proper adhesive. When the body is deformed, the foil is deformed, resulting in its change of electrical resistance [2, 3].

A strain gauge exploits the property of electrical conductance and its reliance on the conductor geometry. When an electrical conductor is stretched inside its elastic limits such that there is no breaking or permanent deformation, it will become thinner and longer, which increases its electrical resistance from end to end. On the contrary, when a conductor is compressed such that it does not crumple, it will become larger and shorter, which decreases its electrical resistance from end to end. The amount of induced stress can be derived from the measured electrical resistance of the strain gauge [3].

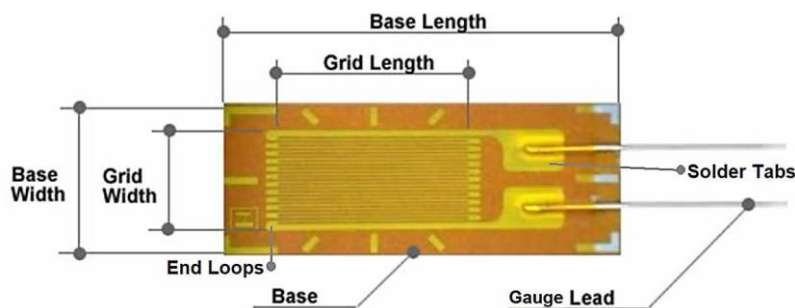


**Figure 2.1** Strain gauge and its parts [4, Showa Measuring Instruments Co., 2018].

Figure 2.1 shows the elements of the strain gauge. Grid length is the operative extent that is useful in strain measurement, and the strain gauge measures along the grid (or gauge) length direction [4]. The interface between foils and the foil themselves generates, in the transversal direction, sensitivity to transverse displacement. The tabs localized in the right corner of Figure 2.1 are used for connecting the gauge. The gauge length of general-purpose gauges ranges from about 0.380 mm to 60 mm but in concrete applications it can reach up to 130 mm. The patterns of the foil, illustrated in the figure above, are first drawn to a large scale and then reduced optically to the desired size in the following step of manufacturing. The pattern is transferred to a metal foil with a light sensitive paint and then developed. Finally, the metal foils are engraved to obtain the individual gauges. The active elements of the foils are oriented in the longitudinal direction and connected at the end by small foil parts perpendicular to the

main elements of the active grid. These elements contribute to a transverse sensitivity of the gauge. The foils are attached to a backing material [2].

### 2.1.1 Backing Material

A strain gauge is very thin and delicate, making it hard to manipulate. It's necessary to use backing materials to allow proper handling and damage-free usage of strain gauges. Backing materials are typically dielectric in nature to offer excellent insulation between the specimen and strain gauge wires [4].

The backing material serves a variety of purposes:

- it supplies a support platform for the foil;
- it facilitates bonding operations on a surface;
- it ensures electrical insulation;

The operational temperature determines the type of backing. Two common backing materials are glass-fiber-reinforced epoxy-phenolic and polyamide. The backing is not an independent parameter but there is a specific combining of foil alloys and backing materials that works better than others for certain types of applications. Lists of gauges with backing and foil combinations are provided by manufacturers [2].

### 2.1.2 Adhesives

A very important contribution in the correct functioning of strain gauges is determined by the adhesive. The deformations are transmitted to the foil by the adhesive with the backing as an intermediate step. Cyanoacrylate is an instantaneous, solvent-free cement. It can be used in regular testing at room temperature. Epoxy-based adhesives are vastly accessible in different variations that can be applied at room temperature or by using heat [2]. For our applications we used a common brand of cyanoacrylate adhesive applied at room temperature to the prototypes. Before any attempt at adhesive application, it is of fundamental importance to clean with solvents the application surface of the test specimen to remove unwanted grease and dirt which would compromise the bonding with the strain gauge.

## 2.2 Gauge Factor

The gauge factor provides a correlation between the strain that is applied to a gauge and the corresponding resistance. It is significant to point out that the resistance of the gauge will depend on the applied strain. Therefore, the gage factor  $F_G$  is defined as:

$$F_G = \frac{\Delta R/R_G}{\Delta L/L} = \frac{\Delta R/R_G}{\varepsilon} \quad (2.1)$$

With  $\Delta R$  = the change in resistance caused by strain,  $R_G$  = electrical resistance of the undeformed gauge,  $L$  = length of strain-sensitive element and  $\varepsilon$  = normal or axial strain. Consequently, the change in resistance per unit of original resistance that occurs per unit of strain applied is evaluated by the gauge factor.

The gauge sensitivity  $S$  is determined as:

$$S = \Delta R / \varepsilon \quad (2.2)$$

The electrical resistance in Ohms is chosen by the maker for different types of applications [2].

### 2.2.1 Measuring grid material

The measuring grid material must fulfil several requirements that can partly clash, depending on the aimed application; in particular, large extensibility and high fatigue strength are not easy to accomplish simultaneously. It is necessary to gain the best achievable linear, reproducible correlation between the strain and the change in resistance, that must have the minimum hysteresis as well [5].

The alloy most widely used as a grid material is constantan. It commonly consists of 55% copper and 45% nickel, but the actual percentage composition may differ of  $\pm 5\%$ . Constantan possesses the most versatile characteristics for applications at temperatures between  $50^\circ\text{C}$  and  $+180^\circ\text{C}$ . Its high sensitivity to strain (i.e. the relationship between change of strain and change of resistance) is barely influenced by temperature and strain. Constantan has a specific resistance ( $\cong 0.49 \Omega\text{mm}^2/\text{m}$ ) sufficiently high to manufacture strain gauges with the typical nominal resistances in convenient sizes [5].

Isoelastic alloy is mostly used for vibration and impact tests for its high capability to measure dynamic strain. This material also possesses higher sensitivity than constantan, therefore it has enhanced signal to noise ratio. Moreover, the major advantage of isoelastic alloy over constantan is its superior resistance, which is  $350 \Omega$  compared with  $120 \Omega$  of constantan. It also has better fatigue property than other strain gauge materials [4].

Another grid material is Karma (NiCr alloy) which possesses general properties comparable to constantan. Its major benefit is its efficient self-temperature compensation from  $-73$  to  $260^\circ\text{C}$ . It presents in addition higher cyclic strain resistance than constantan. However, this material is not easy to solder [4].

### 2.2.2 Temperature Effect

A strain gauge attached to a specimen, in an ideal case, would react only to the applied strain in the part and remain unaffected by other variables such as the environmental conditions. Regrettably, like all other sensors, the resistance strain gauge is somewhat less than perfect. Actually, the electrical resistance of the strain gauge changes not only with strain, but with temperature. Moreover, the correlation between strain and resistance changes, the gage factor varies with temperature. To conclude let us also remember that a difference exists between the thermal expansion of the gauge and the material where the gauge is pasted. All these factors are of careful attention and must be known if one wants to get correct readings. The specific resistance of a material is temperature dependent. In addition, this effect is not a small quantity that can be ignored; consequently, temperature effects are the main corrections that are necessary to obtain correct strain measurements [2].

## 2.3 Wheatstone Bridge Circuit

The Wheatstone bridge was invented by Samuel Hunter Christie in 1833. This measuring instrument was later improved and popularized by Sir Charles Wheatstone in 1843. Generally, reading instruments can differ significantly in their circuit details. Despite that, in most cases they are based on a certain form of the Wheatstone bridge circuit. The bridge circuit itself can be used in differing forms in different instruments, while the principle remains the same. Because of the numerous variations in instrument design, an entirely general coverage of the instrument is not functional [2].

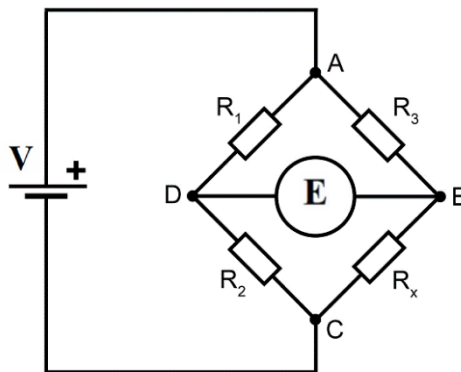


*Figure 2.2* Wheatstone Bridge Circuit [2].

Figure 2.2 illustrates a Wheatstone bridge which consists of a power supply that provides a constant potential  $V$  which is independent of the change in resistance. As illustrated in figure, the potential  $V$  is applied at points  $A$  and  $C$  of the bridge circuit. The diagonal  $BD$  instead includes an instrument that measures the balance of the bridge circuit. Basically, this instrument is used to evaluate an unknown electrical resistance by balancing two legs of the bridge, with one leg containing the unknown component. Its functioning is comparable to a potentiometer besides the fact that in potentiometer circuits the meter utilized is a sensitive galvanometer. On the right-handed side of the circuit illustrated in Figure 2.2,  $R_x$  is the unknown resistance to be gauged;  $R_1$ ,  $R_2$ , and  $R_3$  are resistors of known resistance which reduce current flow, and  $R_2$  has an adjustable resistance. The voltage between the points  $B$  and  $D$  will be zero and no current will flow through the galvanometer if the ratio of the two resistances in the known leg ( $R_2 / R_1$ ) is equal to the ratio of the two resistances in the unknown leg ( $R_x / R_3$ ). In consequence then  $R_2$  is varied until this condition is achieved. The actual direction of the current indicates whether  $R_2$  is too high or too low. The detection of a null current can be carried out with extremely high precision. Thus, if  $R_1$ ,  $R_2$  and  $R_3$  are known to a high accuracy, then also  $R_x$  can be measured to high accuracy. Very small  $R_x$  changes disturb the equilibrium and are promptly detected. At the balance point, the ratio of  $(R_2 / R_1) = (R_x / R_3)$ . Hence, with the following equation  $R_x = (R_2/R_1) \cdot R_3$ , we can easily get  $R_x$  [2].

The Wheatstone bridge circuit is widely employed in many strain gauge applications. Moreover, this instrumentation can be connected to a computer through a multichannel acquisition system to manage and store large quantities of data. With reference to the Figure 2.3, by applying a voltage  $V$  at the points AC with a power source, the voltage  $E$  between BD is measured and it is given by the equation below [4]:

$$E = V_{BD} = V_{AB} - V_{AD} \quad (2.3)$$

where the voltages AB and AD are specified as:

$$V_{AB} = \frac{R_1}{R_1+R_2} V \quad (2.4)$$

$$V_{AD} = \frac{R_4}{R_3+R_4} V \quad (2.5)$$

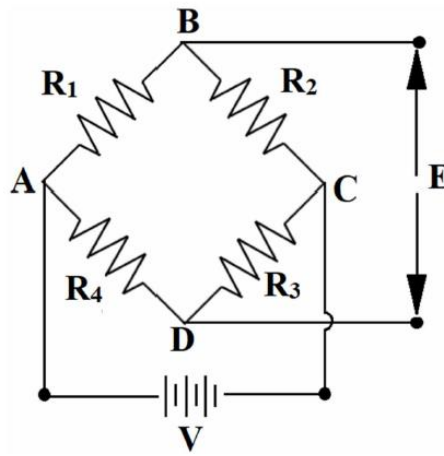


Figure 2.3 Wheatstone Bridge Circuit [4].

Eventually, the voltage  $E$  is given as detailed below:

$$E = V_{BD} = V_{AB} - V_{AD} = \frac{R_1 R_3 - R_2 R_4}{(R_1 + R_2)(R_3 + R_4)} V \quad (2.6)$$

Initially  $E = 0$  which means the bridge circuit is balanced; this condition is achieved when  $R_1 R_3 = R_2 R_4$ . Nevertheless, when the bridge balance is disturbed, then the output voltage  $E$  for a change of incremental resistance is indicated as follows:

$$\Delta E = V \frac{R_1 R_2}{(R_1 + R_2)^2} \left( \frac{\Delta R_1}{R_1} - \frac{\Delta R_2}{R_2} + \frac{\Delta R_3}{R_3} - \frac{\Delta R_4}{R_4} \right) \quad (2.7)$$

By recalling (2.1) we get:

$$\frac{\Delta R}{R} = F_G \varepsilon \quad (2.8)$$

In many cases, the bridge circuit consists of equal resistances ( $R_1 = R_2 = R_3 = R_4$ ); thus, by means of (2.8), the equation (2.7) can be written as:

$$\Delta E = \frac{F_G E}{4} (\varepsilon_1 - \varepsilon_2 + \varepsilon_3 - \varepsilon_4) \quad (2.9)$$

Therefore, by replacing resistances with strain gauges, (2.9) shows that the relative deformations of gauges installed in adjacent arms of the bridge subtract from each other and the relative deformations of gauges installed in opposite arms add to each other. This feature is widely used in strain measurements to compensate for effects such as temperature or to increase signal force. The four arms can be formed by strain gauges or they may be in part occupied by strain gauges [2, 4].

### 2.3.1 Strain Measurement using the Wheatstone Bridge

The Wheatstone Bridge circuit can have one or more arms occupied by strain gauges and by connecting the other arms with known resistances the output voltage  $\Delta E$  can be measured. From the voltage variation  $\Delta E$ , follows an equivalent change in resistance, thus further strain can be evaluated. By connecting the measuring instrumentation to a PC, a large amount of data can be stored and processed to get the strain as output. There are two possible ways to perform the measurement of strain:

1. Directly measure  $\Delta E$  and then derive the strain from the measured  $\Delta E$ . This method is helpful for strain measurement at both static and dynamic conditions. Before measuring the strain, the main prerequisite is that the bridge must be balanced initially.
2. When loading the specimen, after firstly balancing the bridge circuit, the strain is induced in the specimen. The strain is causing the bridge to become unbalanced. Therefore, the resistive balance of the bridge can be adjusted to rebalance it (i.e.,  $\Delta E = 0$ ). The strain can be evaluated from the value of the resistive balance required for rebalancing the bridge. This technique applies primarily to static deformation measures. Moreover, this method can offer great accuracy, even if the process is very slow.

Direct  $\Delta E$  measurement is a very convenient technique and applies to both static and dynamic strain measurements [4].

### 2.3.2 Bridge Sensitivity

A metallic foil forms the strain gauge, which is connected to a bridge circuit to evaluate the electrical signal, so the equivalent strain can be measured. At all stages, sensitivity is involved, and it is necessary to understand sensitivity when every form is taken by the wire during strain measurement. Wheatstone Bridge sensitivity needs to be determined as well, since it is used to transform the resistance variation into an output voltage signal. The sensitivity of the bridge depends on the magnitude of bridge voltage ( $V$ ), the gauge factor ( $F_G$ ), the bridge factor ( $n$ ), and the ratio of resistance ( $m$ ), that is  $R_2/R_1$ . Consequently, the output voltage of the Wheatstone bridge can be re-written by integrating the above-stated factors as follows [4]:

$$\Delta E = V \frac{R_1 R_2}{(R_1 + R_2)^2} n \left( \frac{\Delta R}{R} \right) \quad (2.10)$$

where the term  $\Delta R/R$  is the resistance ratio of Equation 2.1 and can be re-written in terms of  $F_G$ ; also, recalling  $m (= R_2/R_1)$ , Equation 1.10 is revised as below:

$$\Delta E = V \frac{m}{(1+m)^2} n F_G \varepsilon \quad (2.11)$$

The last equation shows that the magnitude of the output signal  $\Delta E$  can be increased by properly controlling  $m$  and  $n$ . The latter parameter is the bridge factor that can be 1, 2, and 4 for the quarter, half, and full-bridge configuration, respectively. It is necessary to evaluate  $m$ , since it can be controlled to

reach the maximum signal for strain measurement. Figure 1.4 spotlights that, when  $m = 1$ , the ratio  $m/(m + 1)^2$  is maximum, thus, by achieving such a state, the output signal can be improved to facilitate the measurement of the deformation. Thus, sensitivity can be increased by adjusting the resistance ratio ( $m$ ), for any given bridge with constant  $V$ ,  $F_G$ , and  $n$  [4].

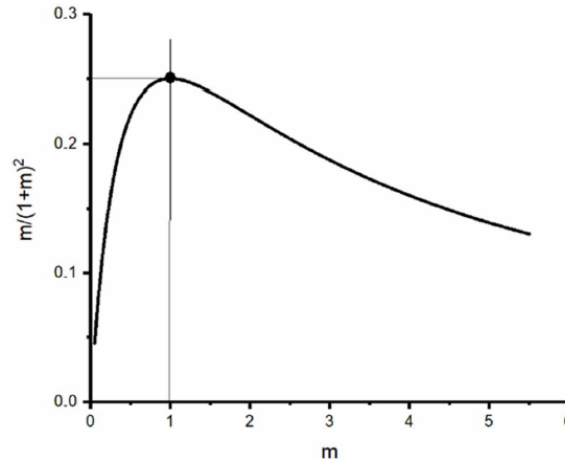


**Figure 2.3** Influence of resistance ratio in the output voltage [4].

### 2.3.3 Bridge Factor

The bridge factor ( $n$ ) indicates the number of active strain gauges in a Wheatstone Bridge circuit. Besides the resistance ratio,  $n$  is another factor that can be used to increase the output voltage. Quarter, half, and full bridge circuit configurations are currently used nowadays in the applications. Each bridge circuit is examined in the following paragraphs [4].

### 2.3.4 Quarter Bridge Configuration

The quarter bridge configuration is displayed in Figure 2.4, where one resistance arm is replaced with a strain gage. This arrangement is very commonly used for experimental stress analysis goals. The quarter bridge configuration can be adopted for both bending and axial strain measurement. The strain gauge must be positioned such that the gauge length is along the longitudinal axis of the specimen to measure the strain. The bridge factor for this setup is  $n = 1$ . Figure 2.4 illustrates an example where the strain gauge is set up to measure  $+\varepsilon$  (i.e. elongation due to the applied load). This arrangement has a major drawback, which is the temperature effect may compromise the accuracy. Consequently, in requests where the temperature is significant, this setup can be less preferred for the measurement. Moreover, the cables themselves may undergo resistance changes due to the effects of temperature. Though, a dummy strain gauge ( $R_2$ ) can be coupled to the bridge to compensate the temperature effects in the quarter bridge. The identical dummy gauge is mounted on an unstrained specimen made of the same material of the test part. The active ( $R_1$ ) and dummy ( $R_2$ ) strain gauge are subjected to the same temperature, and its effect can be nullified in the resistance ratio [4, 2].

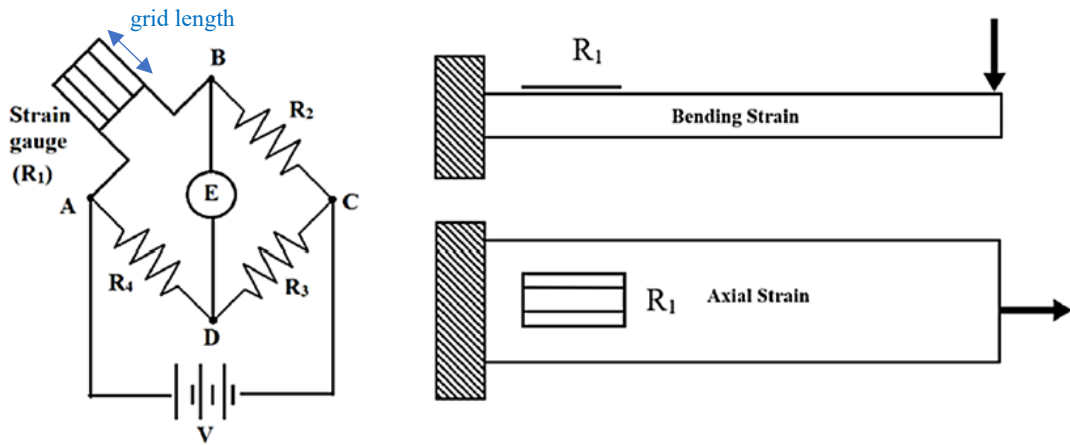


Figure 2.4 Wheatstone bridge circuit for quarter bridge configuration [4].

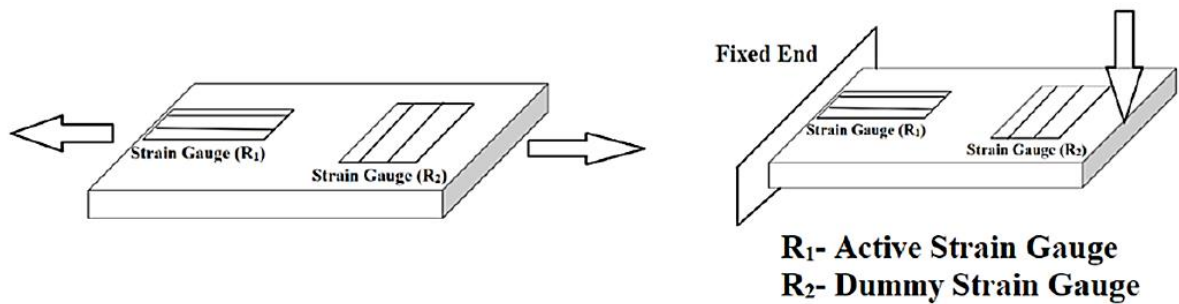


Figure 2.5 Quarter bridge configuration II [4].

### 2.3.5 Half-Bridge Configuration

In the half-bridge arrangement, the bridge factor is  $n = 2$  i.e. two active strain gauges are applied to measure the strain (Figure 2.6). As can be seen in Figure 2.6 allows the two strain gauges  $R_1$  and  $R_2$  are bonded to the top and the bottom of the specimen, The two active strain gauges are connected to adjacent arms of the bridge and for a given direction of loading,  $R_1$  can measure the tensile strain and  $R_2$  can measure the compressive strain. However, if they were connected to opposite arms of the circuit, as  $R_1$  and  $R_3$  in Figure 2.6, then the bridge could not read any output, though there would be strain in the loaded test part. This is because of the configuration of the bridge. The induced variation in resistance annuls them in the bridge circuit (Equation 2.7) and may measure zero output voltage. Therefore, knowledge of the mechanics of material is necessary when applying strain gauges to measure the deformation. Typically, two strain gauges are used when the signal is low and amplification is required. Alternatively, a quarter bridge arrangement can meet the requirement for the application of cantilever for bending strain. Also, the half-bridge layout provides better temperature advantages than the quarter bridge. Configuration II of the half-bridge circuit (Figure 2.7) can also be used, which can evaluate both axial and bending strain, depending on the input load. The  $R_2$  resistance, aligned with transverse strain, is supplied to offset Poisson's effect on strain measurement. This arrangement is comparable to the

quarter-bridge configuration II of Figure 2.5, though, now the strain gauge is active unlike in the quarter-bridge, where one is active and the other is dummy. In addition, the dummy strain gage of quarter-bridge configuration II is not bonded to the test part, whereas in the half-bridge configuration II both the strain gages are attached.  $R_2$  can also be used to measure Poisson's ratio of the sample during axial loading [4].

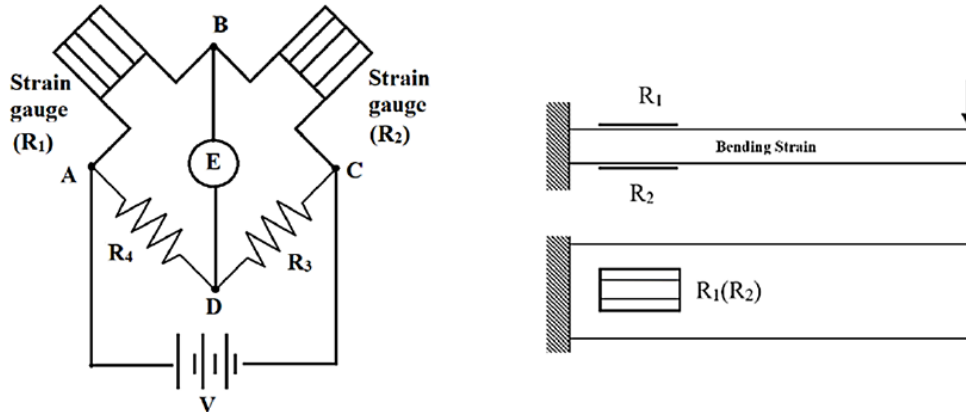


Figure 2.6 Wheatstone bridge circuit for half-bridge configuration [4].

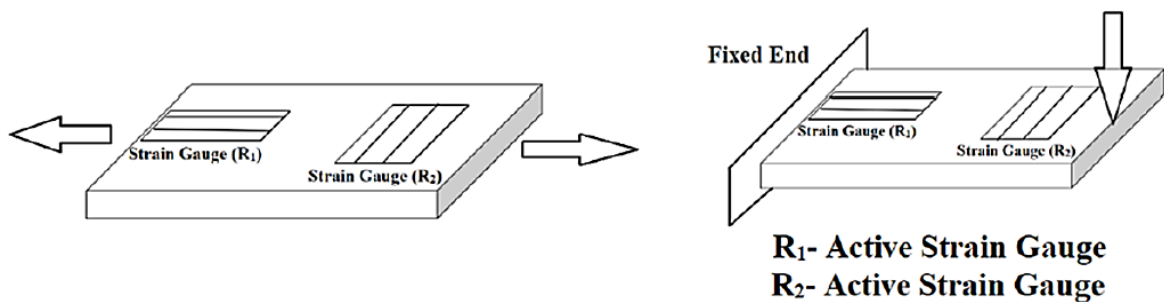


Figure 2.7 Half-bridge configuration II [4].

### 2.3.6 Full Bridge Configuration

Figure 2.8 shows the full-bridge configuration where all four arms of the Wheatstone bridge are formed by the strain gauges. The bridge factor for full-bridge layout is  $n = 4$ . The advantage of this arrangement is that the temperature effect is minimal in comparison with other configurations. The connection concept for strain gauges in the Wheatstone bridge should follow the principle discussed in previous paragraphs. The strain gauge used to measure the tensile and compressive strain during bending loads, shall be connected to the adjacent arms, rather than to the opposite arms of the bridge. Be familiar with the mechanics of materials is necessary to connect strain gauges to the bridge circuit. The full-bridge arrangement can also be extended, like the half-bridge configuration II, to measure bending strain. This second configuration permit to minimize the temperature effect, and to measure Poisson's ratio [4].

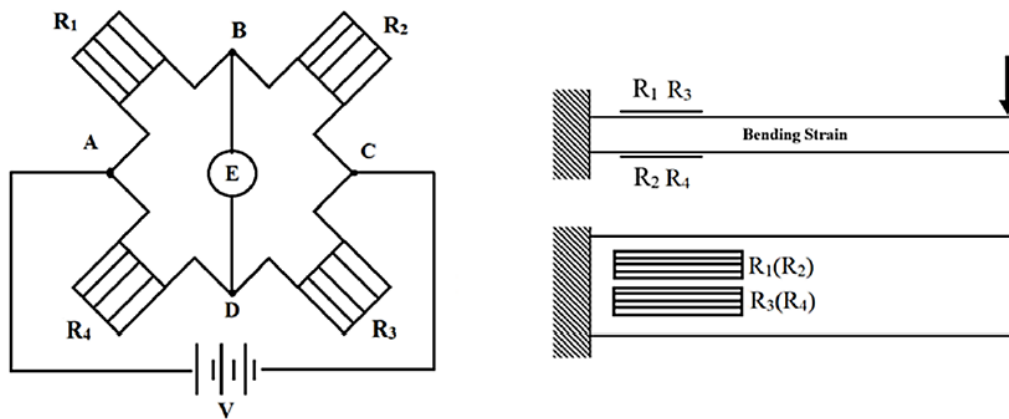


Figure 2.8 Wheatstone bridge circuit for full bridge configuration [4].

## 2.4 Strain Gauge Accuracy

Multiple factors determine the accuracy of the strain measurement. As previously discussed, it is important to be very careful from the beginning and during the measurement, since the measurement of the deformation is very small, and any small error can therefore be significant within this micrometric scale. Regular calibration is required to ensure the accuracy and linearity of the circuit itself. The strain gauges are fabricated with a resistance accuracy of  $\pm 0.3\%$  and the gauge factor accurate to  $\pm 0.5\%$ . Furthermore, it is essential to remember that the measurement of strain is also dependent on the installation procedure, the condition of strain being measured and the ambient conditions. Recently, strain gauge technology has reached such a development that it is possible to measure even  $0.5 \mu\epsilon$  with high accuracy [4, 2].

## 2.5 Strain Gauge Linearity, Hysteresis and Zero Drift

The strain gauge response must be linear and provide the same loading and unloading path. However, due to factors such as temperature effects, a cycle of mechanical hysteresis may be experienced by the strain gauge. This means that there is a difference between loading and unloading paths. Furthermore, the reading, when fully unloading the strain gauge, will not get back to zero and will have a non-zero value called zero drift (Figure 2.9). As a result of the input voltage  $V$ , the current flows through the wires of the strain gauge, causing a heat loss named  $I^2R$  loss. When the strain gauge is attached to materials with low thermal conductivity, the heat produced because of the applied current is not dissipated in an efficient way and built up in the sensor. As a result, this thermal build-up can cause hysteresis and zero drift. Consequently, the choice of materials, adhesive and backing material must be carefully carried out. In this respect, the calculations may include a provision to offset zero drift [4].

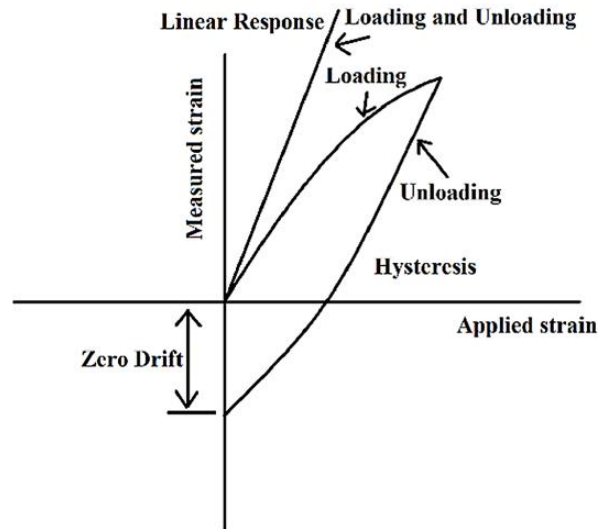


Figure 2.9 Response of strain gauge [4].

## 2.6 Strain Gauge Rosette

A strain gauge can evaluate the strain along its gauge length. Nevertheless, for many applications, the plane strain of a point on a free surface needs to be measured. For this request, three strain components must be determined. The strain at a point on a free surface is obtained by measuring the strain along three directions. When analyzing deformation with rosettes, the equations of the strain field can be referred to a system of coordinates  $x - y$ . In Figure 2.10, three strain gauges  $A$ ,  $B$ , and  $C$  are attached to the sample at a certain angle, and  $\theta_a$ ,  $\theta_b$ , and  $\theta_c$  are the angles of each strain gauge in relation to the reference  $x - y$  axis [4, 2].

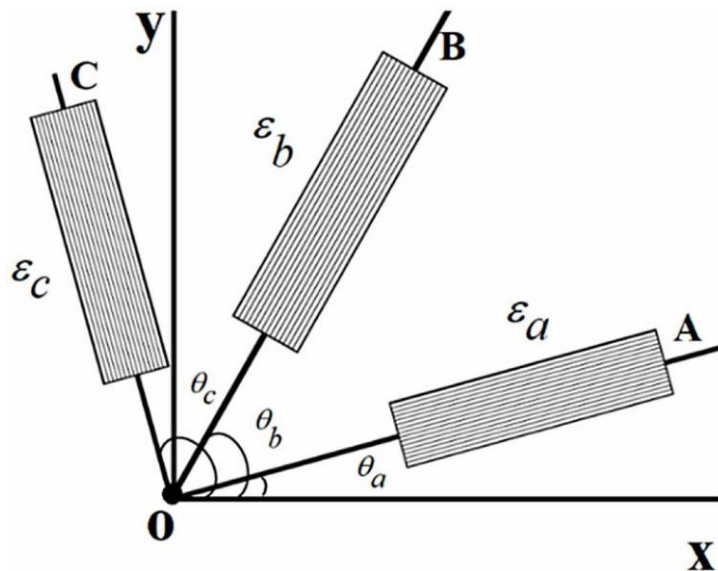


Figure 2.10 General strain rosette [4].

The strain measured by each strain gauge is  $\varepsilon_a$ ,  $\varepsilon_b$ , and  $\varepsilon_c$  and can be associated to the normal and shear strain by using the transformation law reported below [4]:

$$\varepsilon_i = \frac{\varepsilon_x + \varepsilon_y}{2} + \frac{\varepsilon_x - \varepsilon_y}{2} \cos 2\theta + \gamma_{xy} \sin 2\theta \quad (2.12)$$

$\varepsilon_i$  is the strain along a generic axis  $I$ ,  $\varepsilon_x$  and  $\varepsilon_y$  represents the normal strains along the  $x$  and  $y$  axis,  $\gamma_{xy}$  is the shear strain, and  $\theta$  is the angle of the  $I$  axis in relation to the reference  $x - y$  axis. For the strain gauge configuration illustrated in Figure 2.10, (2.12) can be re-written in this way [4]:

$$\varepsilon_a = \frac{\varepsilon_x + \varepsilon_y}{2} + \frac{\varepsilon_x - \varepsilon_y}{2} \cos 2\theta_a + \gamma_{xy} \sin 2\theta_a \quad (2.13)$$

$$\varepsilon_b = \frac{\varepsilon_x + \varepsilon_y}{2} + \frac{\varepsilon_x - \varepsilon_y}{2} \cos 2\theta_b + \gamma_{xy} \sin 2\theta_b \quad (2.14)$$

$$\varepsilon_c = \frac{\varepsilon_x + \varepsilon_y}{2} + \frac{\varepsilon_x - \varepsilon_y}{2} \cos 2\theta_c + \gamma_{xy} \sin 2\theta_c \quad (2.15)$$

From the last three equations, the normal strains  $\varepsilon_x$  and  $\varepsilon_y$ , and the shear strain  $\gamma_{xy}$  can be calculated. The effective use of a strain gauge rosette requires a clear understanding of the law of strain transformation. The  $45^\circ$  and  $60^\circ$  strain gauge rosettes are the most commonly used strain rosettes. Although, the arrangement of strain gauges can be positioned at any angle to measure the strain at a point on a free surface, and, therefore, the transformation law (2.12) can be applied using the corresponding angles of the strain gauges [4].

### 2.6.1 Three Element $45^\circ$ Rectangular Rosette

In this layout, two strain gauges (that measure respectively  $\varepsilon_a$  and  $\varepsilon_b$ ) are lined up along  $x$  and  $y$  axis and a third strain gauge is attached at  $45^\circ$  to the  $x$  axis (Figure 2.11). For this arrangement, the angle  $\theta_a = 0^\circ$ ,  $\theta_b = 45^\circ$  and  $\theta_c = 0^\circ$ . Thus, the transformation law (2.12) can be applied and solved for the normal strains and the shear strain. This result in [4]:

$$\varepsilon_x = \varepsilon_a \quad (1.16)$$

$$\varepsilon_y = \varepsilon_b \quad (1.17)$$

$$\gamma_{xy} = \varepsilon_b - \frac{\varepsilon_a + \varepsilon_c}{2} \quad (1.18)$$

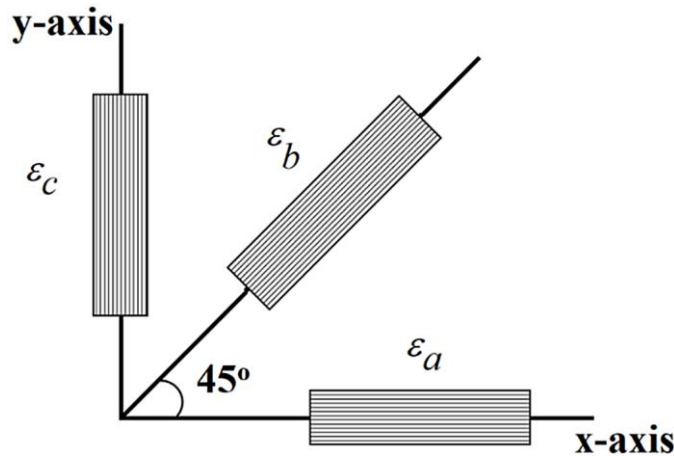


Figure 2.11 Rectangular strain gauge rosette [4].

### 2.6.2 Three Element 60° Delta Rosette

In this arrangement, two strain gauges (that measure respectively  $\varepsilon_a$  and  $\varepsilon_b$ ) are positioned as shown in Figure 2.12. For this configuration, the angles are  $\theta_a = 30^\circ$ ,  $\theta_b = 90^\circ$  and  $\theta_c = 150^\circ$ . Again, the transformation law (2.12) can be used and solved for the normal strains and the shear strain, with the following results [4]:

$$\varepsilon_x = \frac{2}{3} \left( \varepsilon_a - \frac{1}{2} \varepsilon_b + \varepsilon_c \right) \quad (2.19)$$

$$\varepsilon_y = \varepsilon_b \quad (2.20)$$

$$\gamma_{xy} = \frac{1}{\sqrt{3}} (\varepsilon_a - \varepsilon_c) \quad (2.21)$$

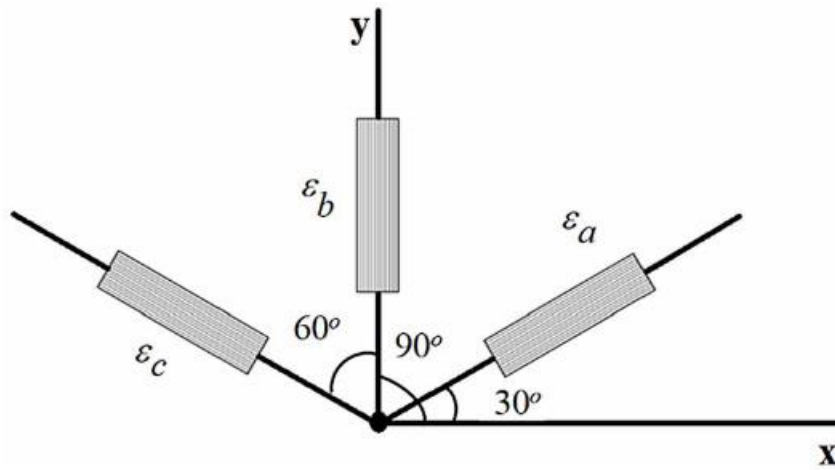


*Figure 2.12* Delta strain gauge rosette [4].

## Chapter 3

# Measuring amplifier and calibration

### 3.1 Measuring amplifier

The voltage signal provided by strain gauges, placed in a bridge configuration, can be processed by measurement amplifier and converted into a corresponding output signal. To acquire our measurements, we used QuantumX MX1615B strain gauge bridge amplifier. This data acquisition module has 16 individually configurable inputs for strain gauges in quarter, half and full bridge circuits, as well as for strain gauge based transducers, potentiometers, resistance thermometers or normalized voltage. The module electronics are integrated in a metal housing that is surrounded by a case protection (Figure 3.1). Typical application areas include static stress tests for FEM models, quasi-dynamic fatigue tests for life analysis, monitoring tasks, material investigations, residual stress analysis, maintenance tasks e.g. for mechanical testing of PCB circuit boards.



*Figure 3.1* QuantumX MX1615B [6].

HBM provides the complete measurement chain for applications in experimental stress analysis, ranging from strain gauges through amplifiers and software. QuantumX is an "open" data acquisition system, and can be integrated into a great many operating, analysis and automation software packages. We used HBM's Catman®Easy data acquisition software (DAQ software) by which we could easily acquire, visualize, and analyze our measuring data. It includes online and offline setup, online visualizations, and online maths as well as recording functionalities. This software enables visualization, analysis and storage of data during measurement and post-report. With Catman®Easy it is possible to choose the type of strain gauge used for the application and to set up specifics such as resistance and gage factor and it displays directly strain read by the strain gauge.

## 3.2 Calibration of the measuring system

In the preliminary phase of the testing, it is necessary to perform the calibration of the measuring system to ensure that the strain gauge is functioning properly and to check the accuracy of the set-up. The aim is to verify the correctness of the measurement system using a simple configuration for which the expected theoretical strain can be calculated and compared with the experimental one obtained. We decided to measure the mechanical strain in a cantilever beam using strain gauges and then compare the results with theoretical strain values calculated from equation derived from solid mechanics.

### 3.2.1 Strain computed with solid mechanics theory

Figure 3.2 shows a simple cantilevered beam subject to a force  $F$  at the end of the beam. In this case, the top of the beam will experience tension and the bottom of the beam will experience compression. In this way, the wires in the strain gauge on top of the beam will be stretched, inducing a positive strain and thus positive  $\Delta R$ . The wires in the strain gauge on the bottom of the beam will be compressed, inducing a negative strain and thus negative  $\Delta R$ .

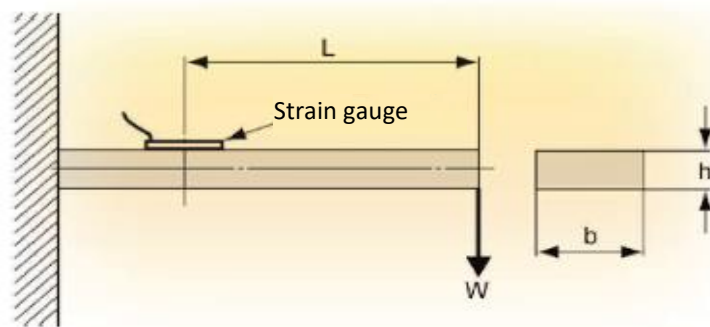


*Figure 3.2* Cantilevered beam subject to force  $F$  at the end [8].

We initially determined the theoretical equation for strain in the cantilever using our knowledge of beams in bending. We start with a quarter bridge configuration: one strain gauge fixed on top of the cantilever. If the beam is subjected to a force  $W$  applied at the extremity, strain gauge is subjected to the following stress:

$$\sigma = \frac{6WL}{bh^2} \quad (3.1)$$

Aware that stress and strain are related with the Hooke's spring law:

$$\sigma = \varepsilon E \quad (3.2)$$

Then we have that the strain is:

$$\varepsilon = \frac{6WL}{Ebh^2} \quad (3.3)$$

In this way, we have produced an equation for the theoretical strain  $\varepsilon$  on the surface of the cantilever at the location of the strain gauge, where  $W$  is the force applied at the end of the beam,  $L$  is the length between strain gauge and the point at which the force is applied,  $b$  is the width of the beam,  $h$  is the thickness of the beam and  $E$  represents the Young's modulus.

### 3.2.2 Experimental setup

We started cutting an aluminium beam with a hacksaw to get the desired length. Using a clamp, we fixed one free end of the beam to a table in our lab. In order to perform the cantilever test, a force was applied by means of positioning a block with known mass being at the free end of the beam. To ensure that force application was as punctiform as possible, the free end of the beam was equipped with a hole through which the threaded end of a thin rod was bolted. A discoidal weight was fixed to the lower end of the bar. The cantilever beam has the following characteristics:

$$h = 3,9 \text{ mm}$$

$$b = 3 \text{ cm}$$

$$L = 6,4 \text{ cm}$$

$$E = 65 \times 10^9 \text{ N/m}^2 \text{ (aluminum)}$$

It is possible to compute analytical strain using formula (3.3) previously discussed, we obtained different values of strain proportional to the weight applied using  $W = \text{weight} \times 9,81 \text{ m/s}^2$ .

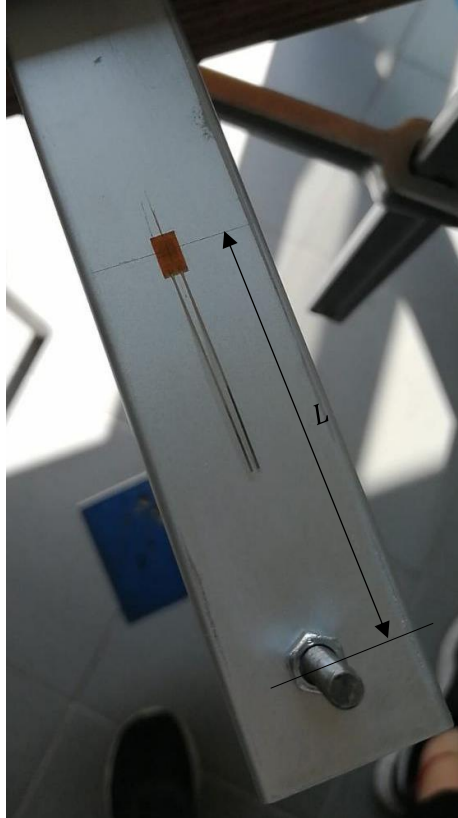


**Figure 3.3** Bonding procedure of the strain gauge.

The procedure for bonding the strain gauges must be carefully performed to avoid measurement errors. For this purpose, we scrupulously sanded the surface of the beam where the strain gauge will be glued, using a fine sandpaper. Then the bonding area was cleaned with solvent to remove debris, dust and grease. Following the cleaning, the linking site must be marked, preferably with a fine graphite pencil so that there is no large graphite deposition in the place, which may end up affecting the measure. We marked the line along the longitudinal length of the beam, where the strain is to be measured and an auxiliary line at 90°, corresponding to the transverse sensitivity axis of the gauge. Then we proceeded with the bonding phase, by handling the strain gauge with the tweezers we placed it carefully, helping us with the marked lines, in the bonding site where we applied first a thin layer of cyanoacrylate glue. We used a piece of transparent tape pressed on the strain gauge to achieve its correct position. Strain gauges should only be handled using the tweezers, avoiding any contact with the hands, reducing any risk of damage in them. Besides, the oiliness that is present in the hand can cause the oxidation of the strain-gauge grid [9]. During the entire procedure, plastic gloves use is recommended. The result of this phase is shown by Figure 3.3. The strain gauge used for this test is a custom product made by Micro-Measurements. Its grid has a linear pattern and an active gage length of 3,56 mm.

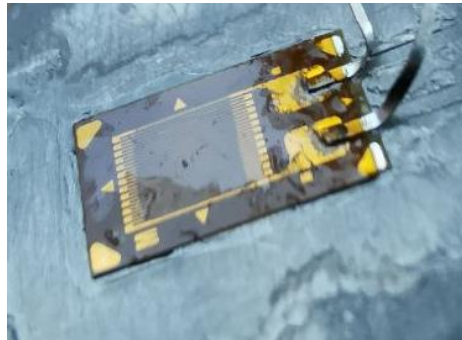


**Figure 3.4** Detail of the strain gauge.

Resistance at 24°C	$350 \Omega \pm 0.3\%$
Gage factor at 24°C	2.08 <i>nom</i>

**Table 3.1** Strain gauge specifics.

Once the strain gauge was glued to the cantilever, we began to solder the electrical wires. This strain gauge is made with preattached, soft and formable copper leads, to which we proceeded to solder a first set of thin and short cables that were soldered in turn to thicker and longer wires connected to the socket/plug with gold pins for sensor connection.

### 3.2.3 Quarter bridge circuit with 4-wires

Regarding quarter bridge configuration for strain gauge, QuantumX supports two, three or four wires circuit for 120 ohms or 350 ohms. In our experimental test we chose quarter bridge 4-wire circuit which is the best choice to reduce measurements errors. This method offers the following advantages compared to the conventional quarter bridge 3-wire method [10].

#### *Leadwire Resistance*

In traditional method, it is recommended to use as thick and short lead wires as possible to maintain the resistance lower. On the other hand, as the 4-wire method is not influenced by the lead wire resistance, it is possible to use thin and long lead wires connected to the strain gauges [10].

#### *Contact resistance*

In traditional method, the extensions of the lead wire and the connections to a measuring instrument are made by soldering or using an exclusive connector. Because the 4-wire method is completely unaffected by contact resistance, a modular plug can be used. Since the modular plug makes lead wire extensions and connections to a measuring instrument possible by simply plugging in, the efficiency of the wiring work and the prevention of wiring errors are achieved [10].

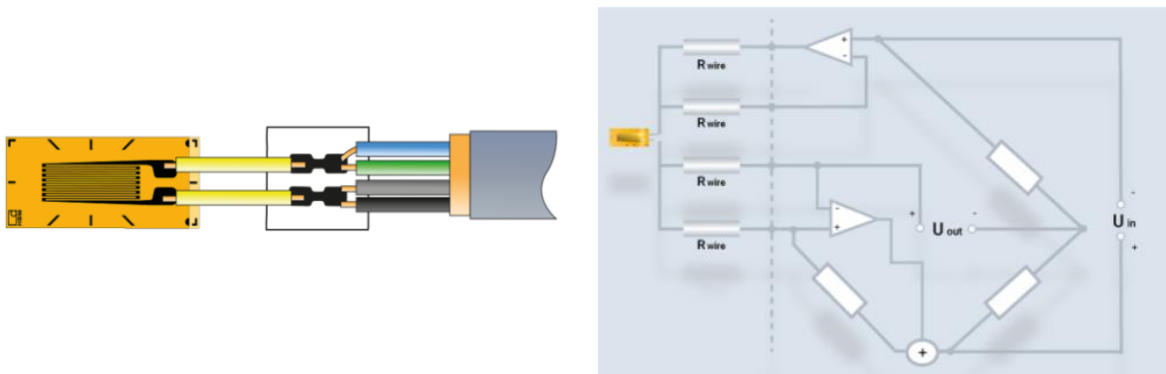


**Figure 3.5** HBM's patented quarter bridge four-wire circuit [11].

According to the QuantumX operating manual, the wiring has been made using push-in connectors 4, 5, 6 and 7 of the wiring mate. Figure 3.6 shows the connection diagram of the circuit in the operating manual and the real wiring. The front panel of the amplifier has a system LED and 16 connection LEDs. The system LED shows the status of the device and the connections LEDs indicates the states of the individual connections. The measurement channels are on electrically isolated from the power supply but not from each other.

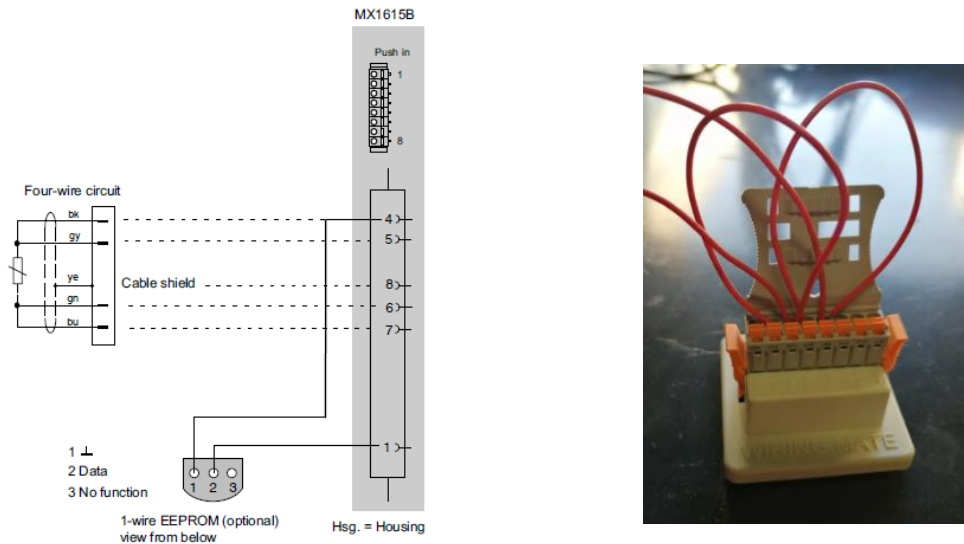


Figure 3.6 Wiring configuration in the operating manual and in reality [12].

After plugging the wiring mate to the QuantumX, checking whether the connection LEDs were green (error-free operation), we connected the amplifier to our laptop via Ethernet. We used Catman®Easy software to communicate with the measuring device. It recognizes not only the configuration of the HBM measuring device connected, but also enables to automatically configure the entire measuring chain. Through the simple user interface, we started a new measurements project and connected the DAQ module. After this step a window displays all the DAQ channels of the module. For DAQ channels with conventional transducers, it is possible to use the integrated Catman sensor database and simply assign the transducers we are using to the individual channels. We then disabled the channels that were not needed. Scrolling through the database we selected “SG 4 wire 350 Ohm” i.e. the type of sensor we wanted to assign to the port. The next step consists in configuring the specifics of the strain gauge, in particular the gage factor, set to 2.08, and the excitation voltage, set to 5 V.

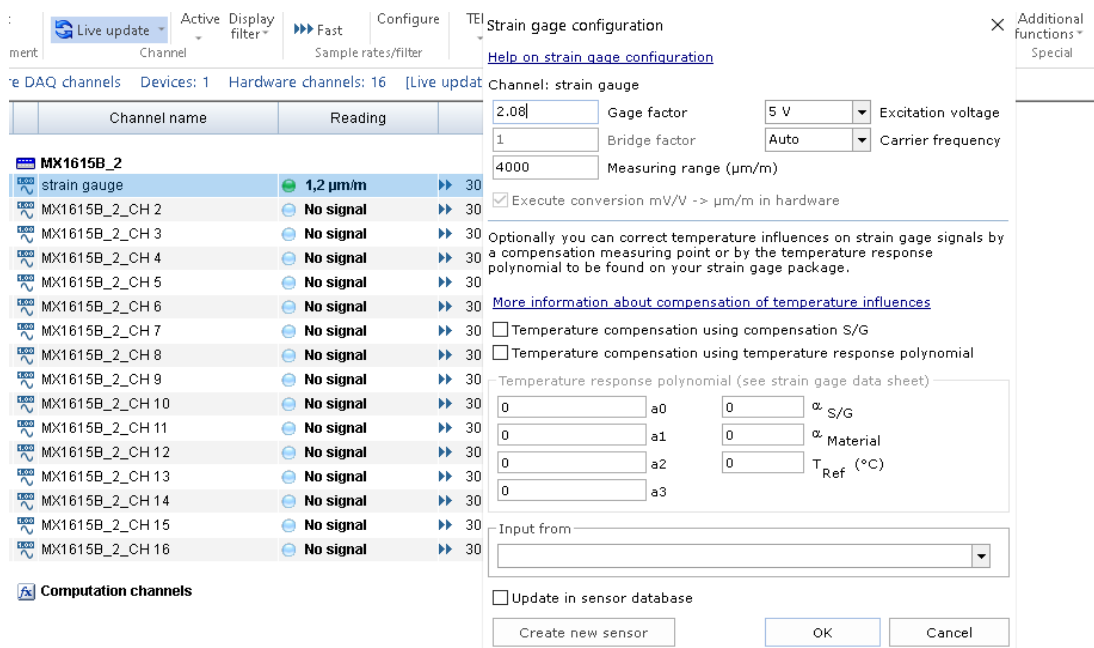


Figure 3.7 Setting specifics of the strain gauge.

The sensor must be configured with the correct range, however, otherwise an error message will indicate that there is no suitable band on the connector for the strain gauge. Once this procedure is completed, it is possible to carry out the zero balancing (“Zero Balance”) with the channel, in order to assign the zero point to the initial configuration of the strain gauge, i.e. the output signal of the sensor under no load. If the zero value of the sensor has changed substantially compared to the zero value on shipping (by about 1 to 5%, depending on the quality of the transducer), there is most likely mechanical damage, meaning the sensor is defective. The value has no practical significance beyond this, because after installation of the transducer there is usually a completely different zero value [13]. That value is eliminated by zero balancing the channel. Now it is possible to start experimental measurements.

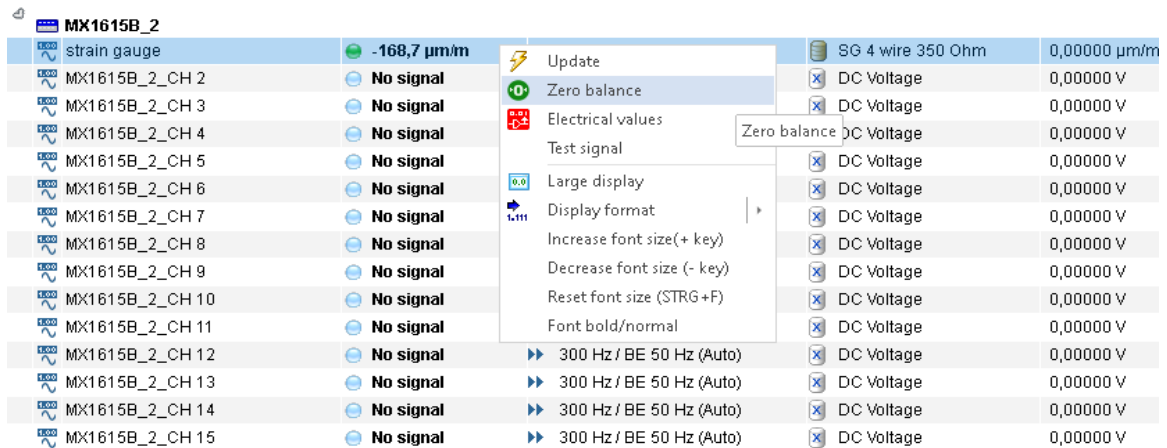


Figure 3.8 Zero balancing.

Catman Easy displays the measured strain in  $\mu\text{m}/\text{m}$ , which means  $10^{-6} \text{ m}/\text{m}$ , that can be directly compared with the strain obtained with theoretical computation.

Data analysis

Figure 3.9 illustrates, by way of example, the software window of the first measurement performed with a disc sample mass of 1,0009 kg.

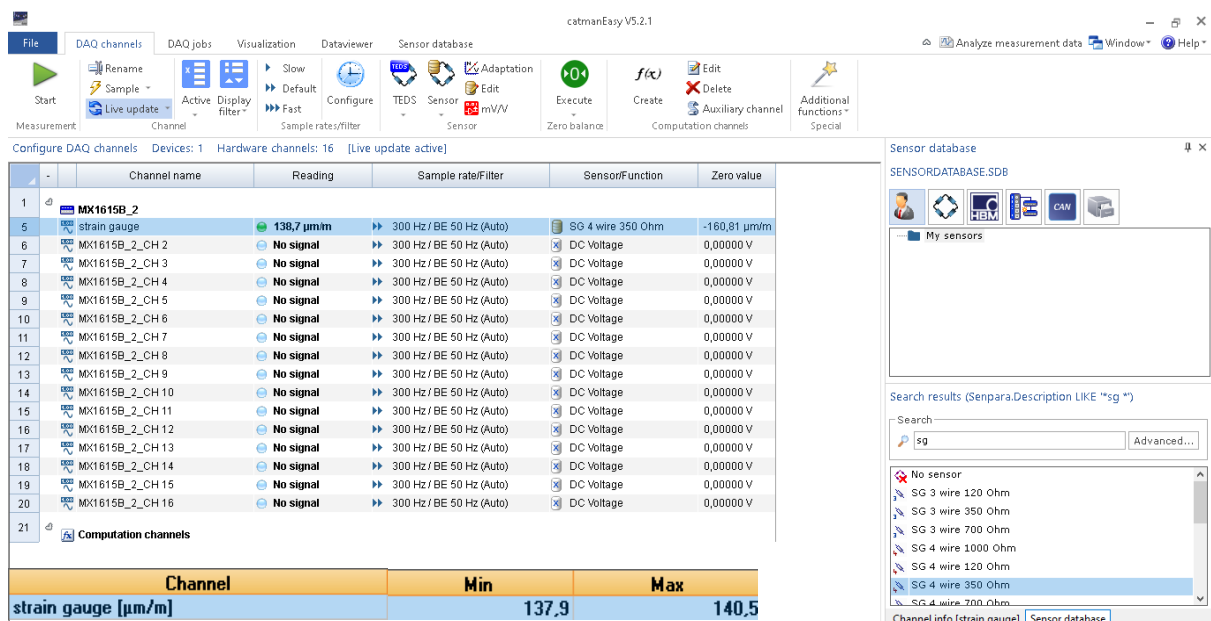


Figure 3.9 Example of Catman output with quarter bridge circuit.

Experimental strain measures reported in Table 3.2 were obtained computing the average between the minimum and maximum values displayed during the acquisition. Table 3.2 shows the comparison between experimental and theoretical strain. The latter was computed with equation 3.3 according to the force applied to the cantilever beam. In the theoretical calculation we considered the additional weight of the mass holder rod, equal to 0,1 kg.

Weight applied M	Theoretical strain $\epsilon$	Experimental strain $\epsilon$
1,0009 kg	139,8 $\mu\text{m/m}$	139,1 $\mu\text{m/m}$
1,0101 kg	140,9 $\mu\text{m/m}$	139,8 $\mu\text{m/m}$
2,0000 kg	266,7 $\mu\text{m/m}$	271,9 $\mu\text{m/m}$
2,0110 kg	268,1 $\mu\text{m/m}$	274,3 $\mu\text{m/m}$
3,0009 kg	393,8 $\mu\text{m/m}$	407,2 $\mu\text{m/m}$

**Table 3.2** Comparison between theoretical and experimental strain results in quarter bridge circuit.

The following graph realized with Excel demonstrates that results obtained experimentally are very similar to the theoretical ones. We can conclude that measuring system has been set up in proper manner and everything works correctly.

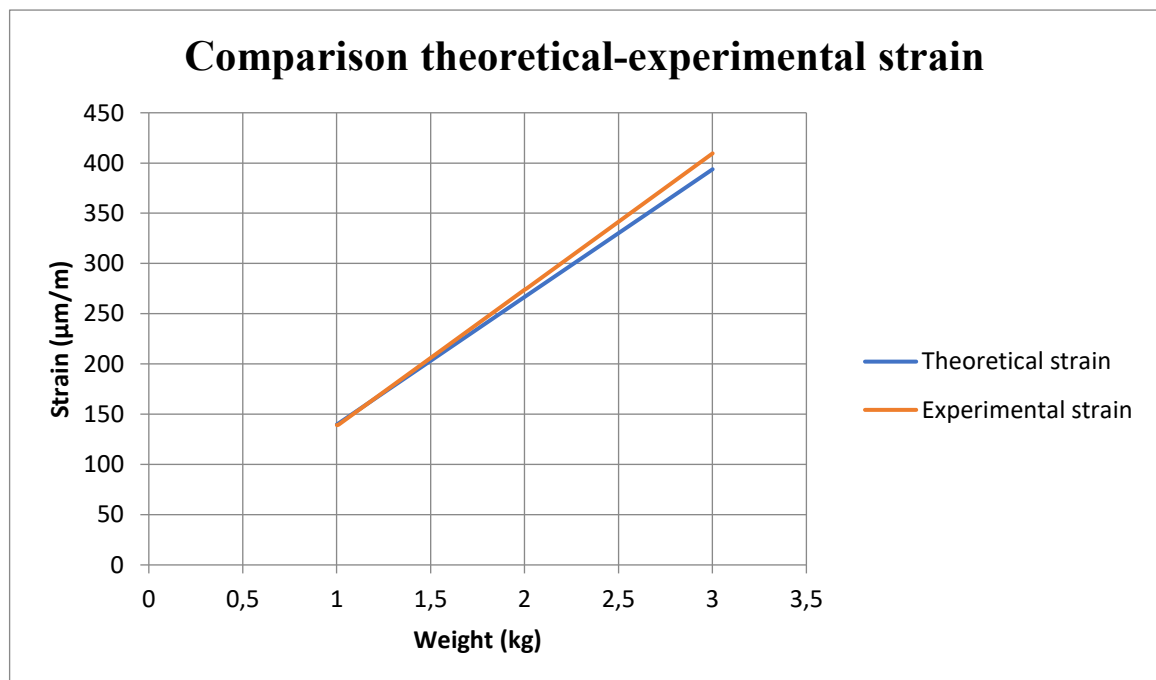


**Figure 3.10** Theoretical and experimental strain behavior.

### 3.2.4 Half bridge configuration

Half bridge configuration has some advantages as compared with the quarter bridge configuration. A half bridge has an increased sensitivity and an automatic temperature adjustment. As the half-bridge contains one more active gauge than the quarter-bridge, the half-bridge is capable of detecting smaller strains with greater accuracy [14]. For the half bridge configuration, we installed two strain gauges symmetrically on the upper and lower surfaces of the cantilever beam, as shown in Figure 3.11. They produce signals of identical absolute value but of opposite sign.

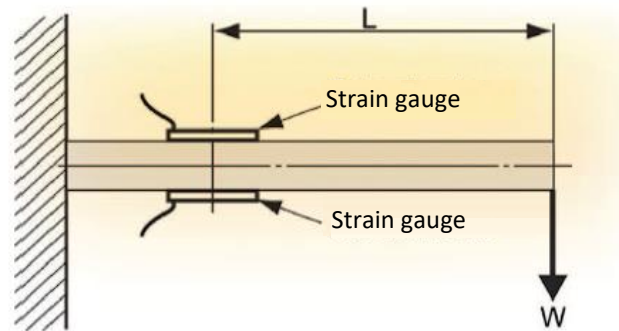


*Figure 3.11* Theoretical and experimental strain behaviour [8].

The possibility of temperature compensation is due to the fact that individual branches flow with different signs in the Wheatstone bridge circuit. With reference to the previous figure, under load the spring exhibits positive strain on the top of the cantilever and compression on the bottom. If two strain gauges are connected to a Wheatstone bridge circuit, the result is to double the signal. If temperature-dependent strain arises, the strain appears to both gauges with the same sign. Therefore, the effects cancel each other out in the bridge circuit [15]. The half bridge configuration has been realized installing a second strain gauge on the bottom surface of the cantilever beam at the same distance  $L$  from the end of the beam (Figure 3.12).

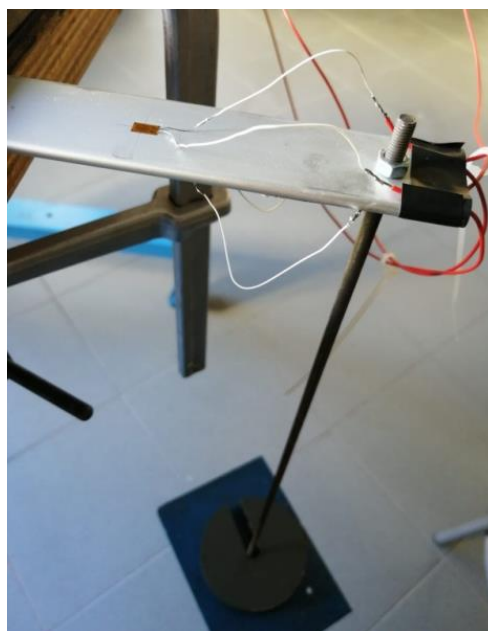


*Figure 3.11* Cantilever beam in half bridge configuration.

The wiring of the half bridge configuration was performed following the instruction in QuantumX operating manual.

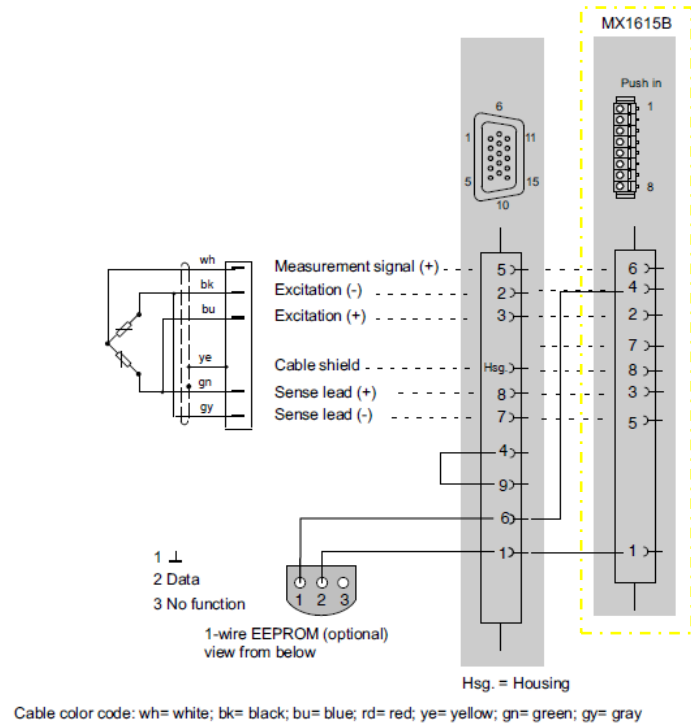


**Figure 3.12** Half bridge wiring configuration in the operating manual.

In practical terms, the cabling was carried out as follows:

- strain gauge on top surface: one wire was inserted into port 6 and another wire into port 4
- strain gauge on bottom surface: one wire inserted into port 6 and another wire into port 3
- additional wiring: port 4 bridged with port 5 and port 2 bridged with port 3

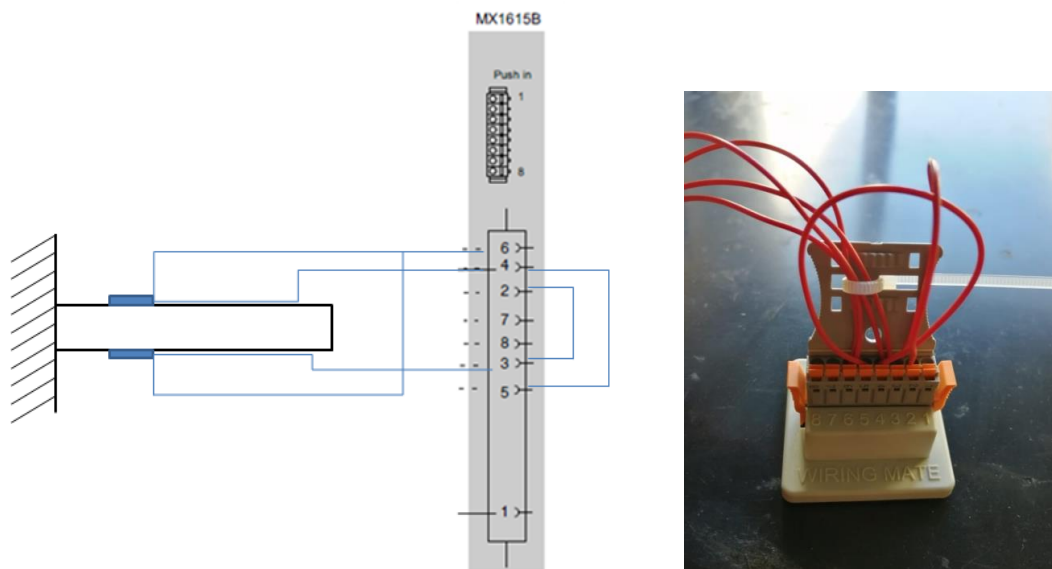


**Figure 3.13** Wiring for half bridge configuration.

## Measuring amplifier and calibration

After cabling, it is possible to start a new data acquisition using Catman software and by selecting "SG half bridge 350 Ohm" as the sensor type and inserting the gauge factor. Figure below shows the Catman window for the first measurement with a mass of 1,0009 kg.

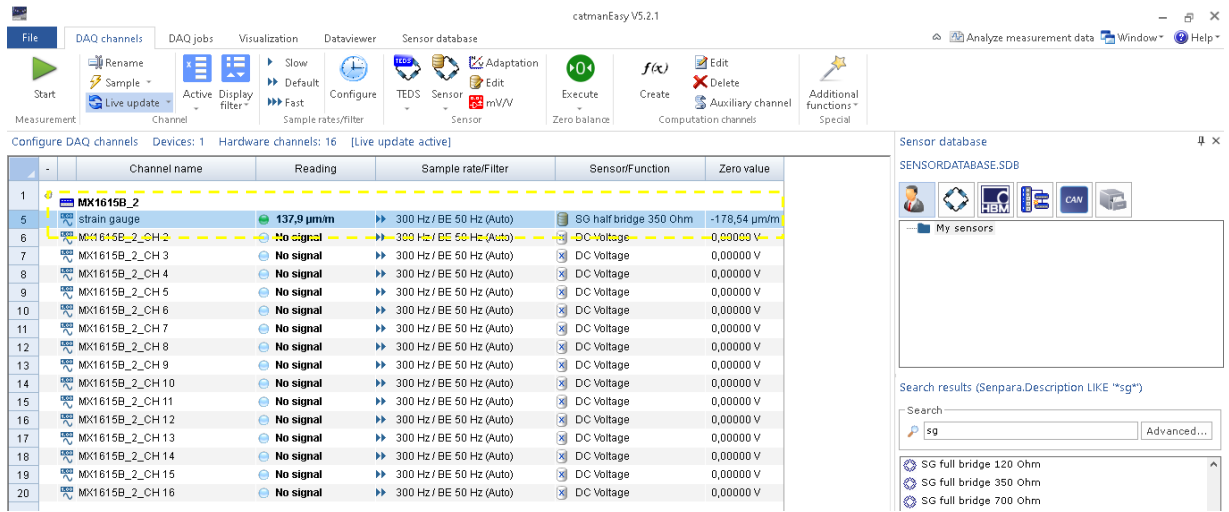


Figure 3.14 Catman output for half bridge configuration.

Experimental strain measures reported in Table 3.3 were obtained computing the average between the minimum and maximum values displayed at the end of the acquisition. Table 3.3 shows the comparison between experimental and theoretical strain.

Weight applied M	Theoretical strain $\epsilon$	Experimental strain $\epsilon$
1,0009 kg	139,8 µm/m	139,0 µm/m
1,0101 kg	140,9 µm/m	139,7 µm/m
2,0000 kg	266,7 µm/m	274,1 µm/m
2,0110 kg	268,1 µm/m	279,2 µm/m
3,0009 kg	393,8 µm/m	414,6 µm/m

Table 3.3 Comparison between theoretical and experimental strain results in half bridge circuit.

The following chart realized with Excel shows that results obtained by experimentation are very similar to the theoretical results. It can be concluded that the measuring system has been set up correctly and everything works properly.

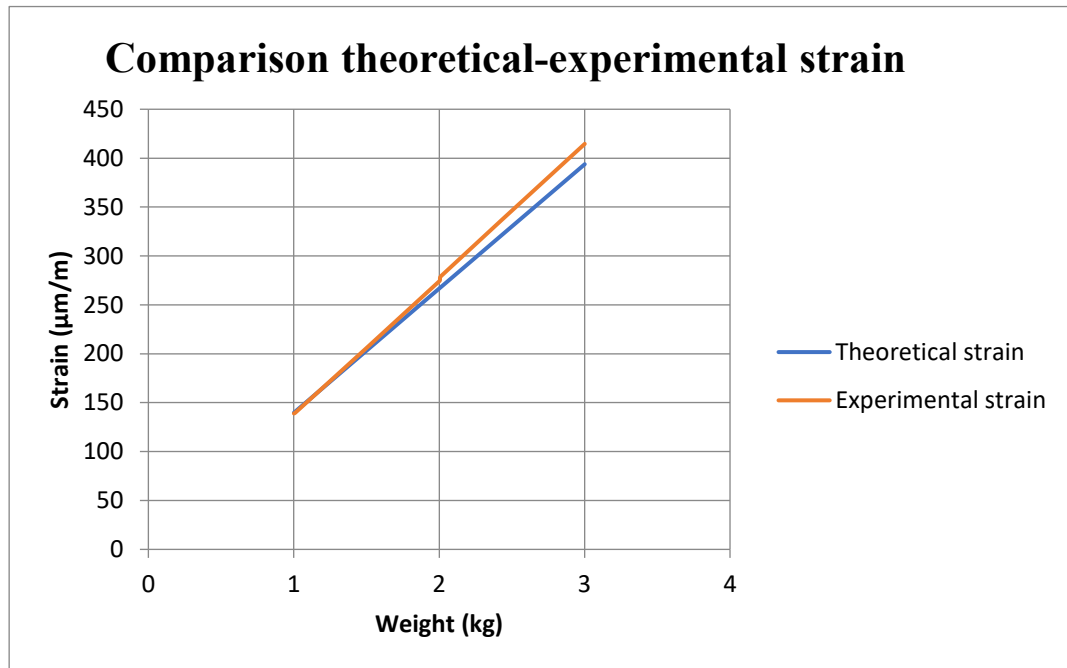


Figure 3.15 Theoretical and experimental strain behavior.

### 3.2.5 Full bridge configuration

Full bridge or half bridge configuration should be used in stress analysis if different kind of interferences need to be eliminated. In a full bridge circuit, we have active strain gauges in all four bridge arms. In both half-bridge and full-bridge circuits, temperature effects are well compensated. In full bridge configuration, there are two strain gauges mounted on top of the beam and two strain gauges mounted on the bottom, at the same distance  $L$  from the end of the beam. In comparison to the half bridge, the full bridge has higher efficiency and sensitivity considering the presence of two additional strain gauges.

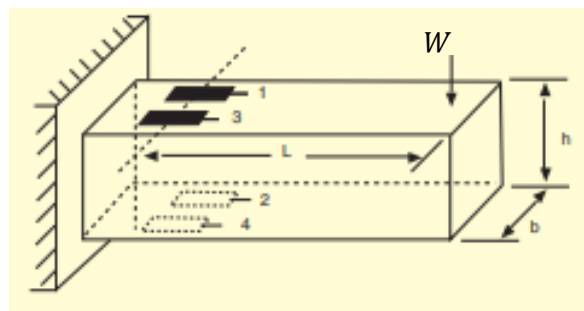
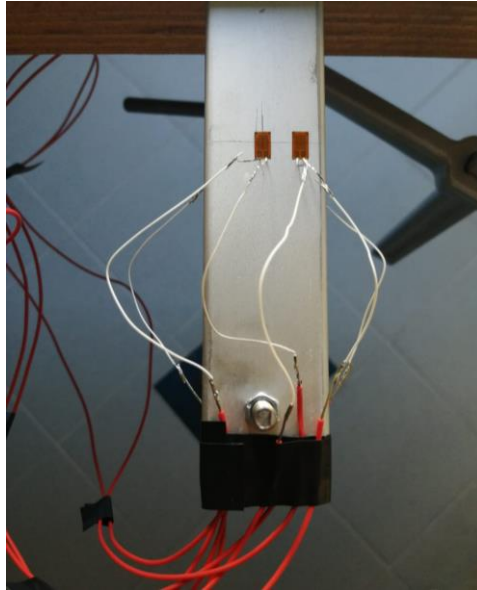


Figure 3.16 Full bridge configuration on a cantilever beam.



**Figure 3.17** Cantilever beam in full bridge configuration.

To prevent the weight of the wiring from stressing the strain gauges, we attached the cables with adhesive tape to the end of beam.

The wiring of the half bridge configuration was performed following the instruction in QuantumX operating manual.

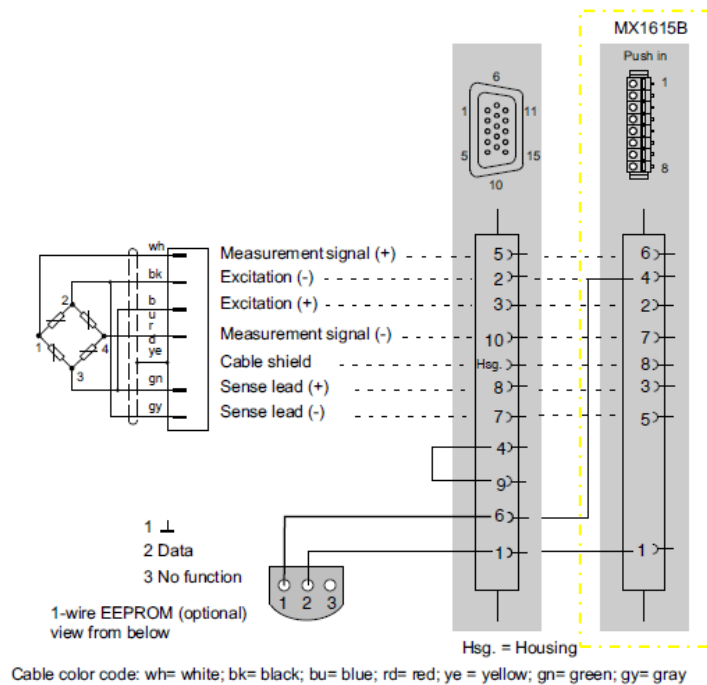


**Figure 3.17** Full bridge wiring configuration in the operating manual.

In practice wiring has been realized in the following way:

- strain gauge 1 on top surface: a wire has been inserted in port 6 and another wire in port 4
- strain gauge 3 on top surface: wires inserted in port 7 and 3
- strain gauge 2 on bottom surface: wires inserted in port 4 and 7
- strain gauge 4 on bottom surface: wires inserted in port 6 and 3
- additional wiring: port 4 bridged with port 5 and port 2 bridged with port 3

In order to check that electrical wire welding was realized properly, we measured the voltage between each couple of strain gauge cables reading the same value of 0.4 V using a voltmeter. In Figure below is shown the wiring scheme and its realization in practice.

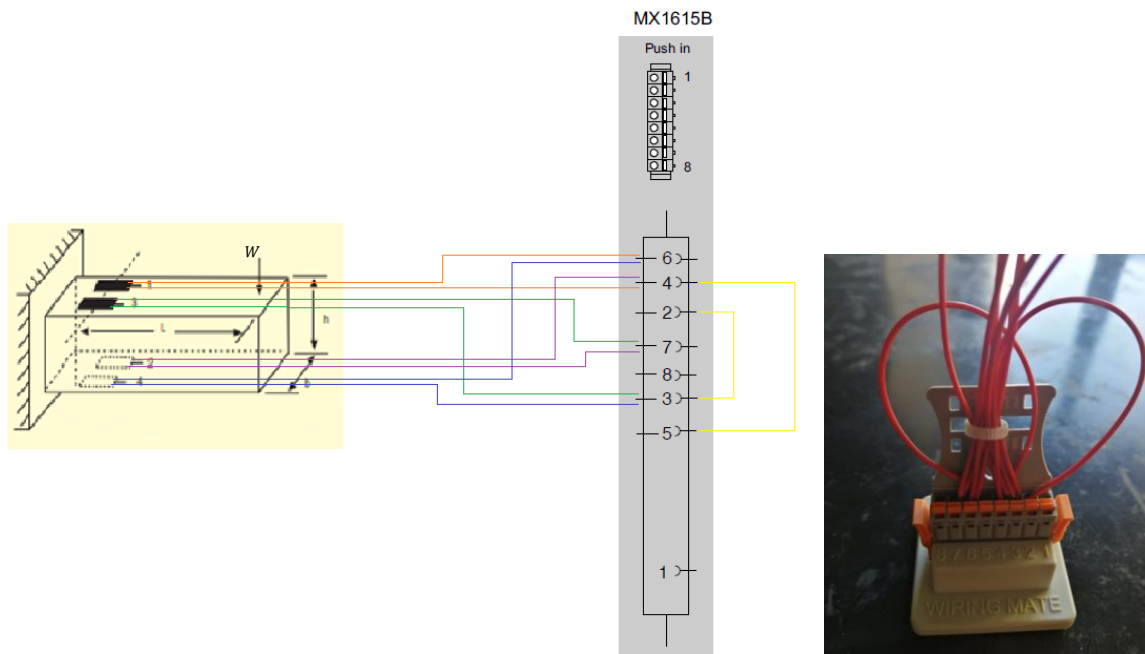


Figure 3.18 Wiring for full bridge configuration.

After cabling, it is possible to start a new data acquisition using Catman software and by selecting "SG full bridge 350 Ohm" as the sensor type and inserting the gauge factor. Figure below shows the software window for the first measurement with a mass of 1,0009 kg.

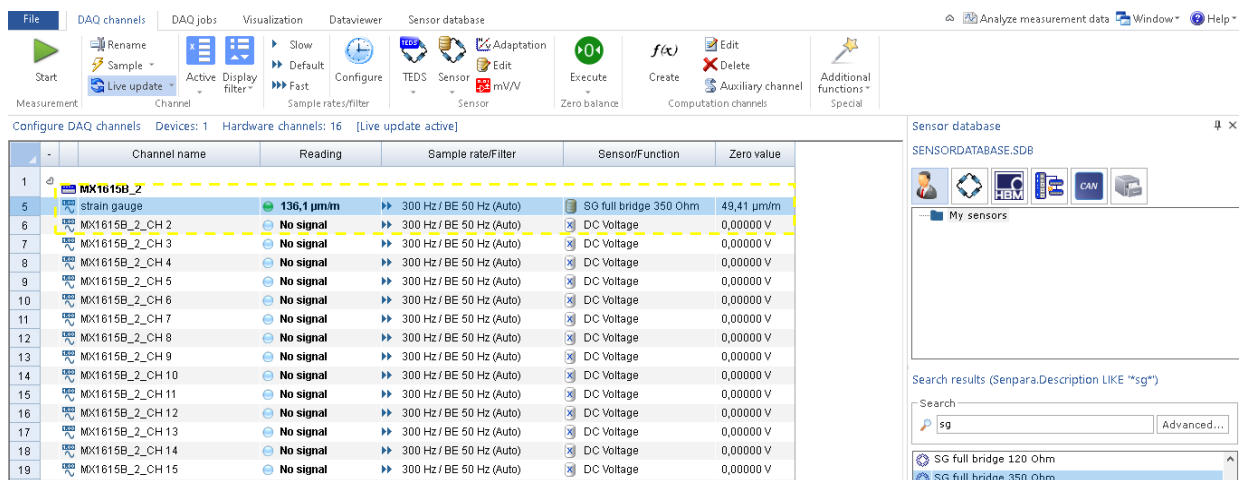


Figure 3.19 Catman output for full bridge configuration.

Strain measurements with different weights have been realized and the results obtained are summarized in Table 3.4 below.

Weight applied M	Theoretical strain $\epsilon$	Experimental strain $\epsilon$
1,0009 kg	139,8 $\mu\text{m/m}$	136,3 $\mu\text{m/m}$
1,0101 kg	140,9 $\mu\text{m/m}$	138,5 $\mu\text{m/m}$
2,0000 kg	266,7 $\mu\text{m/m}$	271,2 $\mu\text{m/m}$
2,0110 kg	268,1 $\mu\text{m/m}$	273,4 $\mu\text{m/m}$
3,0009 kg	393,8 $\mu\text{m/m}$	403,15 $\mu\text{m/m}$

**Table 3.4** Comparison between theoretical and experimental strain results in full bridge circuit.

The following graph realized with Excel demonstrates that results obtained experimentally are very similar to the theoretical ones. We can conclude that measuring system has been set up in proper manner and everything works correctly.

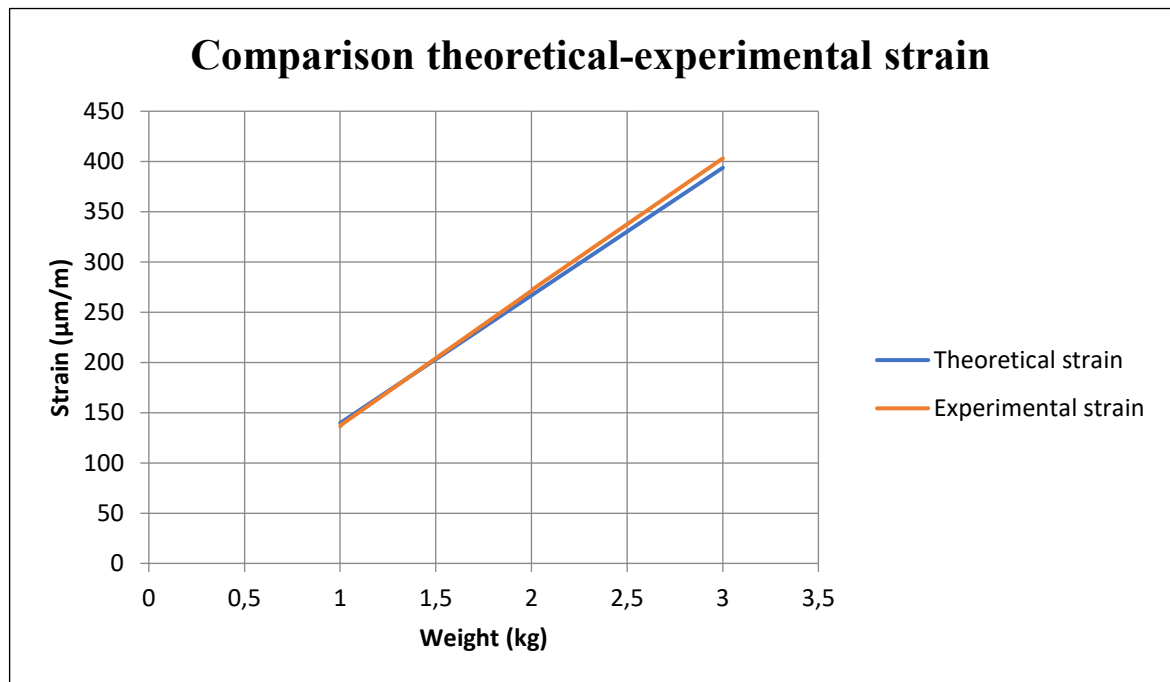


**Figure 3.20** Theoretical and experimental strain behavior.

## Chapter 4

# Test Bench

In this phase of the project, we performed the design and fabrication of the test bench. Its purpose is to impose a pressure inside the device and realize a system able to adjust the pressure value in a simple and effective way. After realization of the test bench, it is possible to test the samples and the sensor system and validate the method of measure.

### 4.1 Structure and characteristics of the test bench

After configuring the strain gauge amplifier, it was necessary to set up a test bench to be able to pressurize our prototypes with embedded strain sensors. Achieving a wide range of constant pressures inside our reservoirs is not an easy task. The first step was to figure out which fluid could be used for our purpose. Compressed air utilization would have allowed us to use a simple compressor to increase the pressure of the gas. However, the vibration of the compressor motor could have caused the capsule to move and affect the measurement. Hence, we decided to use hydraulic pressure. A double-acting pneumatic cylinder was selected as our hydraulic actuator to generate pressure in a circuit of plastic tubes filled with water. Since water is nearly impossible to compress, a hydraulic actuator can apply a larger force than a pneumatic one. Not having available low-pressure water cylinder in our lab, we used a pneumatic cylinder for this application. The double-acting air cylinder under consideration, manufactured by SMC Corporation, has a bore size of 32 mm and a stroke of 80 mm (Figure 4.1).



*Figure 4.1* SMC double-acting pneumatic cylinder.

The piston has air cushioned noses at both ends and four tie rods to protect the barrel. To verify its functioning with water, we connected the posterior chamber port (right port in Figure 4.1) to a single PFA pipe, then we drew water into the chamber by pulling out the piston rod (extension stroke of the linear actuator). After attaching a barometer, already filled of water, to the other pipe end, we increased

the pressure in the circuit by pushing the piston rod (retraction stroke of the actuator, rightward in Figure 4.1). Push-in fittings were attached to the piston chamber port and the barometer port to facilitate circuit assembly operations. For each fitting we wrapped polytetrafluoroethylene (PTFE) film tape around the ends of the tubes for sealing. In this way, we could reach pressure up to 10 bar without water leakage.

Once verified that it was possible to use the pneumatic cylinder at our disposal to perform tests with pressurized water, we proceeded further with the construction of our test bench. To have a stable support surface to work on, and easily move the piston rod, we fixed the pneumatic actuator to a wooden board with cable ties. We secured with screws two angle brackets to the board, one (top in Figure 4.2) is used to constraint the rear end cap of the cylinder during the retraction stroke, the other (below in Figure 4.2) provides a rigid support through which the piston rod can be pushed.

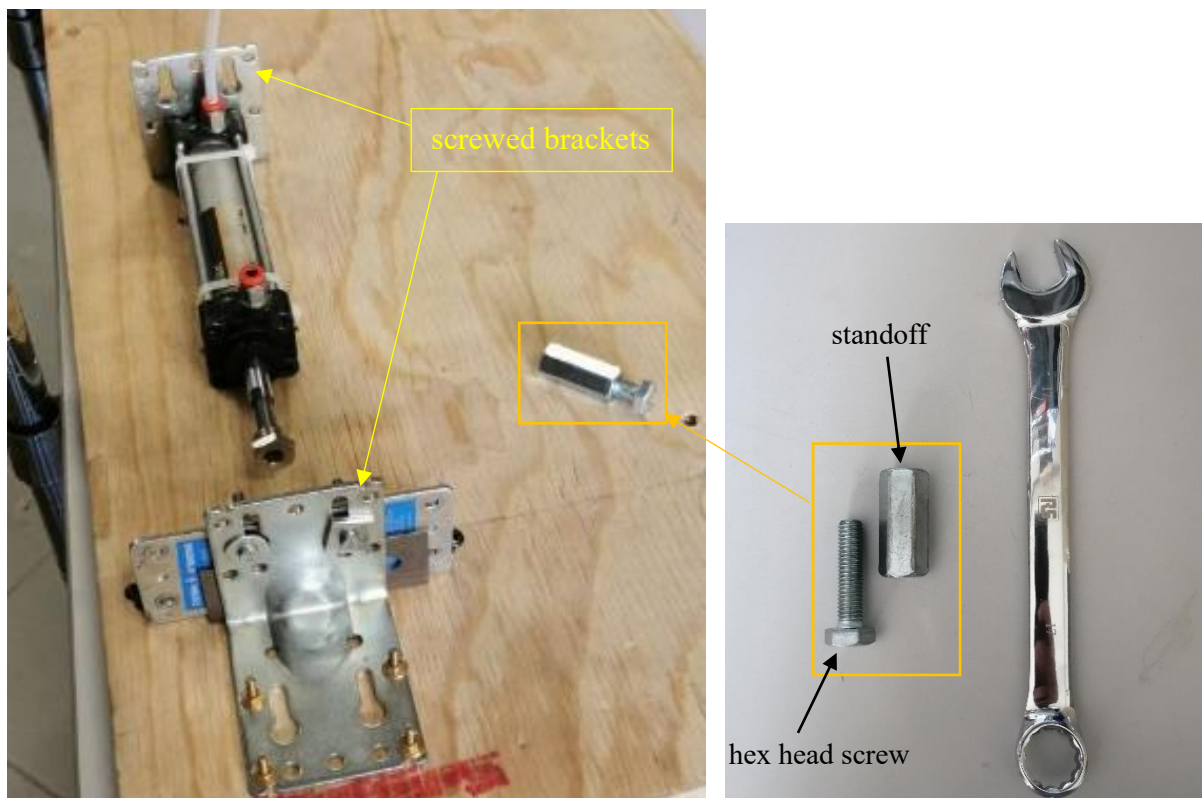


**Figure 4.2** Close-up view of the test bench and work tools.

By using a hex head screw, a hex standoff with female threads and a wrench, we made the kinematics to move the piston rod and set the pressure. A standoff is used to separate one part to another in an assembly. The hex head of the screw must rest on the bracket and press against it by means of the standoff which is unscrewed on it. Using some metal plates, fixed to the bracket, we created a seat for the hexagonal head of the screw, avoiding its rotation during the unscrewing of the standoff. The external hex of the standoff lets us tighten or loosen with a wrench. In the threaded end of the piston rod, we screwed a nut to create a larger surface on which the standoff can press against. Since water is relatively incompressible, a few turns of the hex standoff, meaning a short retraction stroke of the piston, will be enough to reach high pressures.

We then created a circuit of flexible PFA pipes using push-in fittings with M5 threaded connections. One fitting is installed in the rear end cap port of the cylinder. A ‘tee’ type fitting creates a secondary branch, approximately in the middle of the main pipe, where we linked a barometer, suitable for water, which indicates the inner pressure. The capsule sample is connected to the circuit by means of a hand-made fitting (Figure 4.3). For its making, we sawed off few centimeters of an aluminum rod which we then drilled with a through hole that was tapped at both ends. At one end we tightened a push-in fitting, to be connected to the main tube of the circuit, on the other we screwed in a threaded pin which was first perforated, to allow water to flow inside the capsule.



*Figure 4.3* Hand-made fitting connection.

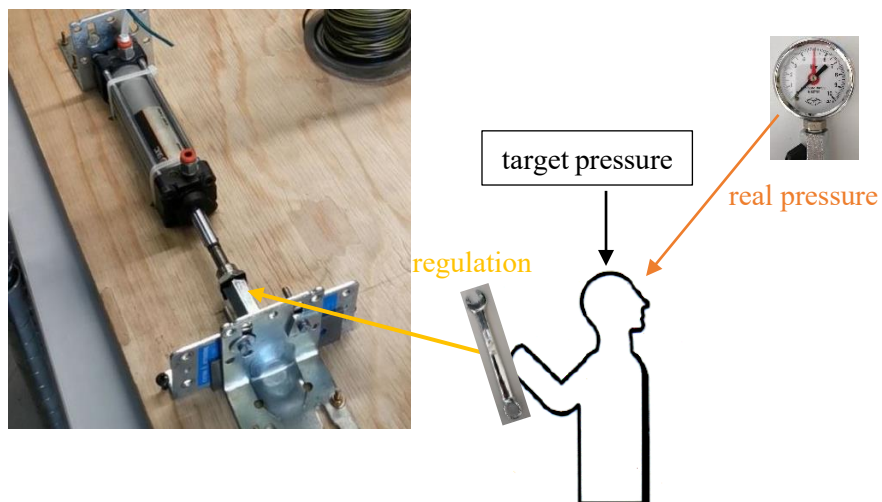


*Figure 4.4* Closed loop of adjustment.

In the previous page, Figure 4.4 illustrates the scheme of the circuit adjustment. Adjustment is a process during which the quantity to be controlled is constantly detected, compared with another quantity, the reference one, and, based on the result of this comparison, modified until it reaches the value of the reference quantity. The resulting actions are carried out in a closed loop called an adjustment loop. When there is a difference between the actual value and the target value, a corrective adjustment becomes essential.

In our tests the activities of measurement, comparison and compensation are done by a person, so it is a manual adjustment. During adjustment it's necessary to carefully observe the pointer of the barometer. For convenience and to keep in full sight the pressure gauge, we hang it at eye level.



*Figure 4.5* Close-up view of the barometer, PTFE tape and push-in fittings.

Table 4.1 below shows the list of all the components used for the fabrication of the test bench.

Test bench component	Quantity
Wooden board	1
SMC double-acting pneumatic cylinder	1
Angle brackets	2
Cable tie	2
Hexagonal head screw	1
Hexagonal standoff	1
Wrench	1
Pressure gauge with range 0-10 bar	1
Push-in fitting	5
Hand-made fitting	1
PFA pipes	3
Screws and nuts	8
PTFE seal tape	

*Table 4.1* Test bench components list.

## Chapter 5

# Samples and sealing tests

This chapter will introduce the various types of samples at our disposal and the pressure tests performed on the test bench to verify their sealing. We recall that, in the water circuit, the sealing is guaranteed by wrapping PTFE seal tape at the ends of PFA pipes where the tube needs to be inserted in the push-in fitting. However, it was relatively simple to make the push-in fittings perfectly watertight, even for hydraulic pressures above 10 bar. On the other hand, many sealing problems were encountered concerning the hand-made fittings and the samples examined. Ensuring no water leaks were present, was a difficult and time-consuming job. Through a trial-and-error process, it was possible to ensure total sealing for some of our samples.

### 5.1 Samples

The goal of the experimental activity is to test the sensor system and validate the method of measure. After construction of the test bench, samples are required to conduct the tests. Some of these capsule samples were designed by us via 3D CAD software and made by an external company through additive manufacturing. Other samples were selected by Dr. Alessandro Grattoni and Dr. Nicola Di Trani of the Houston Methodist Research Institute and sent to our laboratory at Politecnico di Torino. In the following paragraphs we review the various types of samples that we had available and their sealing tests.

#### 5.1.1 Disc-shaped capsules produced with additive manufacturing

After performing FEM simulations and analysis of different design solutions, it was decided that the capsule should have the shape of a disc. As already explained in paragraph 1.3, the two flat faces of the disc represent very suitable surfaces for fixing strain gauges, and, if they have sufficiently thin walls, they can deform elastically and provide an accurate indication of the internal pressure. Indeed, a thin surface deforms more than a thicker and provides higher sensing sensitivity. The disc-shaped capsule is designed by dividing it into an upper and lower part, which form two symmetric membranes coupled. As can be seen on the right of Figure 5.1, the lower element has small grooves along the edges that mate the corresponding projections along the edges of the upper part (Figure 5.1 on the left). A cubic nub protruding from the thickness of the capsule is added. This element provides the connection between the capsule and the PFA pipes circuit through the hand-made fitting. The nub must be drilled and tapped, then it is possible to screw in the perforated threaded pin that connects the hand-made fitting to the sample. At the top and bottom of the sample, the circular surfaces that form the two symmetric membranes measure 22 mm in diameter. For these membranes, the maximum strain value is located at the center, as analyzed in the FEM simulations of paragraph 1.3.2. The top and bottom part of the disc-shaped sample must be meticulously glued together with a powerful adhesive to ensure a good sealing and avoid water leaks. The glue deposited in the grooves will ensure greater bonding.

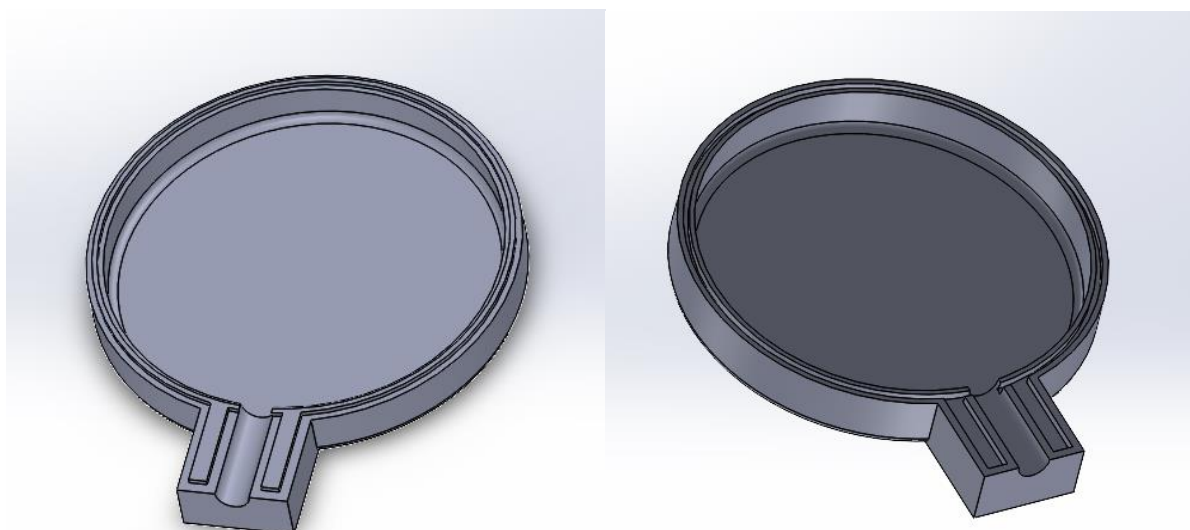


**Figure 5.1** Upper (left side) and lower (right side) part of the capsule.

The CAD file of the sample was sent to a company specialized in 3D printing. In about a week, we received two 3D printed capsules in polyamide 12 (PA12 or nylon 12) made by Multi Jet Fusion (MJF) process, and two metallic capsules, one made in aluminum alloy (AlSi10Mg) and the other made in titanium alloy (Ti6Al4V), printed using Stereolithography (SLA) process. The samples are showed in Figure 5.2 below.



**Figure 5.2** 3D printed samples: A) Ti6Al4V; B) AlSi10Mg; C) PA 12.

The building machines, used for making our samples, are from SLM Solutions and Multi Jet Fusion HP. As can be observed from the previous figure, the titanium alloy sample has a higher dimensional accuracy than the other capsules. The titanium parts perfectly mate together and once the assembly has been composed, considerable force must be exerted to separate the parts. A caliper was used to measure the main dimensions of the sample and verify the conformity to dimensional tolerances. The AlSi10Mg sample presents a lower functional finishing degree but after wiping with sanding paper on the mating surfaces, the capsule can be assembled. As regards the sample printed in PA 12, the dimensional tolerances of the grooves and projections along the edges are not respected at all. This makes it very difficult to couple the surfaces of the PA 12 capsule and, therefore, its sealing.

### Sealing problems and solutions

The sealing test starts with the gluing of the sample. First the two parts that compose the capsule are glued together, then a bit of glue is also applied on the connection between the hand-made fitting and the sample. Depending on the material of which the capsule was made of, we used different types of adhesives for sealing. For the metal capsules we used an epoxy bicomponent adhesive suitable for bonding metallic parts. For the PA 12 sample we initially applied a bicomponent adhesive made of epoxy resins, then we tried a cyanoacrylate glue proper for hard plastic. After waiting for the time necessary for the glue to dry, the next phase consists in connecting the capsule with the water circuit of the test bench, via the push-in fitting. Then, the pressure can be gradually raised, checking that no water leakage occurs. First attempts to pressurize were made on the capsule made of PA 12, however, the sample had out of tolerance dimensions. The small details such as the grooves were barely hinted at and therefore it was not possible to obtain a good sealing. After reaching pressures around 2 *bars* the water was already beginning to leak from the sides of the sample. Printed sample made of aluminum alloy has a high dimensional tolerance, though it was necessary wipe with the sandpaper in the grooves for a perfect mate between the parts. In this case, once a pressure of about 3.5 bar was reached, the specimen began to lose water from the grip points. Besides, the epoxy adhesive used becomes very rigid once dried and may be subject to brittle fractures because of the pressure forces within the capsule. In order to overcome such leakage problems, we developed a new 3D CAD model with additional enhancements. The failure of the pressure tests was largely due to the small area on which the adhesive could bond. Moreover, to reach high pressures it was necessary to counteract the pressure forces that tended to divide the capsule as the bonding forces of the adhesives were not sufficient. On the next page, Figure 5.3 shows the redesigned 3D CAD model. As a first correction, we modified the dimensions of the grooves, making them wider and deeper to increase the gripping surface. Furthermore, one peripheral collar is added around the edges of the capsule: once glued to the sample, this collar operates to mechanically join the two parts. Ridges along the edges form the surface on which the collars mates. We requested from the same 3d printing company the production of some redesigned samples, this time made only of Ti6Al4V and PA 12. With the new capsule samples, it was possible to reach pressure of 8 *bar* for the titanium capsule and 4 *bar* for the PA 12 capsule, without water leakage.



*Figure 5.3* Redesigned 3D CAD model for 3d printed samples.

### 5.1.2 Samples from the Houston Methodist Research Institute

Two different types of samples were sent via postal service from the Houston Methodist Research Institute. These capsules were previously used by Dr Grattoni's team to conduct in vivo tests with the use of nanofluidic membranes. As can be seen in the following figures, the samples have a variety of holes that connect the inside of the reservoir to the external environment. These through holes allowed for controlled drug release from the nanofluidic membrane, which was positioned in its seat obtained on the internal surface of the reservoir. Therefore, to pressurize the sample, the holes must be carefully sealed up. Figure 5.4 shows the detailed pictures of the first capsule type sent to our laboratory. It is a disc-shaped metallic capsule, made of titanium alloy (Ti6Al4V) and CNC machined. The sample consists of two parts screwed together through a thread. Not having available a CAD model or an engineering drawing of the parts, we measured the dimensions with a caliper. Once assembled, the sample has a total height of 5,1 mm and its external diameter measures 16,6 mm. or this. The surfaces have a high finishing degree and provide a perfect tightening of the two parts.



**Figure 5.4** Machined titanium alloy capsule sent by the Houston Methodist Research Institute.

The second type of sample sent from Houston is a disc-shaped capsule molded in Polyamide (PA) (Figure 5.5). Also here, on a side of the sample, there are numerous through holes for the in vivo tests with the nanofluidic membrane. The holes were then sealed up with epoxy or silicone glue in order to allow the pressurization of the capsule.

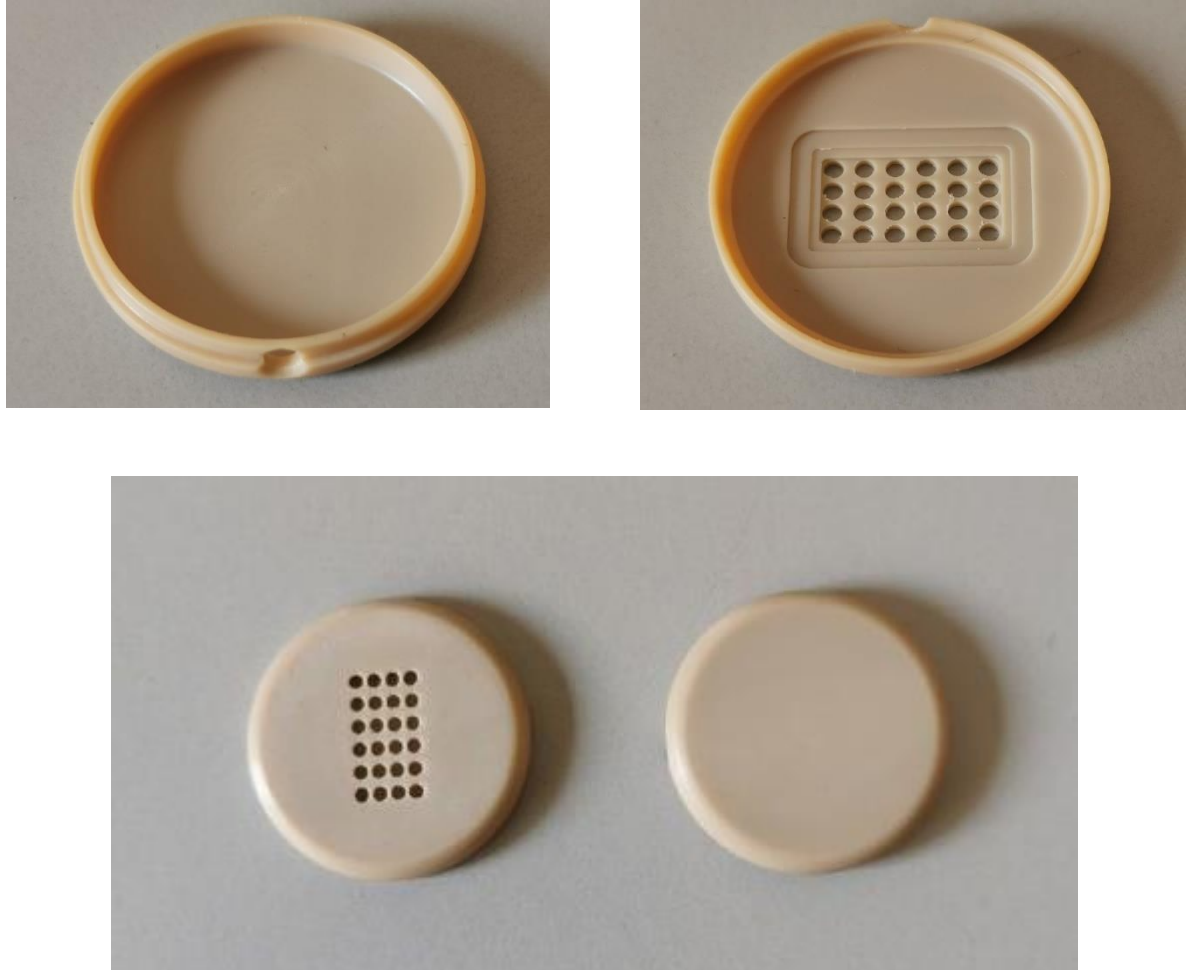


*Figure 5.4* PA molded capsule sent by the Houston Methodist Research Institute.

### Sealing problems and solutions

It must be recalled that one of the most critical part of the realization of the set up to perform testing is the achievement of a perfect sealing that allows to pressurize the device. It was necessary to study and develop specific solutions for the different types of capsules. For the machined titanium alloy sample of Figure 5.3, the joining of the upper and lower parts is done by first applying the epoxy two-component adhesive and then screwing them together. Furthermore, the holes on the capsule must be sealed up. For this purpose, we have applied a thin sheet of rigid plastic on the internal surface of the capsule, suitably shaped and glued to further seal the holes. The most complicated part was to prevent leaks from the terminal portion between the capsule and its hand-made fitting, especially when pressures over 4 *bar* were reached. Using PTFE seal tape and cyanoacrylate glue, we fixed the problem. Finally, for this sample, we managed to obtain pressures over 8 *bar* and an excellent replicability of the pressure test.

Figure 5.5 displays the assembly of the titanium capsule and the hand-made fitting, ready to start a pressure test. Before applying adhesives, we always cleaned the surfaces with solvent to eliminate any grease residue. If the material was metal, we first proceeded to make the surfaces rough, with the use of sandpaper, for a better bonding.



**Figure 5.5** Machined titanium alloy sample connected to the hand-made fitting.

For the sample molded in PA of figure 5.4, we first applied a two-component adhesive made of epoxy resins with poor results, then we tried a suitable cyanoacrylate adhesive for hard plastic. Also in this case, we first seal the holes with the help of duct tape and cyanoacrylate glue. With this sample, we managed to reach about 4 *bar*, then the pressure forces were such as to split the specimen in half. Figure 5.6 shows the result of the pressure test: the black colored material that is seen inside the open capsule is duct tape used to seal the holes, but which reacted badly to contact with the glue by wrapping around itself. While good sealing results were obtained, this sample was not used in tests with strain gauges due to a lack of time.



**Figure 5.6** PA molded sample, pressure test.

## Chapter 6

# Experimental tests with sensorized samples and analysis of the results

This chapter describes the core phase of the experimental laboratory activity performed in the Department of Mechanical and Aerospace Engineering of Politecnico di Torino. In the following paragraphs, tests with pressure adjustment on sensorized samples are presented. The samples were equipped with strain gauges to provide the volume variation of the reservoir [16]. The tests were performed on the additive manufactured capsules made of Ti6Al4V and PA12, and on the machined titanium alloy (Ti6Al4V) capsule sent from Dr. Grattoni's laboratory.

### 6.1 Installation of strain gauges on samples

After having sealed the samples, we started with the installation of the strain gauges. We decided to use the linear strain gauge we had used for the tests on the cantilever beam, described in Chapter 3. The strain gauge is a custom product made by Micro-Measurements. Its grid has a linear pattern and an active gage length of 3,56 mm. The specifications of the sensor are shown again in the following table:

Resistance at 24°C	$350 \Omega \pm 0.3\%$
Gage factor at 24°C	2.08 <i>nom</i>

**Table 6.1** Liner strain gauge specifics.

Strain gauge is bonded on one of the two symmetric circular surfaces of the disc-shaped device. For the machined titanium alloy capsule, the strain gauge was attached on the face that did not have the holes in the central area, i.e. the side shown in Figure 5.4 on the previous page. In fact, as explained above, the strain gauge should be positioned in the center of the circular membrane of the disc-shaped capsule, as this area presents the largest strain values due to the internal pressure of the reservoir. Since this was a metal sample, we proceeded to roughen the surface and clean it with solvent as a preparation for gluing. To help us in the positioning of the strain gauge, we drew with a pencil a few guidelines along the diameter direction and perpendicular to it. The reference marks of the strain gauge must be aligned with the guidelines. Thus, the active gauge length is placed along the diameter of the circular surface for measuring the strain in the center. We employed a magnifying glass to aid us with the positioning and gluing operations. The adhesive used for bonding was cyanoacrylate glue. Figure 6.1 illustrates the result of the installation of the sensor on this sample.



**Figure 6.1** Result of the installation of the linear strain gauge on the machined Ti6Al4V sample.

For strain gauge installation on the additive manufactured capsule made of Ti6Al4V, we followed the same procedures as for the previous sample, since both are metallic. For the latter, less difficulty was encountered in the construction of the guidelines and in the positioning of the strain gauge, given the larger surface of the capsule. For bonding, one of the two identical available faces of the sample was chosen. The adhesive used in the bonding process was cyanoacrylate glue. Figure 6.2 shows the outcome of the installation of the linear strain gauge on this sample.



**Figure 6.2** Result of the installation of the linear strain gauge on the AM Ti6Al4V sample.

For strain gauge installation on the additive manufactured capsule made of PA 12, some precautions relating to the material have been adopted. The use of sandpaper is not necessary because of the high surface roughness of polyamide 12. For the same reason we had to draw the alignment guidelines using a thin marker. The rest of the bonding procedure is the same as for the other samples. Again, the adhesive used for bonding was cyanoacrylate glue. Figure 6.3 shows the results of the installation of the linear strain gauge on the AM PA 12 capsule.



**Figure 6.3** Result of the installation of the linear strain gauge on the AM PA 12 sample.

## 6.2 Test procedure

In this phase of the activity, experimental tests were performed using the test bench previously fabricated and the data acquisition system described in Chapter 3. Experimental tests are realized with the three different samples outlined in the previous paragraph. During tests, on each capsule, a linear strain gauge was installed at the center of the circular surface. This strain gauge has preattached copper leads, to which we soldered a first set of thin and short cables that were soldered in turn to thicker and longer wires connected to a socket/plug. The sensor was connected to QuantumX MX1615B amplifier module through a 4-wire quarter bridge configuration (for more details on the wiring configuration see paragraph 3.2.3). The sample was connected to the water circuit via a push-in fitting. To avoid the presence of air bubbles inside the hydraulic line, we filled the sample with water before its connection.

All the experimental tests were performed following a standard testing procedure: we gradually increased the pressure step by step and kept the pressure value of interest fixed for a time of 30 seconds. Using the amplifier module and Catman®Easy software we acquired data of the strain behavior as function of time. During the post-process phase, we analyzed the acquired data and computed the average, maximum and minimum strain value in the time interval of 30 seconds corresponding to a specific value of pressure. During the tests, the value of pressure was read via a barometer connected to the line.

The result of the post-processing activity was the realization of the graph of the strain as a function of internal pressure. The following step was to perform interpolation in order to find the linear relationship between strain and pressure. In the following pages are described all the experimental tests performed on the samples with the obtained results:

- temporal behavior of the strain, during pressure adjustment, acquired with QuantumX amplifier module and Catman®Easy software (strain as function of time).
- table with statistical results obtained from the acquisition.
- graph of strain as a function of pressure with liner interpolation of the data.

The following figure displays the overall set up of test bench and data acquisition system during the testing activity.

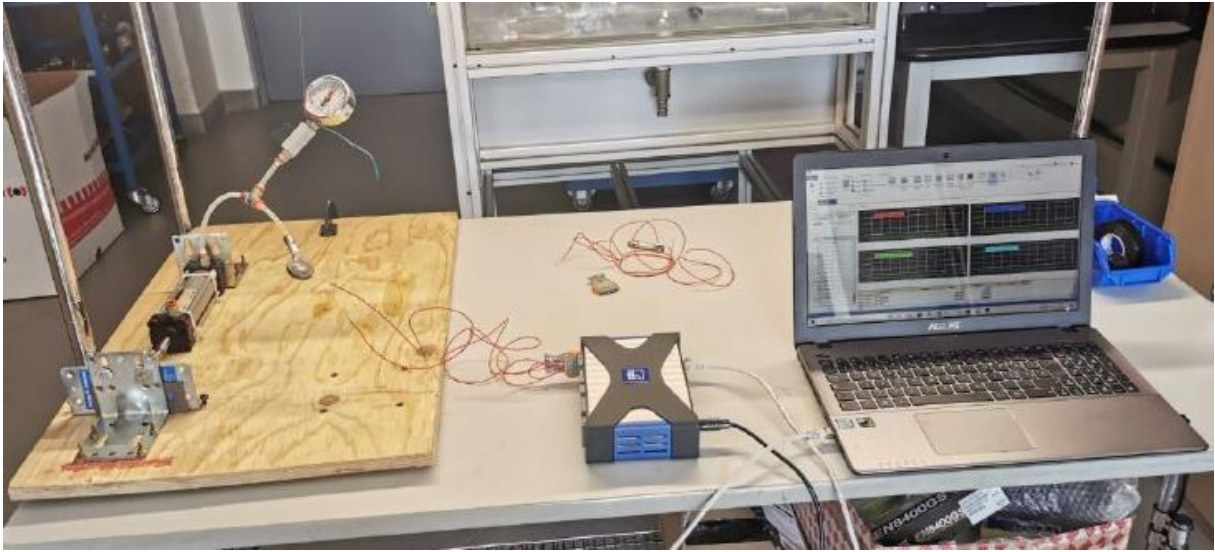


*Figure 6.4* Test bench set up for testing on sample.

### 6.2.1 Sample 1: titanium alloy threaded capsule

Two tests are performed for sample 1 in order to obtain more reliable results. Data acquisition is obtained using QuantumX amplifier module and Catman software. After connection, the strain gauge must be configured as “SG 4 wire 350 Ohm”. Once this procedure is completed, it is possible to carry out the zero balancing (“Zero Balance”) with the selected channel of the module and start the test. The result of the acquisition is a graph of the strain output as a function of time.



*Figure 6.5* Sample 1 connected to the hydraulic line.

TEST 1

Figure 6.6 displays the diagram of the strain output of the sensor as a function of time. By analyzing the diagram, it is possible to notice a step-by-step behavior since the pressure is kept fixed for 30 seconds in correspondence with the values of interest. The graph has been detailed by adding the relative pressure value scale to the right as shown in the figure below. The value of strain is indicated in  $\mu m/m$  and the value of the relative pressure is reported in *bar*.

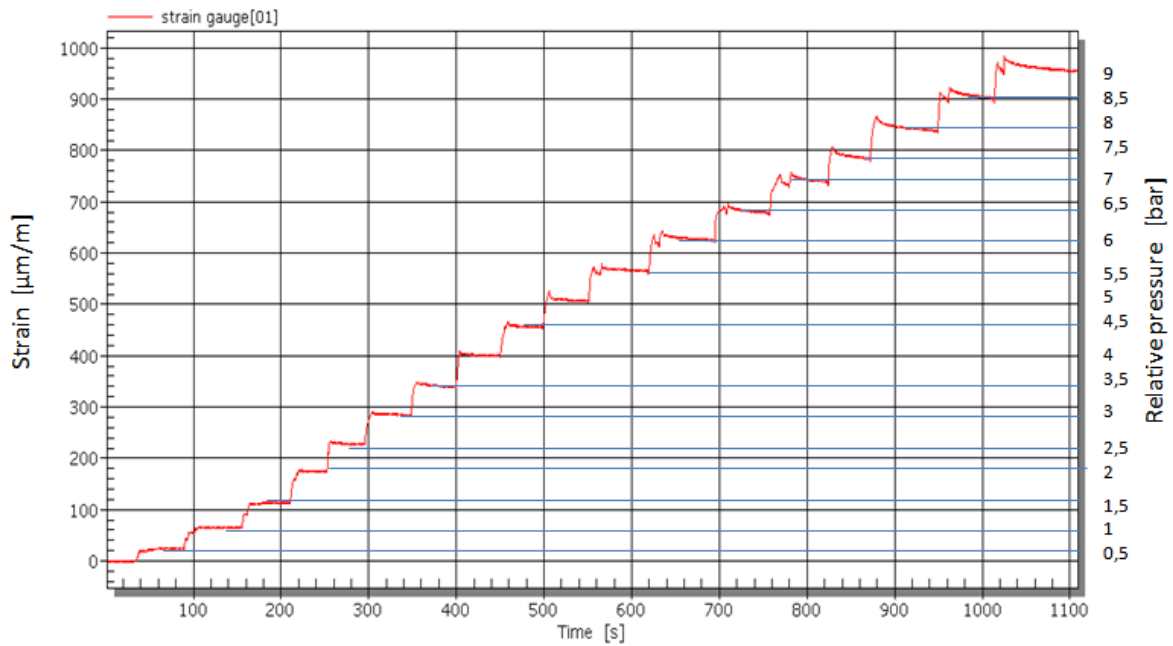


**Figure 6.6** Test 1 (sample 1): strain output as a function of time.

From the graph in Figure 6.6, the acquired data are elaborated, and the main statistical values are extracted for further analysis. In particular, for each 30-second interval corresponding to a specified pressure value, the following references shall be identified:

- Mean strain
- Maximum strain
- Minimum strain

All the statistical reference strain measurements, extracted from data acquisition, are listed in Table 6.1 below.

Relative pressure [bar]	Mean strain [ $\mu\text{m}/\text{m}$ ]	Max strain [ $\mu\text{m}/\text{m}$ ]	Min strain [ $\mu\text{m}/\text{m}$ ]
0	0	0	0
0,5	23,7	25,5	21,95
1	64,95	66,6	63,12
1,5	112,39	114,18	110,34
2	175,47	177,15	173,88
2,5	228,75	231,03	226,86
3	285,47	288,29	283,24
3,5	341,06	344,72	338,44
4	401	403,82	398,64
4,5	456,61	459,22	454,1
5	508,27	510,89	505,62
5,5	567,14	570,5	564,37
6	627,93	631,99	624,67
6,5	682,05	687,16	678
7	743,5	749,4	738,98
7,5	789,3	795,95	784,58
8	846,83	853,88	841,82
8,5	910,39	918,77	904,85
9	965,2	972,93	959,7

**Table 6.1** Test 1 (sample 1): strain data acquired.

Starting from the data in the table above, a graph of the strain as a function of pressure is obtained using Excel. Starting from the data in the table above, a graph of the strain as a function of pressure is obtained using Excel. The interpolation line is plotted on the graph below in order to obtain the pressure stress equation. Computing the relationship between measured strain and internal pressure is the final goal of the experimental activity. Experimental results will then be analyzed and compared with theoretical ones to validate the method of measure and the sensor system.

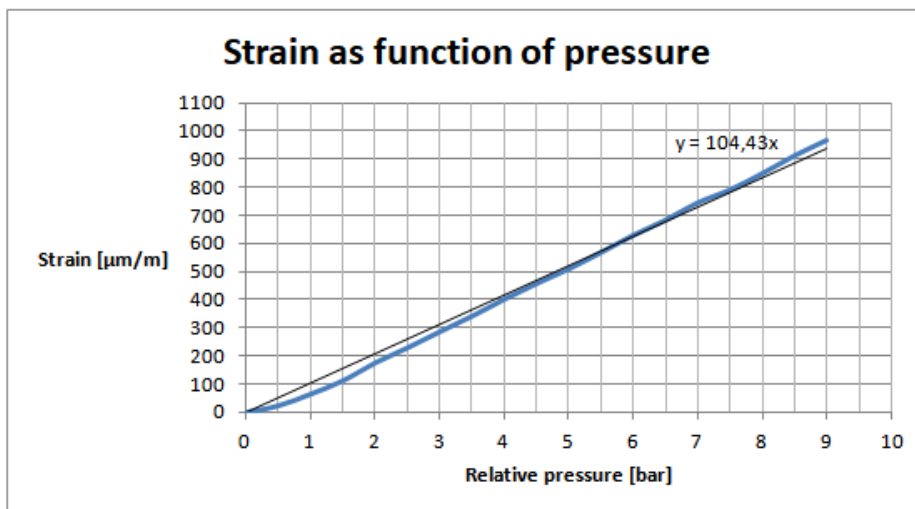


**Figure 6.6** Test 1 (sample 1): strain output as a function of pressure.

TEST 2

The same procedure described in Test 1 is followed when performing Test 2. It must be said that after the first test, no leakage was detected in the hydraulic line and in the sample. Therefore, it was possible to conduct the second test without the need for additional sealing. The following pages present the results obtained for Test 2 on sample 1. Figure 6.7 displays the diagram of the strain output of the sensor as a function of time.

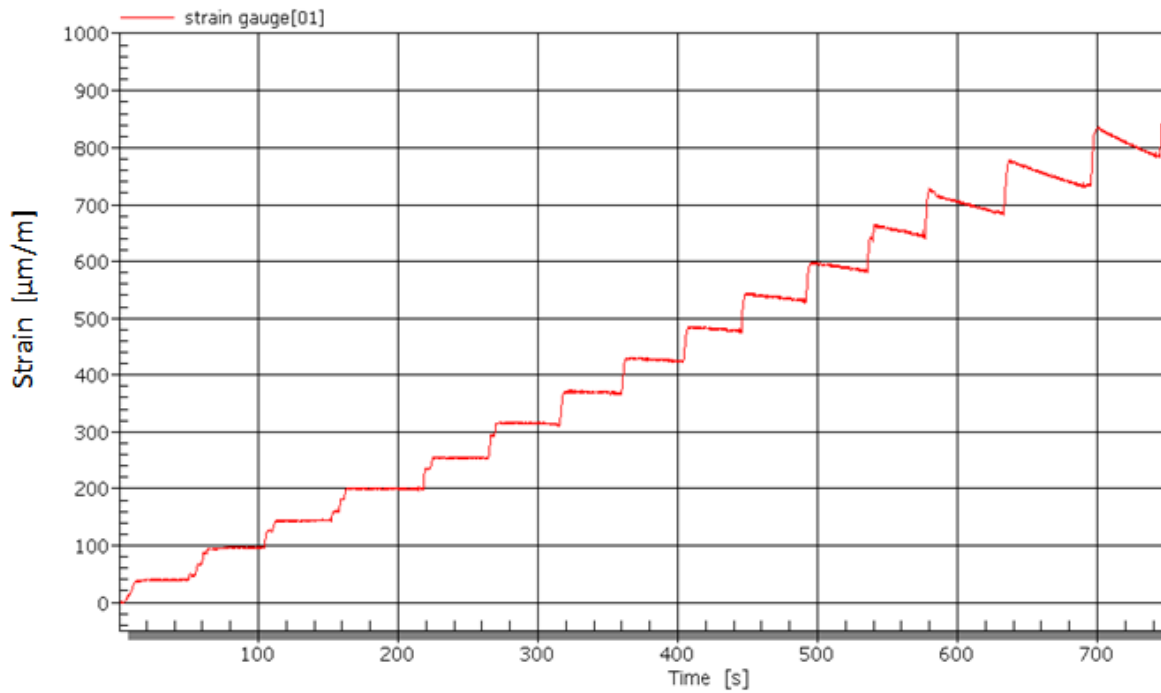


Figure 6.6 Test 2 (sample 1): strain output as a function of time.

Relative pressure [bar]	Mean strain [µm/m]	Max strain [µm/m]	Min strain [µm/m]
0	0	0	0
0,5	39,09	41,32	35,83
1	95,28	97,38	92,25
1,5	143,8	145,3	141,9
2	200,2	201,7	198,5
2,5	253,5	255,1	252,1
3	314,9	316,3	313,1
3,5	370	372,4	367,3
4	427	430,3	423,6
4,5	481,1	485	476,8
5	538	543,4	532,6
5,5	590,9	597,4	583,5
6	654,5	663,6	645,3
6,5	703,4	714,9	692
7	756	770,9	741,5

Table 6.2 Test 2 (sample 1): strain data acquired.

All the statistical reference strain measurements, extracted from data acquisition, are listed in Table 6.2 above.

In this second test, it was not possible to reach a pressure of 9 *bar*, as in the previous test, because of the occurrence of a leakage between the hand-made fitting and the sample 1. The strain-pressure experimental characteristics is realized also for Test 2 and is shown in figure below.

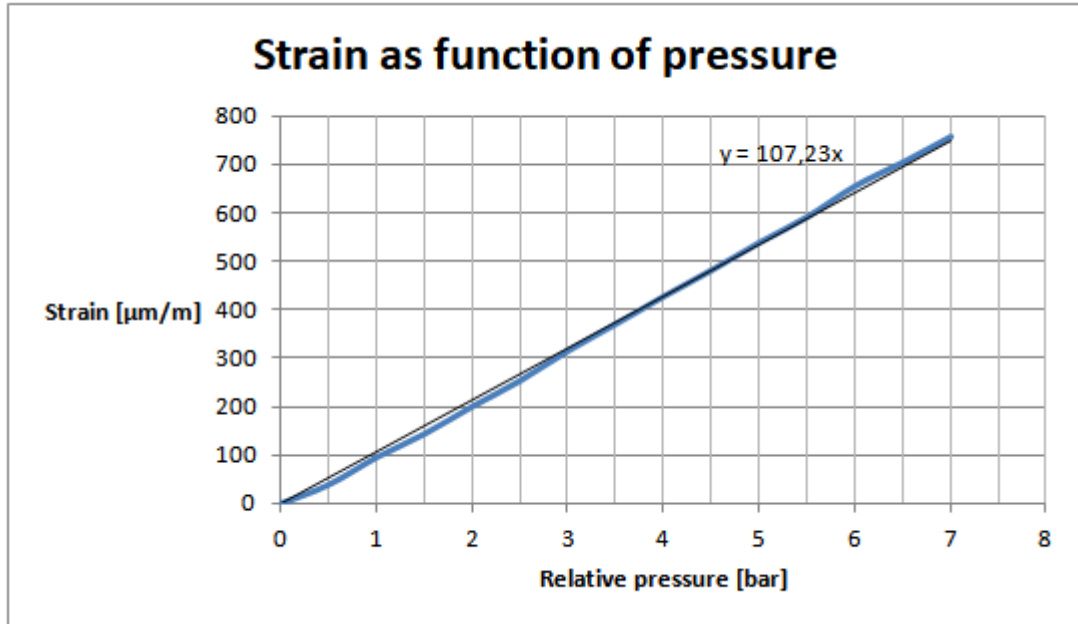


**Figure 6.6** Test 2 (sample 1): strain output as a function of pressure.

### 6.2.2 Sample 2: additive manufactured titanium alloy capsule

As in the previous case of sample 2, two tests are performed in order to obtain more reliable results and to verify repeatability. Figure 6.7 below displays the AM titanium alloy capsule with the linear strain gauge installed at the center of a side.

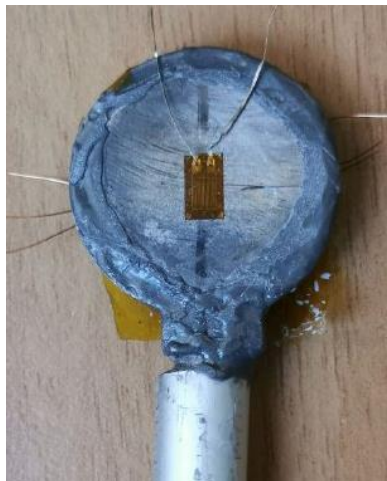


**Figure 6.7** Sample 2: AM titanium alloy capsule.

TEST 1

The same test procedure described for performing experimental tests on sample 1 is followed to realize the tests of sample 2. The results obtained are shown in the following pages.

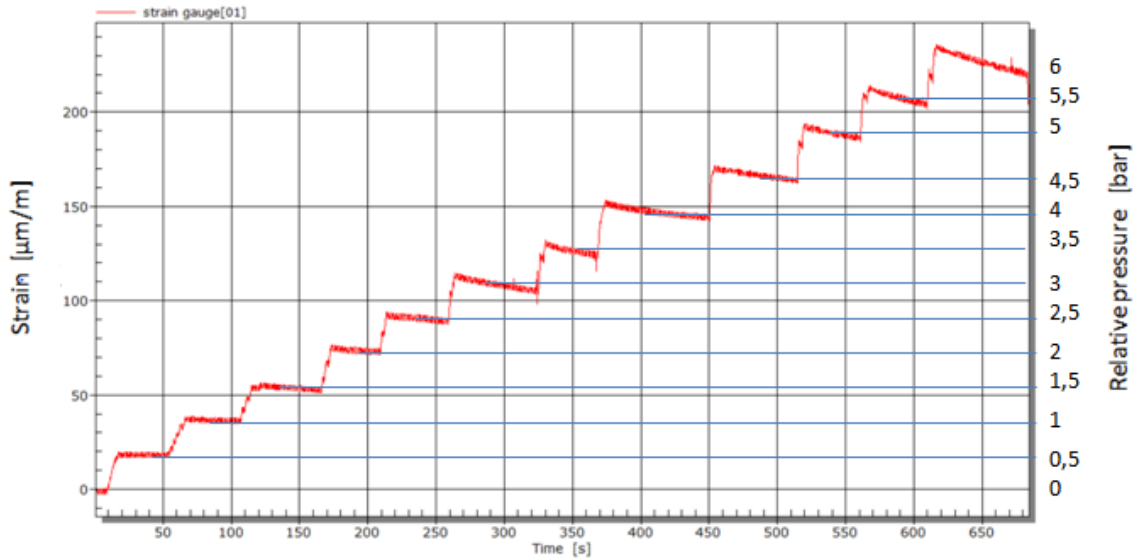
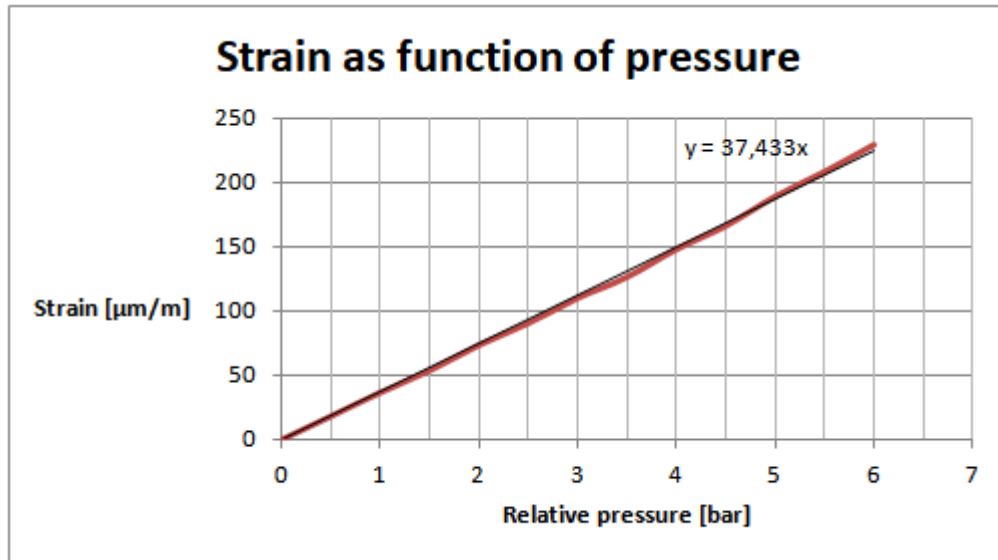


Figure 6.8 Test 1 (sample 2): strain output as a function of time.

Relative pressure [bar]	Mean strain [µm/m]	Max strain [µm/m]	Min strain [µm/m]
0	0	0	0
0,5	18,25	19,66	16,87
1	36,75	38,57	35
1,5	53,76	56,32	51,49
2	73,67	76,26	71,3
2,5	90,61	93,23	87,71
3	110,2	114	106,8
3,5	126,6	130,7	122,8
4	148,1	151,5	144,6
4,5	166,3	169,1	163,4
5	189,2	193,1	185,8
5,5	208,4	213	203,7
6	229,3	234,8	224,6

Table 6.3 Test 1 (sample 2): strain data acquired.

On sample 2 we reached a maximum pressure value of 6 *bar* to not risk permanent damage of the capsule sealing due to leakage. As in the previous case we compute the equation between strain and pressure.



*Figure 6.9* Test 1 (sample 2): strain output as a function of pressure.

## TEST 2

The same procedure described in Test 1 is followed when performing Test 2. The following pages present the results obtained for Test 2 on sample 2.

Relative pressure [bar]	Mean strain [µm/m]	Max strain [µm/m]	Min strain [µm/m]
0	0	0	0
0,5	21,39	22,69	20,3
1	40,77	41,95	39,67
1,5	58,78	59,85	57,57
2	77,17	78,18	76,04
2,5	95,67	96,88	94,37
3	115,5	117,3	114,1
3,5	134,7	136,6	132,6
4	155	156,9	153,5
4,5	174,8	177	172,8
5	192,5	195,2	189,9
5,5	209,9	212,8	207,5
6	227	233,8	203,4

*Table 6.4* Test 2 (sample 2): strain data acquired.

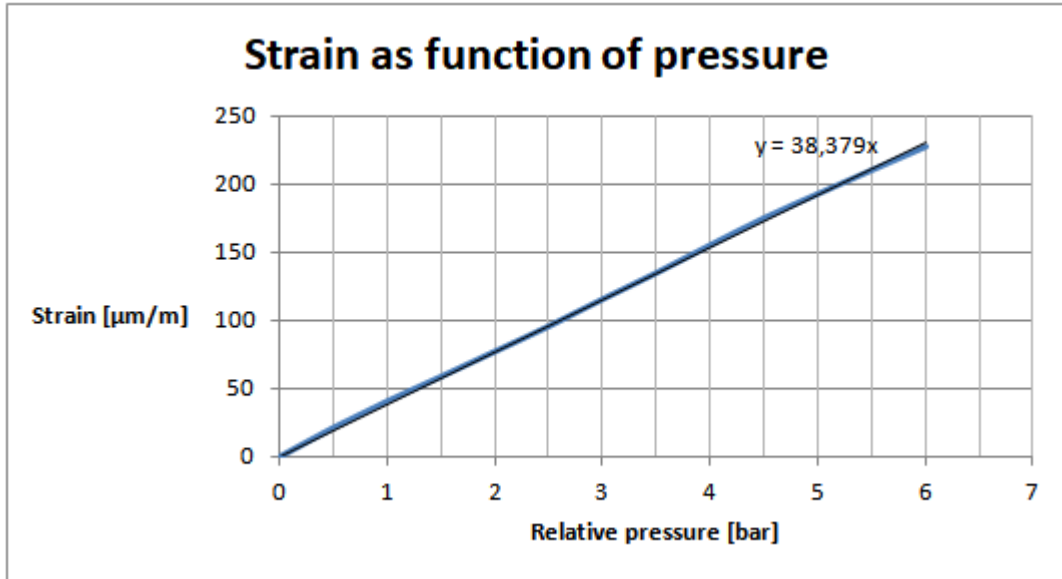


*Figure 6.10* Test 2 (sample 2): strain output as a function of pressure.

### 6.2.3 Sample 3: additive manufactured polyamide 12 capsule

The third and last testing slot was performed on AM PA 12 disc-shaped sample. Again, two tests are performed in order to obtain more reliable results and to verify repeatability. Figure 6.11 below shows sample 3 equipped with the linear strain gauge, during the experimental test. It can be noted that sample 3 swelled visibly due to the high internal pressure imposed.

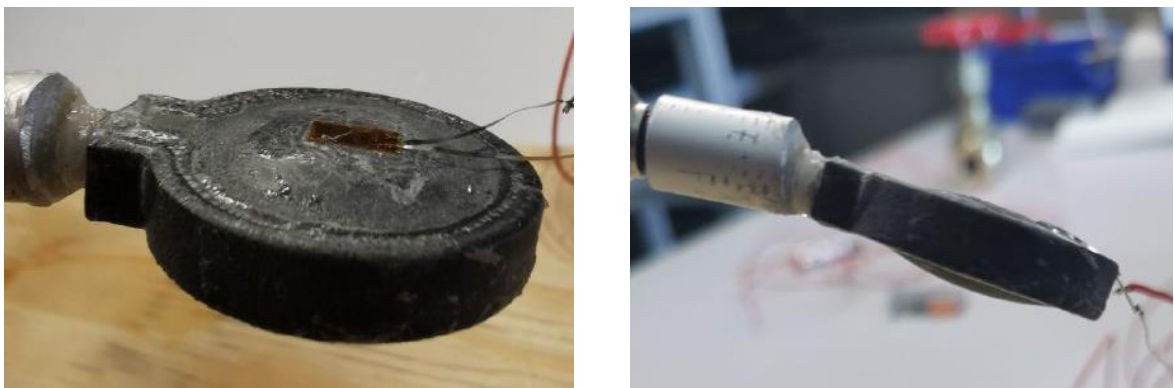


*Figure 6.11* Sample 3: AM PA 12 capsule.

TEST 1

In the following pages are described the results obtained for the two experimental tests performed on sample 3. In both tests we reached a maximum pressure value of 3,3 *bar*. It was possible to notice a great deformation of the sensorized surface corresponding to this pressure value. Moreover, we noticed that for higher pressure values the strain gauge detached due to the large deformation of the bonding region.

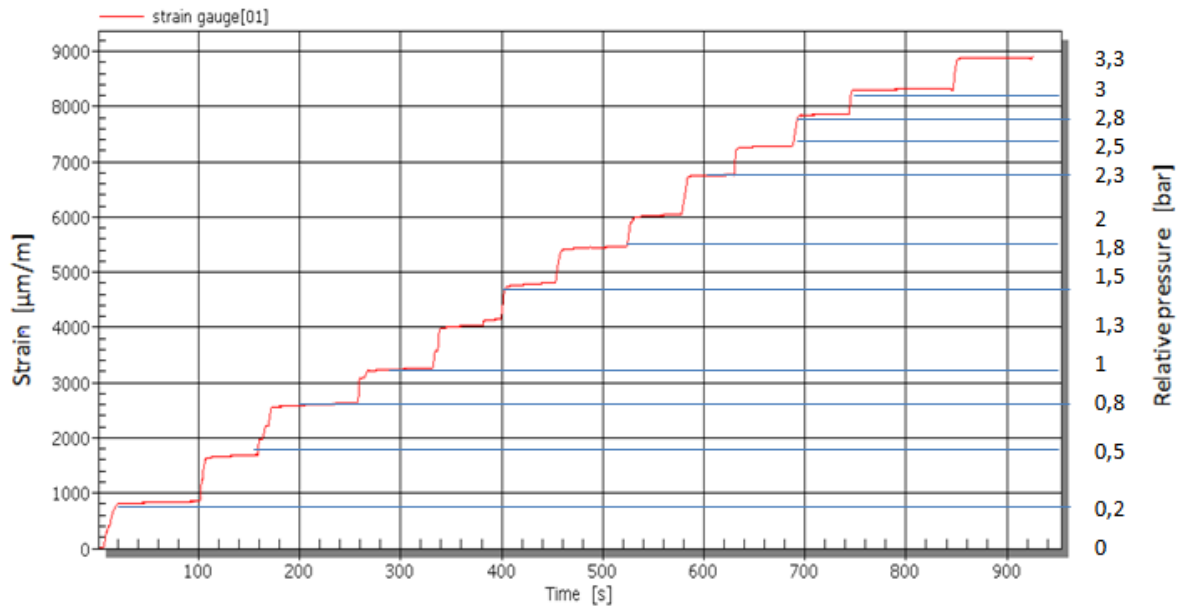
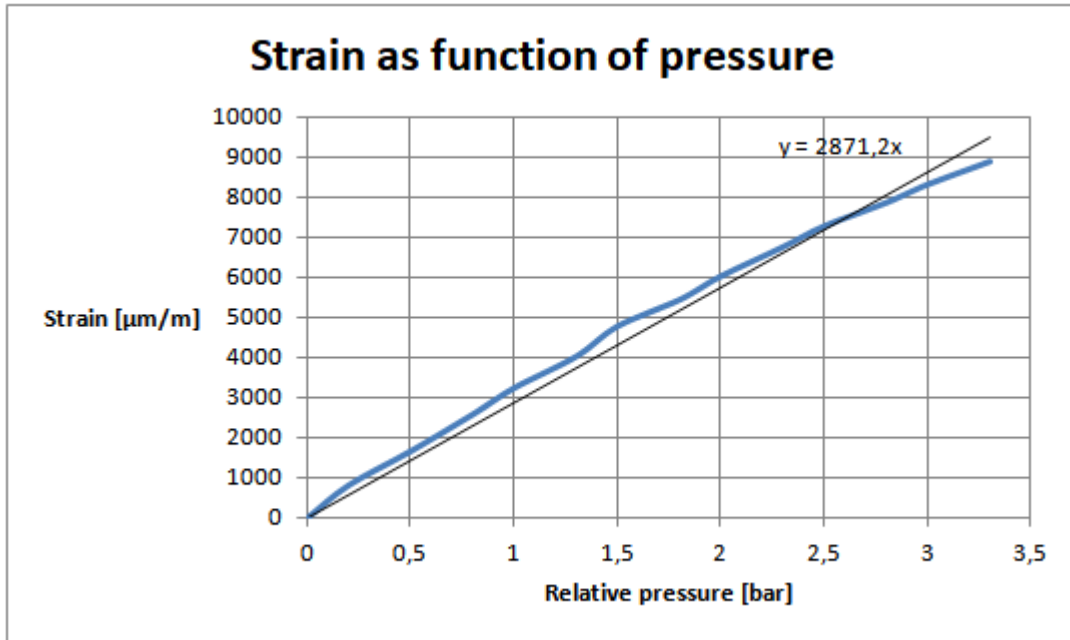


Figure 6.12 Test 1 (sample 3): strain output as a function of time.

Relative pressure [bar]	Mean strain [µm/m]	Max strain [µm/m]	Min strain [µm/m]
0	0	0	0
0,2	818,9	828,9	807,7
0,5	1664	1681	1634
0,8	2581	2598	2564
1	3238	3251	3223
1,3	4024	4044	3999
1,5	4773	4796	4743
1,8	5436	5452	5410
2	6020	6036	5988
2,3	6750	6760	6740
2,5	7267	7282	7237
2,8	7853	7860	7844
3	8305	8309	8301
3,3	8873	8875	8871

Table 6.5 Test 1 (sample 3): strain data acquired.



**Figure 6.13** Test 1 (sample 3): strain output as a function of pressure.

## TEST 2

For the second test we report the table of statistical value and the final graph of the strain behavior as a function of the internal pressure.

Relative pressure [bar]	Mean strain [µm/m]	Max strain [µm/m]	Min strain [µm/m]
0	0	0	0
0,2	737,4	747,5	720,1
0,5	1675	1690	1650
0,8	2546	2563	2503
1	3174	3189	3148
1,3	3713	3723	3706
1,5	4348	4394	4286
1,8	5164	5182	5150
2	5538	5575	5462
2,3	5936	5944	5930
2,5	6373	6383	6363
2,8	6875	6884	6863
3	7228	7247	7208
3,3	7522	7564	7493

**Table 6.6** Test 2 (sample 3): strain data acquired.

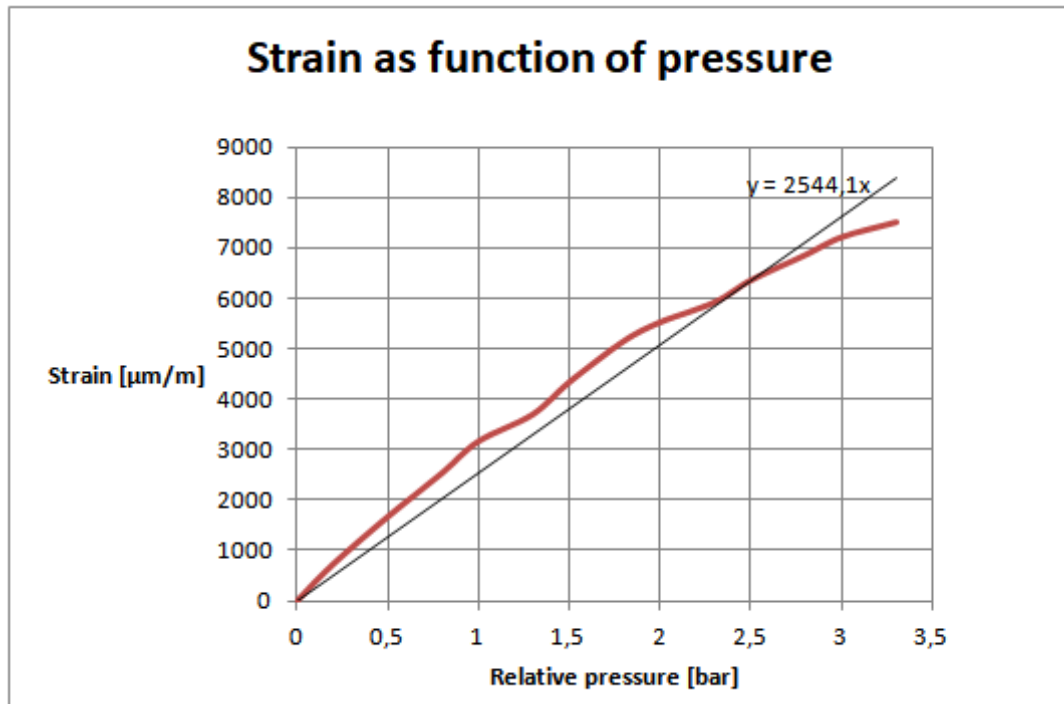


*Figure 6.14* Test 2 (sample 3): strain output as a function of pressure.

### 6.3 Analysis of testing results

The purpose of the analysis activity is to compare the experimental results with theoretical ones to validate the method of measure developed. Theoretical computation of strain values as function of pressure has been performed for the three different samples.

#### 6.3.1 Theoretical equation which relates strain and pressure

In this paragraph we derive the theoretical relationship between the strain and the internal pressure of the disc-shaped sample. Hence, we needed to identify the case in literature that best suited our device behavior during the tests, in order to obtain the formula of pressure as a function of strain. The choice was made based on the following considerations:

- the strain gauge is applied in the most loaded point, already identified by means of the FEM structural analysis performed. This point corresponds to the center of the circular surface of the device.
- the surface of the device on which the sensor is applied can be considered as a circular plate, loaded with uniform pressure and fixed boundaries.

The following figure presents the strain distribution in a circular plate with fixed boundaries and uniform pressure applied. It can be shown that at the centre of the plate tangential and radial strain are equal.

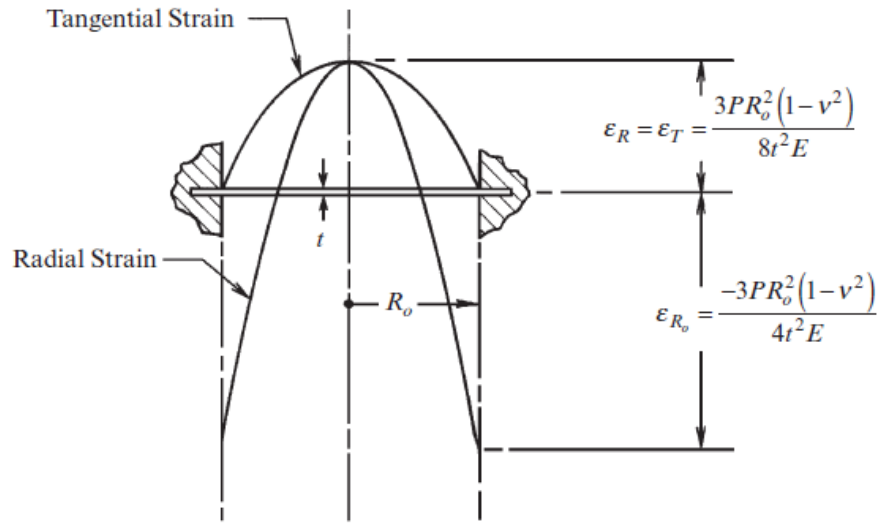


**Figure 6.15** Strain distribution in a circular plate with fixed boundaries [17].

It is possible to compute the theoretical value of strain at the centre using the following formula:

$$\varepsilon_R = \varepsilon_T = \frac{3PR_o^2(1-\nu^2)}{8t^2E} \quad (6.1)$$

Equation 6.1 contains the following terms:

$\varepsilon_R$  is the radial strain

$\varepsilon_T$  is the tangential strain

$P$  is the pressure applied [ $Pa$ ]

$R_o$  is the radius of the circular plate [ $mm$ ]

$t$  is the plate thickness [ $mm$ ]

$\nu$  is Poisson's ratio

$E$  is the Young's modulus [ $Pa$ ]

Equation 6.1 shows the relationship between strain and pressure. It is possible to reformulate this equation in order to have the pressure as a function of the strain. We can obtain in this way the desired transfer function:

$$P = \frac{8t^2E\varepsilon}{3R_o^2(1-\nu^2)} \quad (6.2)$$

### 6.3.2 Theoretical calculation of strain for sample 1

In the following table, the strain results were calculated using Equation 6.1, applied for the different relative pressure values, considering the particular properties of the capsule. In Table 6.7 are listed the values of the properties of sample 1 used in the calculation.

<b>Capsule properties (Ti6Al4V)</b>	
Young's modulus $E$ [ $Pa$ ]	1,07E+11
Poisson's coefficient $\nu$	0,36
Thickness $t$ [ $m$ ]	4,00E-04
Radius $R_o$ [ $m$ ]	7,90E-03

**Table 6.7** Sample 1 properties.

Relative pressure [bar]	Strain at the center [m/m]	Strain at the center [ $\mu\text{m}/\text{m}$ ]
0	0	0
0,5	5,95E-05	5,95E+01
1	1,19E-04	1,19E+02
1,5	1,78E-04	1,78E+02
2	2,38E-04	2,38E+02
2,5	2,97E-04	2,97E+02
3	3,57E-04	3,57E+02
3,5	4,16E-04	4,16E+02
4	4,76E-04	4,76E+02
4,5	5,35E-04	5,35E+02
5	5,95E-04	5,95E+02
5,5	6,54E-04	6,54E+02
6	7,14E-04	7,14E+02
6,5	7,73E-04	7,73E+02
7	8,33E-04	8,33E+02
7,5	8,92E-04	8,92E+02
8	9,52E-04	9,52E+02
8,5	1,01E-03	1,01E+03
9	1,07E-03	1,07E+03

**Table 6.8** Sample 1: strain data computed with Equation 6.1.

In the graph below, the strain behavior as function of the relative internal pressure is plotted, based on the values of Table 6.8.

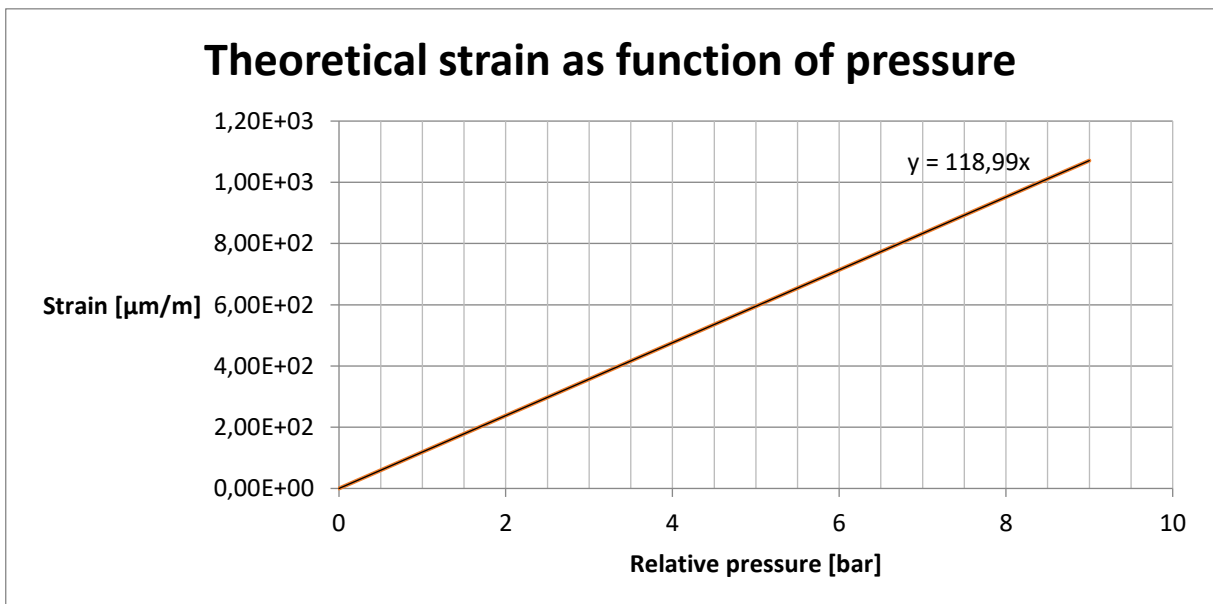


**Figure 6.16** Sample 1: theoretical strain as function of the relative pressure.

### 6.3.3 Theoretical calculation of strain for sample 2

The theoretical calculation procedure to determine the strain values as a function of the relative pressure inside the reservoir, is now applied for sample 2. The results obtained are presented below.

<b>Capsule properties (AM Ti6Al4V)</b>	
Young's modulus $E$ [ $Pa$ ]	1,07E+11
Poisson's coefficient $\nu$	0,323
Thickness $t$ [ $m$ ]	1,00E-03
Radius $R_o$ [ $m$ ]	1,25E-02

*Table 6.9* Sample 2 properties.

<b>Relative pressure [<math>bar</math>]</b>	<b>Strain at the center [<math>m/m</math>]</b>	<b>Strain at the center [<math>\mu m/m</math>]</b>
0	0	0
1	4,90E-05	4,90E+01
1,5	7,36E-05	7,36E+01
2	9,81E-05	9,81E+01
2,5	1,23E-04	1,23E+02
3	1,47E-04	1,47E+02
3,5	1,72E-04	1,72E+02
4	1,96E-04	1,96E+02
4,5	2,21E-04	2,21E+02
5	2,45E-04	2,45E+02
5,5	2,70E-04	2,70E+02
6	2,94E-04	2,94E+02
6,5	3,19E-04	3,19E+02
7	3,43E-04	3,43E+02

*Table 6.10* Sample 2: strain data computed with Equation 6.1.

In the next page, the strain behavior as function of the relative internal pressure is plotted in Figure 6.17, based on the values of Table 6.10.

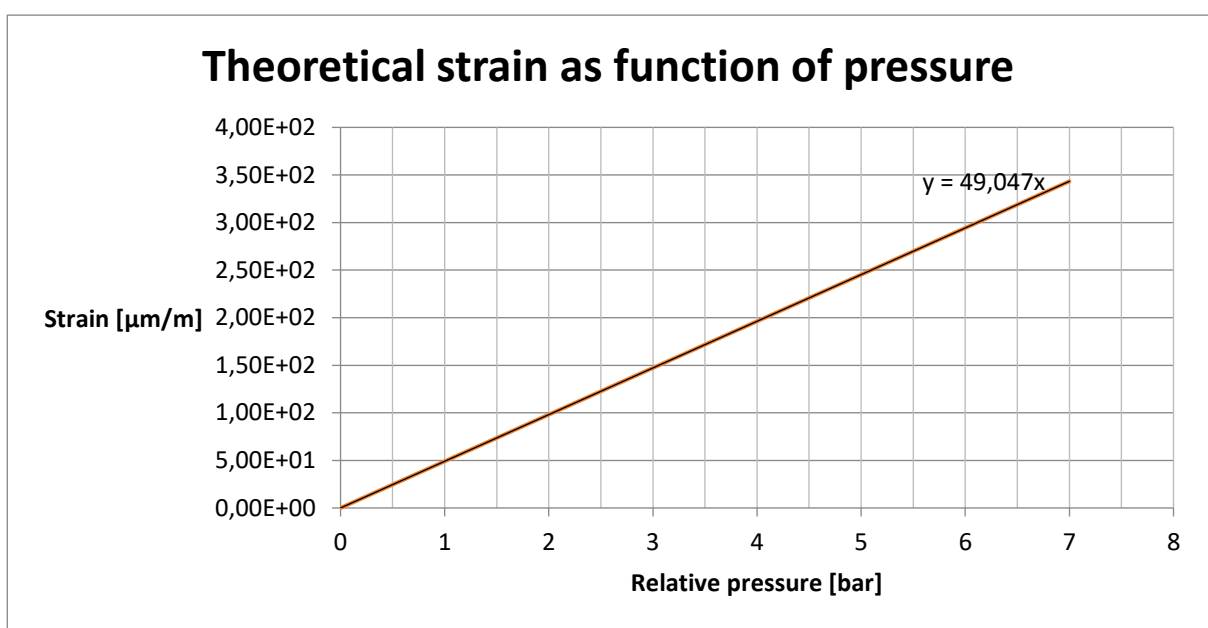


**Figure 6.17** Sample 2: theoretical strain as function of the relative pressure.

#### 6.3.4 Theoretical calculation of strain for sample 3

The theoretical calculation procedure used for the other two capsules is now applied for sample 3. The results obtained are presented below.

Capsule properties (AM PA 12)	
Young's modulus $E$ [ $Pa$ ]	1,80E+9
Poisson's coefficient $\nu$	0,349
Thickness $t$ [ $m$ ]	1,00E-03
Radius $R_0$ [ $m$ ]	1,25E-02

**Table 6.11** Sample 3 properties.

Relative pressure [bar]	Strain at the center [m/m]	Strain at the center [ $\mu\text{m}/\text{m}$ ]
0	0	0
0,2	5,72E-04	5,72E+02
0,5	1,43E-03	1,43E+03
0,8	2,29E-03	2,29E+03
1	2,86E-03	2,86E+03
1,3	3,72E-03	3,72E+03
1,5	4,29E-03	4,29E+03
1,8	5,15E-03	5,15E+03
2	5,72E-03	5,72E+03
2,3	6,58E-03	6,58E+03
2,5	7,15E-03	7,15E+03
2,8	8,00E-03	8,00E+03
3	8,58E-03	8,58E+03
3,3	9,43E-03	9,43E+03

**Table 6.12** Sample 3: strain data computed with Equation 6.1.

In Figure 6.18, the strain behavior as function of the relative internal pressure is plotted, based on the values of Table 6.12.

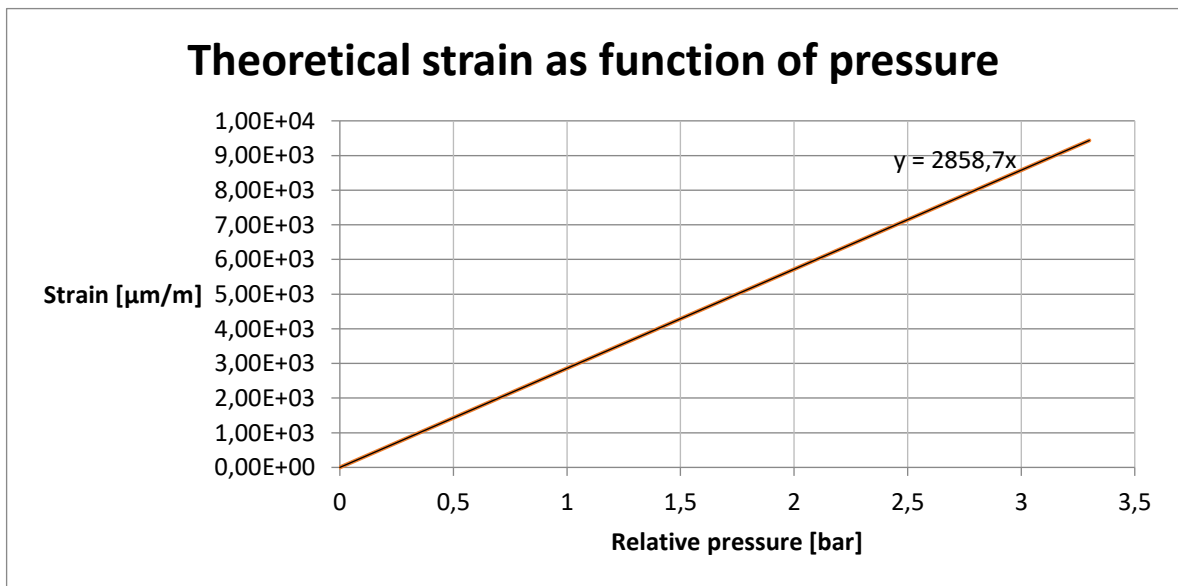


**Figure 6.18** Sample 3: theoretical strain as function of the relative pressure.

### 6.3.5 Comparison between theoretical and experimental results

This paragraph is dedicated to the comparison between experimental and theoretical results obtained for the three samples. Table 6.13 shows the strain-pressure experimental and theoretical linear characteristics of the samples. The experimental equations written in Table 6.13 are computed through the average of the gain values of the two tests performed.

Type of sample	Experimental equation	Theoretical equation
Sample 1	$y = 105,83 x$	$y = 118,99 x$
Sample 2	$y = 37,91 x$	$y = 49,047 x$
Sample 3	$y = 2707,65 x$	$y = 2858,7 x$

**Table 6.13** Comparison between theoretical and experimental results.

The experimental strain-pressure characteristics reported provide the gain factors  $G_{sample1} = 105,83$ ,  $G_{sample2} = 37,91$  and  $G_{sample3} = 2707,65$ .

## Chapter 7

# Conclusion

The experimental tests conducted on the machined titanium capsule sent from the Houston Methodist Research Institute, and on the titanium and PA 12 capsules fabricated by additive manufacturing processes, led to obtaining excellent results. The final outcomes from capsule prototypes equipped with strain gauges provided evidence of applicability to implantable drug delivery systems. From the comparison analysis between experimental and theoretical strain-pressure characteristics of paragraph 6.3.5, it is possible to notice very similar gain factors that confirm the goodness of the results obtained during the experimental activity. Differences can be attributed to many possible factors such as the fact that the capsule surface is considered, for the theoretical analysis, as a rigidly clamped diaphragm but this is just an approximation because the sensorized region has a more complex structure. Furthermore, the formula used to compute the strain is based on restrictive assumptions that are hardly respectable in reality, such as the perfectly elastic behavior of the material and an infinitely rigid clamping around the diaphragm periphery. Despite this, the experimental results are confirmed by the theoretical analysis of the tests. Following filtering and decoupling of external disturbances, the resolution of the sensing system is comparable with the target resolution of osmotic pressure measurement. There are particular advantages in the materials used. Titanium alloy capsules have higher dimensional accuracy and mechanical strength, while PA 12 capsule has low cost, fast manufacturing and higher sensing sensitivity provided by the flexibility of nylon polymer [16]. Our results show that the use of capsules made of metals and polymers processed by additive manufacturing can be a promising choice for the development of implantable drug delivery devices. The decision to use a linear strain gauge turned out to be a good choice. However, the employment of a diaphragm strain gauge could have provided a higher measurement accuracy. This type of strain gauges is specially developed for manufacturing precision pressure sensors. A diaphragm strain gauge, made available by our laboratory, was used to perform tests on the AM titanium capsule. Figure 7.1 shows the result of the installation of the sensor.



**Figure 6.18** Diaphragm strain gauge bonded on AM titanium capsule.

Unfortunately, satisfying measurement data could not be obtained because of communication issues between the acquisition software and the sensor. However, the linear strain gauge used has good accuracy and some advantages over the diaphragm sensor: it is much cheaper and requires an easier wiring connection.

## Conclusion

---

The best sealing for in vitro tests was obtained with the machined titanium capsule. The threaded coupling that connects the two parts of the sample proved to be an excellent solution to prevent leaks at high operating pressures. The design we conceived for the fabrication of the AM samples can certainly be improved to ensure a better sealing. One of the possible improvements could be the relocation of the cubic nub that connects to the fitting, so that it protrudes from only one of the two membranes which form the reservoir. In this manner, the tapping operation of the hole and the screwing of the fitting should not stress the coupling area of the glued parts. A further improvement may result from the use of alternative adhesives in the marketplace.

Regarding the necessity to discriminate the osmotic pressure induced by the nanofluidic membrane and that produced by external stresses, lot of work has still to be done in the forthcoming years. The solution of equipping the device with a protective external shell seems to be promising, however, much remains to be studied in order to produce a functioning prototype. The shell separates the device from the external environment, therefore a solution must be studied to enable the interaction of the nanofluidic membrane with the interior of the human body.

The following steps in the development of the device will include the design of a wireless system capable of powering the strain sensor and transmitting data, and the equipment of the nanofluidic membrane. The experimental results reported in this thesis will be the starting point for the realization of a working prototype to be tested in vivo.

# Bybliography

- [1] Stewart, S. A., Domínguez-Robles, J., Donnelly, R. F., & Larrañeta, E. (2018). Implantable Polymeric Drug Delivery Devices: Classification, Manufacture, Materials, and Clinical Applications. *Polymers*, 10 (12), 1379.
- [2] Sciammarella, Cesar A., and Sciammarella, Federico M. *Experimental Mechanics of Solids*. Hoboken: John Wiley & Sons, Incorporated, 2012. Web.
- [3] "Strain gauge". n.d. In *Wikipedia*. Retrieved June 24, 2021, from [https://en.wikipedia.org/wiki/Strain\\_gauge](https://en.wikipedia.org/wiki/Strain_gauge).
- [4] Karuppasamy, Karthik Selva Kumar, and Balaji P.S. "Introduction and Application of Strain Gauges." *Applications and Techniques for Experimental Stress Analysis*. IGI Global, 2019. 57-77. Web.
- [5] Keil, Stefan. *Technology and Practical Use of Strain Gages*. 1st ed. Newark: Ernst & Sohn, 2017. Web.
- [6] HBM website: <https://www.hbm.com/en/3053/quantumx-mx1615b-bridge-amplifier-for-strain-gauges/>
- [7] John Whitefoot, *Use of Strain Gages to Determine the Strain in Cantilever Beams*, Mechanical Measurements I course, October 11, 2018.
- [8] Instrumentation Devices website: [https://www.instrumentation.it/gallery/6847/Come\\_lavorano\\_gli\\_Estensimetri.pdf](https://www.instrumentation.it/gallery/6847/Come_lavorano_gli_Estensimetri.pdf).
- [9] Silva, Anderson Langone, Marcus Varanis, Arthur Guilherme Mereles, Clivaldo Oliveira, and José Manoel Balthazar. "A Study of Strain and Deformation Measurement Using the Arduino Microcontroller and Strain Gauges Devices." *Revista Brasileira De Ensino De Física* 41.3 (2018): Revista Brasileira De Ensino De Física, 2018-12-10, Vol.41 (3). Web.
- [10] Tokyo Measuring Instruments Lab website: [https://tml.jp/e/knowledge/strain\\_gauge/what\\_1g4w.html](https://tml.jp/e/knowledge/strain_gauge/what_1g4w.html).
- [11] HBM website: <https://www.hbm.com/en/6725/article-temperature-compensation-of-strain-gauges/>.
- [12] QuantumX Operating Manual: <https://www.hbm.com/fileadmin/mediapool/hbmdoc/technical/A03031.pdf>.
- [13] Catman Operating Manual: <https://www.hbm.com/fileadmin/mediapool/hbmdoc/technical/A05566.pdf>.

- [14] David Hazel, *Comparing strain gage measurements to force calculations in a simple cantilever beam*, Worcester Polytechnic Institute Major Qualifying project, January 27, 2016.
- [15] HBM website: <https://www.hbm.com/en/6725/article-temperature-compensation-of-strain-gauges/>.
- [16] Graziano, M., Charig, D. W., Di Trani, N., Grattoni, A., & De Pasquale, G. (2021). Design and characterization of AM sensorized capsules for drug delivery devices. *Transactions on Additive Manufacturing Meets Medicine*, 3(1), 504. <https://doi.org/10.18416/AMMM.2021.2109504>.
- [17] Vishay Precision Group website: <http://www.vishaypg.com/docs/11060/tn5101tn.pdf>.



# Ringraziamenti

Voglio iniziare scusandomi con tutte le persone che non mi ricorderò di nominare ma che hanno contribuito a questo successo. Vi ringrazio per avermi aiutato anche senza saperlo.

In primis, un grande ringraziamento va al mio relatore Dr. Giorgio De Pasquale ed al mio correlatore Dr. Alessandro Grattoni, per avermi concesso l'occasione di partecipare a questa tesi. È stato per me un onore collaborare e contribuire ad un progetto così ispirante ed ambizioso.

Uno speciale grazie va alla mia collega di tesi Marta Graziano con la quale ho collaborato durante lo svolgimento dell'attività di tesi.

Ringrazio il Politecnico di Torino e tutti i miei professori per avermi insegnato molto in questi anni ed avermi formato come ingegnere meccanico.

Voglio ringraziare tutti i miei compagni universitari che ho conosciuto durante questi anni ma anche coloro che, semplicemente facendo domande a lezione, hanno dissipato i miei dubbi. Uno speciale ringraziamento va ai miei compagni di studio, con i quali ho potuto preparare molti miei esami e che mi hanno aiutato quando qualcosa non era chiaro.

Ringrazio i miei coinquilini di Torino ed in particolare Elisabetta De Rocco che mi è stata vicino quando avevo bisogno di sfogarmi e che mi ha sostenuto nei momenti più difficili.

Grazie ai miei amici Filippo, Ivan e Stefano per aver creduto in me e soprattutto per aver condiviso con me i momenti più felici della mia vita. Non sarei la persona che sono senza di voi.

Grazie di cuore a mio fratello Gershom, alla sua compagna Lalla ed al mio bellissimo nipotino Ollie. Siete per me motivo di grande orgoglio e spero di riabbracciarvi presto.

A mia madre, grazie infinite per avermi concesso di studiare ed avermi sempre sostenuto in tutte le mie scelte. Grazie per avermi confortato, consigliato ma soprattutto per aver creduto in me.

Grazie al mio patrigno Carlo ed ai suoi figli Paolo e Andrea che mi hanno supportato e consigliato lungo tutto il mio percorso.

Ringrazio col cuore mio padre che mi ha sempre spronato a dare il meglio e che, nonostante la lontananza, mi è sempre stato d'aiuto quando dovevo prendere delle decisioni importanti. Un sentito grazie anche a sua moglie Anat che, con le sue dolci parole, mi ha sempre confortato e rasserenato.

Grazie infinite a mio nonno Guglielmo, che mi ha cresciuto ed aiutato sempre. Grazie per avermi insegnato cosa significa la forza di volontà e l'etica del lavoro.

Grazie a mia nonna Lea che, anche senza sentirci spesso, riesce sempre a farmi sentire amato ogni volta che mi vede.

Vorrei infine ringraziare con tutto il mio cuore mia nonna Rita che purtroppo è mancata e non potrà assistere al raggiungimento di questo traguardo. Sono sicuro che saresti stata orgogliosa di me.